5-2001

Time Dependent Density Functional Theory of Dynamical Response in 3d and 4d Metals

James M. Sullivan
University of Tennessee - Knoxville

To the Graduate Council:

I am submitting herewith a dissertation written by James M. Sullivan entitled "Time Dependent Density Functional Theory of Dynamical Response in 3d and 4d Metals." I have examined the final electronic copy of this dissertation for form and content and recommend that it be accepted in partial fulfillment of the requirements for the degree of Doctor of Philosophy, with a major in Physics.

Adolfo G. Eguiluz, Major Professor

We have read this dissertation and recommend its acceptance:

Gerald D. Mahan, Robert N. Compton, Bennett C. Larson

Accepted for the Council:

Carolyn R. Hodges

Vice Provost and Dean of the Graduate School

(Original signatures are on file with official student records.)

To the Graduate Council:

I am submitting herewith a dissertation written by James M. Sullivan entitled "Time Dependent Density Functional Theory of Dynamical Response in 3*d* and 4*d* Metals." I have examined the final copy of this dissertation for form and content and recommend that it be accepted in partial fulfillment of the requirements for the degree of Doctor of Philosophy, with a major in Physics.

Adolfo G. Eguiluz

Adolfo G. Eguiluz, Major Professor

We have read this dissertation and

recommend its acceptance:

Gerald D. Mahan

Robert N. Compton

Bennett C. Larson

Accepted for the Council:

Dr. Anne Mayhew

Interim Vice Provost and Dean of

The Graduate School

Time Dependent Density Functional Theory of Dynamical Response in 3*d* and 4*d* Metals

A Thesis

Presented for the

Doctor of Philosophy

Degree

The University of Tennessee, Knoxville

James M. Sullivan

May 2001

Dedication

This Thesis is dedicated to my parents

Joann Jefferson Sullivan

and

Gary Lynn Sullivan

who have provided unwavering support in all of my

endeavors of life.

Acknowledgements

I thank the committee members, Adolfo G. Eguiluz, Bennett C. Larson, Gerald D. Mahan and Robert N. Compton for their help in the preparation of this Thesis. I especially thank my advisor, Adolfo G. Eguiluz for providing me with the opportunity to explore various aspects of the many-body problem and for the countless hours he has spent educating me. In this same regard, I also wish to thank Bennett C. Larson for his many difficult questions, seeking the answers to which helped shape my physical intuition. To my colleague and friend, Wei Ku, I am grateful; the numerous conversations we have had concerning both conceptual and technical issues has propelled my own research success at a rate far greater than I would have achieved otherwise. Wolf-Dieter Schöne and Igor Campillo, especially during the first two years of my graduate studies, also played a significant role in my education and for that, I thank the both of them. Martin Fuchs has graciously provided me with pseudopotentials, without which, the calculations of Chapter Two would be impossible.

I thank the members of the theory group of the Solid State Division of Oak Ridge National Laboratory, John Cook, Dick Wood, Randy Fishman, and Zhenyu Zhang for all the useful information they have bestowed upon me over the years and for accepting me into their daily activities in the context of scientific research at a national laboratory. I am also grateful to the excellent teachers I have had while at the University of Tennessee.

Special thanks goes to Ward Plummer for his help in locating postdoctoral opportunities and for serving as a mentor to me over the years.

I acknowledge financial support from the Department of Physics at the University of Tennessee, Knoxville in the form of Teaching Assistantships and Science Alliance stipends. As well, the research grant of Adolfo G. Eguiluz (NSF-DMR-9634502) has provided financial support in the form of a Research Assistantship thereby allowing me more freedom to pursue research projects . Computing support has been provided by NERSC. I also thank the Joint Institute of Computational Science at the University of Tennessee for the training it has provided in the way of parallel computing. Special thanks goes to Christian Halloy and Kwai Wong for consultation on various technical aspects of the present numerical methods. Sharron King of the Solid State Division at Oak Ridge National Laboratory has been no less helpful; on numerous occasions her expertise in the way of computer technology has saved me many hours of research work.

Abstract

Two different but complementary quantum mechanical many-body problems are investigated. These problems include both static and dynamic aspects of the electron-electron interaction in real materials. In Chapter One, we take up the cases of Ag and Ni with a microscopic evaluation of the dielectric function and loss function using the formalism of time dependent density functional theory and all-electron techniques. We address the striking line shapes that have been recently observed via inelastic scattering experiments. The present work reveals three relevant energy scales for excitations in the selected systems. These scales are argued to be generic to a large number of 3*d* and 4*d* metals, and include the threshold for excitation of *d* electrons, final state energies, and the plasmon energy. Our results for Ag corroborate the experimental interpretation of the anomalous dispersion of the nominal plasmon loss, and shed new light on the striking line shape as well as predicting an anomalous dispersion of the nominal plasmon lifetime. In agreement with experiment, the theoretical loss spectrum of Ni is found to be equally complex with two prominent loss features at ~22 *eV* and ~28 *eV*. The *ab initio* results demonstrate that both phase space and a strong modulation of $d \rightarrow p$ transitions lead to the predicted behavior. Moreover, in contrast to the canonical description that has been used to describe these features, we find them to be quite different from plasma oscillations. In Chapter Two, we address static properties of the electron-electron interaction as it pertains to ground state properties. In the exchange-only method one approximates the exchange-correlation energy functional of density functional theory by

its Hartree-Fock form, ensuring that the method adheres to several scaling laws and identities which are violated by the local density and generalized gradient approximations. Although there is no formal correspondence to eigenvalue gaps determined by photoemission or inverse photoemission, we find that exchange-only results partially remove the discrepancy between these energy gaps and those obtained based on the local density approximation. However, we also find marked discrepancies with other recent theoretical treatments. Suggestions for future research are made.

Preface

For several years before beginning the actual work on the projects presented in this Thesis, the author was captivated by the world of many-body physics. This fascination mainly sprang from initial exposure to the field during undergraduate study at North Carolina State University. The two Chapters of this Thesis investigate, in *ab initio* detail, two different, but complementary, aspects of the electron-electron interaction in real systems. These studies, as described briefly in the pages that follow, represent a subset of the many aspects of the quantum mechanical many-body problem the author has been involved with over the course of graduate studies at the University of Tennessee, Knoxville.

There is a two-fold motivation for each of the problems presented in this Thesis. The primary motivation is to investigate electronic properties for solid materials with methods that are as realistic as possible. This attention to *ab initio* detail also allows us to shed light on recent experimental results which is the second motivation for the problems presented here. For the present work, we adopt the definition of *ab initio* as put forth by John A. Pople, who shared the 1998 Nobel prize in Chemistry with Walter Kohn and classifie a technique as *ab initio,* if it relies solely on the fundamental constants.

Chapter One provides insight into the dynamical response of select 3*d* and 4*d* metals using the formalism of time dependent density functional theory. The present work on the loss spectra of two prototypical materials, Ag and Ni, demonstrates that the

observations of recent experiments are easily accommodated in such an approach. It is also demonstrated that all-electron techniques are a necessity in these materials, as calculations carried out in a pseudopotential-based approach give a poor description of the screening and damping properties that reveal themselves in the dielectric and loss functions.

Chapter Two investigates a different aspect of the realistic quantum mechanical many-body problem, with a first look at non-local treatments of the exchange-correlation energy functional of density functional theory. When approximated in exchange-only theory, the energy functional and electron charge density satisfy several known scaling laws and other exact identities which are not satisfied with popular treatments, such as the local density and generalized gradient approximations. This preliminary exploration of "beyond-the-LDA" physics will pave the way to more sophisticated treatments of ground state and excited state properties.

Table of Contents

List of Figures

Chapter One: Dynamical Response in 3*d* and 4*d* Metals

INTRODUCTION

Density-functional theory, implemented in the local density approximation, has made possible the *ab initio* evaluation of total energies and related observables for a wide variety of materials [1], its success being best illustrated by noting that the 1998 Nobel prize was shared by Walter Kohn and John Pople for their fundamental contributions to the field [2,3,4]. By contrast, there is no "LDA-like" approximation scheme —i.e., one that is of rather general applicability, insightful, parameter-free, and relatively easy to implement— for the study of electronic excitations. The reason for this situation is easy to visualize as the spectrum of excitations in solids is often dominated by electron-electron interactions, which, furthermore, are intertwined with features of the one-electron band structure —e.g., flat bands. Thus, the loss spectrum is system-specific (except in simple metals, and for zero wave vector, in which case the dominant loss, the plasmon, is macroscopic in nature) and it becomes difficult to describe the physics of the excitations in terms of simple models of "universal" significance. Indeed these models often lead to discussions of "anomalies" or complicated patch-ups to existing simple models.

This complexity of the electronic degrees freedom of real materials is being directly probed in a new generation of high-resolution experiments involving electron

energy-loss spectroscopy (EELS) [5-10] and inelastic x-ray scattering spectroscopy (IXS) [8]. Interestingly, these investigations have revealed unexpected anomalies in the physics of the excitations in even the simplest systems, such as the alkalis [5] and Al [8]. Of more immediate relevance to this Thesis are recent EELS measurements for the 4*d* series including Pd, Ag, Cd, In, Sn and Sb [10] which reveal striking line shapes and a complex interplay between the nominal plasma oscillation and localized single-particle-like excitations.

Figure 1 displays the energy scales for prototypical 3*d* and 4*d* metals accounting for both the *d* electrons and the average *sp* electron density. The solid lines denote the binding energy and bandwidth of the 4*d*'s whereas the open circles represent the nominal plasma energy for the *sp* electrons of these materials; the dashed line through the points is a guide to the eye. The symbols are the position of resonance features observed with EELS for the 4*d* series [10] and for select 3*d*'s (Cu and Ni) [12]. We run the gamut from the case of Sb, in which the 4*d* level is a closed shell residing at ~32 *eV* below the Fermi level and is quite localized, to the case of Pd, with its open shell itinerant $4d^8$ electrons, which reside at the Fermi surface. If we imagine the physics of these systems as describable by a two fluid model, involving separately *sp*-electrons and *d*-electrons, we can picture this particular series as a means for the systematic investigation of the mutual interactions between extended (*sp*-like) and localized electronic states. The cases of Ag,

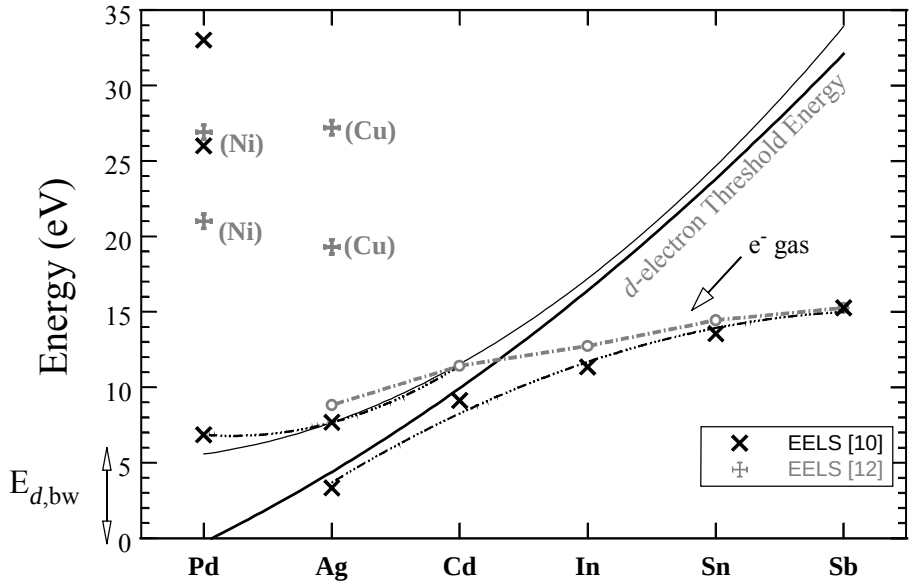

Figure 1 Energy scale relevant for excitations (both one- and two-particle) in select 4*d* elements. The vertical axis has units of energy while the horizontal axis scans select 3*d* and 4*d* elements. The gray lines denote the upper (thick line) and lower (thin line) edges of the d bands. Crosses correspond to resonance features observed in the EELS spectra [10]. Also shown is the nominal plasma energy (open symbols) obtained by considering the conduction electrons as a homogeneous electron gas; the thick black line is a guide to the eye.

Cd and In are particular intriguing, as the nominal energy for creation of plasma oscillations lies very close to the binding energy of the *d* levels; the proximity of these two energies gives rise to the conditions necessary for the existence of coupled excitations in the case of Ag [10,13]. In the case of Pd, there are resonance features at low energies (~7.8 *eV*) as well as two prominent features at much larger energies (~26 *eV* and ~33 *eV*). The loss spectrum of Ni shows similar features for the high-energy spectrum, with two loss features at ~22 and ~28 *eV*. Predominantly these two loss features have been discussed as plasma oscillations involving two separate types of electrons. For the case of Ag the excitation observed at ~7.8 *eV* in Ag is attributed to a plasma oscillation, though strongly renormalized by additional screening mechanisms and decay channels provided by the localized *d* levels; the other excitation (at ~3.3 *eV* inFigure 1) is a complex quantum mechanical feature containing signatures of the underlying one-particle band structure but also of a coherent and macroscopic nature. Accordingly, the excitation spectra of these materials are complicated many-body probes, ill described with simple models, and revealing subtle features that are inaccessible with traditional one-particle-like probes such as Compton scattering [14] and/or photoemission [15].

In this work, we concentrate on the cases of Ag and Ni. We present both *ab initio* and semi-empirical results for excitation spectra of these systems using realistic band structures and wave functions. To minimize breaks in the conceptual flow of the Chapter

we relegate a large portion of the technical details of the calculations to various Appendices.

We provide microscopic insight into the complex loss spectra of Ag, contrasting our interpretation with that of experiment [9,10,13] and recent theoretical work [17,18]. As well, this work also reveals a limitation of the local density approximation (LDA) [19] in the dynamical context. This breakdown is due to the spurious self-interactions contained in LDA and is partially removed upon performing additional density functional calculations that result in increased binding energies for the 4*d* electrons. Moreover, this semi-empirical approach, discussed in more detail in the Section on Ag, allows us to shed light on the subtleties of the dielectric function and loss function. Corroborating the intuitive view of Ref. [10], we find the intrinsic bandwidth of the 4*d* levels, as manifested in the dielectric function, explains the anomalous dispersion of the nominal plasmon energy. Furthermore, this band structure effect also leads us to predict an anomalous dispersion of the nominal plasmon lifetime that should be observable with single-crystal samples.

In the case of Ni we provide an interpretation of the two prominent loss features present in the excitation spectra at approximately 22 *eV* and 28 *eV* [22] which is distinct from that of previous works. Though these features have been traditionally described as plasma oscillations [22,23], we instead, reveal them to be due to modulations in the

transition strengths involving predominantly $d \rightarrow p$ transitions in a complex phase space of interband transitions. A extensive investigation of matrix elements for the initial and final states involved in these excitations reveals, for the first time, the subtle nature of hybridization as manifested in the dielectric properties.

We conclude this Chapter with a discussion of the techniques of dynamical response. We provide a clear demonstration that *ab initio* pseudopotential-based approaches fail for materials with localized electronic states. This severity of this breakdown correlates with the strength of the non-local pseudopotential used in the ground state calculations and is most severe for the case of Zn. We trace these effects to an improper description of transition matrix elements for excitations involving an extended (*sp*-like) conduction state and a localized hole. The relative success of the pseudopotential method for Ag and Cd is then fortuitous, and is explained in terms of the proximity of the binding energy of the *d*'s to the nominal plasma energy, and the intrinsic strengths of the $3d \rightarrow 4p$ and $4d \rightarrow 5p$ transitions.

THEORETICAL ESSENTIALS

Before discussing our results, we first review the fundamentals of time-dependent density functional theory (TDDFT) [25-28]. It is assumed that the reader is familiar with the density functional theory (DFT) [1,29], appropriate for a, in principle, exact description of the electron charge density of an inhomogeneous system. An outline of the

formalism of the ground state, i.e. DFT, is provided in Appendix H as well as in Chapter Two; for further review the reader is directed to [1].

Time-Dependent Density Functional Theory

Consider a spin compensated system of N electrons interacting via the Coulomb interaction, $v(\vec{x}-\vec{x}')$, and in the presence of a time-dependent, local, external potential $\mathrm{v}_{ext}(\vec{x},t)$. The time dependent Hamiltonian for this system, written in terms of the field operators $\hat{\psi}$ and $\hat{\psi}^{\dagger}$, is (We adopt Hartree atomic units throughout this Thesis.)

$$\hat{H}(t) = -\frac{1}{2}\int d^3x\,\hat{\psi}^{\dagger}(\vec{x})\vec{\nabla}^2\hat{\psi}(\vec{x}) + \int d^3x\,\hat{\psi}^{\dagger}(\vec{x})\hat{\psi}(\vec{x})\,\mathrm{v}_{ext}(\vec{x},t) + \frac{1}{2}\int d^3x\,d^3x'\,\hat{\psi}^{\dagger}(\vec{x})\hat{\psi}^{\dagger}(\vec{x}')v(\vec{x}-\vec{x}')\hat{\psi}(\vec{x}')\hat{\psi}(\vec{x}) \quad . \tag{1}$$

In the time independent case, the external potential typically would correspond to the ionic potential due to the nuclear charge, or, for an extended system, the lattice (crystal) potential. The many-body problem then involves the solution of the time-dependent Schrödinger equation

$$\hat{H}(t)\left|\Psi(t)\right\rangle = i\frac{\partial}{\partial t}\left|\Psi(t)\right\rangle, \tag{2}$$

from which all relevant physical quantities may be obtained as expectation values in the time dependent state $\left|\Psi(t)\right\rangle$. The time dependent charge density, for example, is given by

$$n(\vec{x},t)=\left\langle \Psi(t)\left|\hat{\psi}^{\dagger}(\vec{x})\hat{\psi}(\vec{x})\right|\Psi(t)\right\rangle . \tag{3}$$

As Runge and Gross (RG) argue in their seminal work on TDDFT [25], the solution of the time dependent Schrödinger Eq. (2) with the initial condition specified by the initial state $\left|\Psi(t_o)\right\rangle$, and with the expectation value of Eq. (3) defines a map

$$A_{v+\mathrm{v}} : \mathrm{v}_{ext}(\vec{x},t) \rightarrow n(\vec{x},t) . \tag{4}$$

The central result of TDDFT is RG's proof of the invertibility of the map, $A_{\mathrm{v}+v}$. This invertibility allows one to recast the complex many-body problem solely in terms of the time dependent charge density, $n(\vec{x},t)$ from which all other quantities are, in principle, obtained as functionals.

In the time independent case Hohenberg and Kohn (HK) [29] establish the invertibility of the map, $A_{v+\mathrm{v}}$, by appealing to the Rayleigh-Ritz variational (see Appendix H for more details). This demands that one exclude constant potentials from the space of allowable potentials, since a constant shift of the external potential will have no physical consequences for the electron charge density. As for the time dependent case, we must also exclude constant functions; this includes purely time dependent functions as well. In contrast to the time independent case, one cannot, however, apply a Rayleigh-Ritz principle, as the usual quantum-mechanical action

$$A = \int dt \left\langle \Psi(t) \left| i\frac{\partial}{\partial t} - \hat{H}(t) \right| \Psi(t) \right\rangle, \tag{5}$$

satisfies only a stationary, rather than a minimum principle. Under the assumption of a Taylor series representation of the time evolution of the many-body wave function, RG established the uniqueness (invertibility) of the map A_{v+v}. Moreover, under the assumption of non-interacting v-representability [122], RG demonstrated that the exact time dependent charge density, $n(\vec{x},t)$, can be obtained from a non-interacting reference system as

$$n(\vec{x},t) = \sum_{i=1}^{N} \left| \phi_i(\vec{x},t) \right|^2. \tag{6}$$

The time dependent Kohn-Sham (KS) [19] orbitals, $\phi_i(\vec{x},t)$, are the solutions to a set of time dependent Schrödinger-like equations

$$\left\{ -\frac{1}{2}\vec{\nabla}^2 + v_S[n](\vec{x},t) \right\} \phi_i(\vec{x},t) = i\frac{\partial}{\partial t}\phi_i(\vec{x},t), \tag{7}$$

with the time dependent effective potential

$$v_S[n](\vec{x},t) = v_H[n](\vec{x},t) + v_{xc}[n](\vec{x},t) + \mathrm{v}_{ext}(\vec{x},t). \tag{8}$$

The time dependent Hartree potential, $v_H[n](\vec{x},t)$ is simply

$$v_H[n](\vec{x},t) = \int d^3x' v(\vec{x}-\vec{x}') n(\vec{x}',t), \tag{9}$$

whereas $v_{xc}[n](\vec{x},t)$ is the time dependent exchange-correlation potential. In the time independent case, it is the first variational coefficient of the exchange-correlation energy [1,19]

$$v_{xc}[n](\vec{x}) = \frac{\delta E_{xc}[n]}{\delta n(\vec{x})}, \tag{10}$$

and whose physical content is such to ensure that the time independent KS density

$$n(\vec{x}) = \sum_{i=1}^{occ} \left|\phi_i(\vec{x})\right|^2, \tag{11}$$

is identical to the electron charge density when implemented self-consistently with the exact exchange-correlation energy functional.

Formally, we know that all physical quantities are unique functionals of the time dependent electron charge density and, hence, all of many-body physics could then be viewed as a theory of the exact $v_{xc}[n](\vec{x},t)$. In practice, of course, this is far from realized, for we lack explicit expressions for general physical quantities as functionals of the charge density, and, more importantly, we lack an explicit expression for the exact quantum mechanical action. These unresolved formal issues notwithstanding; we may still endeavor to shed light on microscopic physical phenomena with the formalism of time dependent density functional theory, in particular for dynamical correlation functions

that are appropriate for linear response theory and as measured in inelastic scattering experiments.

Time-Dependent Linear Response

Most of the calculations that have been performed thus far within the TDDFT framework refer to the linear-response domain [16-18,21-24,36-47]. In this case the system is assumed to evolve in the presence of an external potential $\mathrm{v}_{ext}(\vec{x},t) = \mathrm{v}_{ext}(\vec{x}) + \mathrm{v}_1(\vec{x},t)$ containing a time dependent piece, $\mathrm{v}_1(\vec{x},t)$, which is turned on (abruptly) at $t = 0$. If we assume that for $t \le 0$ the system is in its ground state for the external potential $\mathrm{v}_{ext}(\vec{x})$, then $n(\vec{x},t)$ is uniquely determined by the external potential —without a cumbersome dependence on the initial state. We may then introduce the time-dependent density-response function for the interacting system,

$$\chi(\vec{x}t;\vec{x}'t') = \frac{\delta n(\vec{x},t)}{\delta \mathrm{v}_{ext}(\vec{x}',t')} \ , \tag{12}$$

where the functional derivative is to be affected about the ground state density corresponding to the external potential $\mathrm{v}_{ext}(\vec{x})$. Since this potential is in one-to-one correspondence with the ground-state density (by virtue of HK), χ is a functional of the latter. Furthermore, since the one-to-one mapping between time dependent density and external potential also holds in the absence of interactions, we may define the single-particle density-response function $\chi_S(\vec{x}t;\vec{x}'t')$ according to the equation

$$\chi_S\left(\vec{x}t;\vec{x}'t'\right)=\frac{\delta n\left(\vec{x},t\right)}{\delta v_s\left(\vec{x}',t'\right)}\ . \tag{13}$$

Now $\mathrm{v}_{ext}\left(\vec{x},t\right)$ and $v_S\left(\vec{x},t\right)$ are in one-to-one correspondence. This conclusion is crucial, as it allows us to introduce the functional derivative $\delta v_S/\delta \mathrm{v}_{ext}$; making use of the chain rule for functional differentiation, we can then show that the response function χ obeys an integral equation of the form

$$\chi=\chi_S+\chi_S\left(v+f_{xc}\right)\chi\,, \tag{14}$$

where v is the bare Coulomb interaction, and the "dynamical exchange-correlation kernel" f_{xc} is defined by

$$f_{xc}\left(\vec{x}t;\vec{x}'t'\right)=\frac{\delta v_{xc}\left(\vec{x},t\right)}{\delta n\left(\vec{x}',t'\right)}. \tag{15}$$

Equations (12)-(15) define a formally exact linear-response scheme. Contact with experiment is immediate, as the inelastic-scattering cross section for x-rays and fast electrons is proportional to the dynamical structure factor $S\left(\vec{Q},E\right)\sim \mathrm{Im}\,\chi$ as we discuss in the following Section. The two "material-dependent" building blocks of the physical response χ are the KS density-response function $\chi_S\left(\vec{x},\vec{x}'\middle|E\right)$ and the exchange-correlation kernel $f_{xc}\left(\vec{x},\vec{x}'\middle|E\right)$. The former is determined once we pick a "model" (e.g., LDA) for the correlations built into the ground-state exchange-correlation potential $v_{xc}\left(\vec{x}\right)$; the latter accounts for all the explicit effects of dynamical correlations.

Connection with Spectroscopic Probes of the Two-Particle Type

The double differential cross section, $d^2\sigma / dEd\Omega$, which is probed in inelastic scattering experiments, be it IXS or EELS, is proportional to the so-called dynamical structure factor, $S\left(\vec{Q},E\right)$. Consider a scattering event in which energy and momentum transferred to the system are E and $\vec{Q}$, respectively. The double differential cross-section takes the form [48]

$$\frac{d^2\sigma}{dEd\Omega} = AS\left(\vec{Q},E\right). \tag{16}$$

The proportionality factor, A, depends only on the beam-target coupling and the geometry of the scattering experiment, whereas $S\left(\vec{Q},E\right)$ is an intrinsic property, i.e. for the materials in isolation, of the system to which the probe couples. In the case of IXS, the proportionality factor in Eq. (16) is just the Thomson-scattering cross section

$$A_{\mathrm{IXS}} = \left(d\sigma / d\Omega\right)_{Th} = \alpha^2 \left(\varepsilon_1 \cdot \varepsilon_2\right)^2 E_2 / E_1,$$

with α the fine structure constant ($\approx 1/137$), ε_1 and ε_2 are the polarization vectors for the incoming and outgoing photon states with energies E_1 and E_2 respectively. In the case of EELS, the proportionality factor, g, takes a form similar to that for Møller scattering

$$A_{\mathrm{EELS}} = \left(\frac{d\sigma}{d\Omega}\right)_{Møller} = -k' v_{\vec{Q}}^2 / 4\pi^3 k,$$

with k and k' the momentum of the incoming and outgoing electron, respectively, and $v_{\vec{Q}}$ is the Fourier coefficient of the Coulomb potential. Moreover, the dynamical structure factor is proportional to the dynamical density response function introduced in Eq. (13)

$$S\left(\vec{Q},E\right) = -2\Omega \,\mathrm{Im}\,\chi_{\vec{G},\vec{G}}\left(\vec{q},E\right), \tag{17}$$

with $\vec{Q} = \vec{q} + \vec{G}$, and $\chi_{\vec{G},\vec{G}}\left(\vec{q},E\right)$ the space-time Fourier transform of the density response function. This conclusion is critical for it allows experiment to probe a microscopic quantity, χ, with macroscopic measurements. By macroscopic, here we have in mind that one only need measure two asymptotic photon (electron) states in IXS (EELS) in order to determine the loss spectra.

The dielectric function, ε, is a further useful quantity for analyzing the properties of the excitation spectra; it allows for a concise discussion of the physics of the systems in question with a microscopic view of both the single-particle and many-particle nature of the excitation spectra. The dielectric function satisfies the following well-known exact relationship to the density response function

$$\varepsilon^{-1} = 1 + v\chi. \tag{18}$$

In discussing the results of our calculations, as well as for unambiguous comparison to experiment (note that the dielectric function is dimensionless.), we find it

more convenient to refer to the *loss function*, $\mathrm{Im}\,\varepsilon^{-1}$, which, by Eqs. (17) and (18), is also proportional to the dynamical structure factor, and hence the double differential cross section. In the homogeneous electron gas, the real part of the dielectric function has root associated with the energy for plasma oscillations

$$\mathrm{Re}\,\varepsilon\left(\omega_p\right)=0\,, \tag{19}$$

with $\omega_p^2=4\pi\bar{n}$ and $\bar{n}$ is the average electron density; the corresponding loss function then has a single peak, of zero width, referred to as the plasmon, which is a collective excitation of coherent and macroscopic nature. In a real material, the crystal potential provides for decay channels (interband transitions) that are absent in the electron gas and these damping mechanisms then give rise to a finite linewidth in the loss function, whose peak position is also shifted relative to the "natural" frequency defined by Eq. (19). In general we will then use the language "natural" frequency to refer to frequencies determined by the condition of Eq. (19) and reserved the term plasmon energy or plasma frequency to refer to peak positions in the loss spectra.

The spectral representation of χ_s is of the usual form; for the case of a perfectly-periodic crystal, its space and time Fourier transform takes on the form [24]

$$\chi_{S,\vec{G},\vec{G}'}(\vec{q},E)=\frac{2}{\Omega}\sum_{\vec{k}}\sum_{n,n'}\frac{f_{\vec{k},n}-f_{\vec{k}+\vec{q},n'}}{E_{\vec{k},n}-E_{\vec{k}+\vec{q},n'}+E+i0^{+}}\left\langle \vec{k},n\left|e^{-i\left(\vec{q}+\vec{G}\right)\cdot\hat{\vec{x}}}\right|\vec{k}+\vec{q},n'\right\rangle$$
$$\text{x}\quad\left\langle \vec{k}+\vec{q},n'\left|e^{i\left(\vec{q}+\vec{G}'\right)\cdot\hat{\vec{x}}}\right|\vec{k},n\right\rangle\ , \tag{20}$$

where the kets $\left|\vec{k},n\right\rangle$ refer to Kohn-Sham Bloch states ("orbitals"), the wave vector $\vec{k}$ lies in the first Brillouin zone (BZ), *n* is a band index, $f_{\vec{k},n}$ is the occupation (1 or 0) of state $\left(\vec{k},n\right)$, and the factor of 2 accounts for spin degeneracy. In Eq. (20) the "external" wave vector $\vec{q}$ is also in the BZ, and $\vec{G},\vec{G}'$ are vectors of the reciprocal lattice. In the representation introduced in Eq. (20), the integral equation for χ becomes a matrix equation for its Fourier coefficients, $\chi_{\vec{G},\vec{G}'}$.

Note that $\mathrm{Im}\,\chi_S$ is the product of three terms that enforce fundamental physical laws for the non-interacting KS system: (ii) the Pauli exclusion principle, (ii) energy conservation and (iii) crystal momentum conservation. The Pauli exclusion principle, enforced by the term ($f_{\vec{k},n}-f_{\vec{k}+\vec{q},n'}$), reflects that we can only have single-particle excitations from occupied to unoccupied states. Energy conservation, contained in the term $\left(E_{\vec{k},n}-E_{\vec{k}+\vec{q},n'}+E+i0^{+}\right)^{-1}$, accounts for the phase space of kinematically accessible transitions, whereas crystal momentum conservation is ensured via the matrix elements $\left\langle \vec{k},n\left|e^{i\vec{q}\cdot\hat{\vec{x}}}\right|\vec{k}+\vec{q},\vec{n}\right\rangle$ and accounts for the spatial overlap of the single-particle orbitals involved in the excitations.

With these matrix elements, we find it useful to introduce the transition strengths,

$$f_{n,n'}\left(\vec{k}\mid\vec{q}\right)\equiv\left|\left\langle\vec{k},n\left|e^{i\vec{q}\cdot\vec{x}}\right|\vec{k}+\vec{q},n'\right\rangle\right|^2. \tag{21}$$

This notation should not be confused with that of the Fermi occupation factors, $f_{\vec{k},n}$, or the term "oscillator strength", which, by convention, generally refers to $v_{\vec{q}}\, f_{n,n'}\left(\vec{k}\mid\vec{q}\right)$. For the homogeneous electron gas, the transition strengths are unity for kinematically allowed intraband transitions, and zero otherwise. This is, of course, just a reflection of the fact that momentum is a good quantum number for the homogeneous system. For an inhomogeneous system, interband transitions are possible and vary in strength from zero to unity, as determined by the momentum content of the initial and final single-particle states. A proper treatment of the transition strengths is required in order to fulfill conservation of particle number, via the f-sum rule, and hence, they are a crucial ingredient in an *ab initio* description of the response function.

All-Electron Approach

To date, most *ab initio* studies [17,18,21,24-41] of the dynamical response of periodic crystals have been implemented with use of *ab initio* pseudopotentials [49]. Correspondingly, the calculations have been predominantly carried out in a plane wave basis. Such approach considerably simplifies the evaluation of the Kohn-Sham ground state, and leads to relatively simple algorithms for the evaluation of the response. Recently, making use of the virtues of modern "ultra-soft" pseudopotentials, response calculations for Cu and Ag have also been carried out in a plane wave basis [17, 18]. A

mixed-basis approach involving plane waves and localized Gaussians was recently utilized for the study of the response of semiconducting compounds such as CdTe Ref. [21].

A more general and powerful —albeit technically more complex— approach to the self-consistent study of bonding and dynamical response in systems with *d*-like electronic states, is the all-electron approach. Our viewpoint in this work is that the price paid in effort of algorithm development is well rewarded by the much smaller size (*vs*. the plane wave approach) of the basis set required to study the metals of interest to the current investigations. Most importantly, the method allows for an unbiased description of the dual localized-itinerant nature of *d*-like electronic states in transition metals such as Ni. Furthermore, as we explain in the Section Two of this Chapter, all-electron techniques prove to be an absolute necessity for a truly microscopic understanding of the physics of the $e^{-}h$ continuum for systems with localized electronic states.

We have developed dynamical-response algorithms within the *full-potential* linearized augmented plane wave (FLAPW) method [50,51]. The label "full potential" refers to the fact that no shape approximation is made in evaluating the potential or electron density in the self-consistent solution of the Kohn-Sham problem. The "local-orbital" enhancement of the FLAPW method due to Singh [52] is extremely well-suited for our purposes, as it allows us to treat the response of semi-core states on the same

footing with that of the valence states. Moreover, as explained in Appendix E, this basis set enhancement proves to be crucial for accurate descriptions of high-energy excitations as well. In the Appendices, we provide details of the numerical calculations and a discussion of the LAPW basis. A derivation of the matrix elements of Eq. (21) in the LAPW approach is given in Appendix E, a discussion of the use of symmetry in evaluating these matrix elements in Appendices A, B and E, and other technical details of the calculations which would digress too much from the main line of discussion of this Chapter. We direct the reader to the appropriate Appendix and/or references when needed.

I. THRESHOLD EFFECT AND PLASMA OSCILLATIONS

To date most calculations of dynamical response for solids have been implemented within the so-called time-dependent local-density approximation (TDLDA), which was introduced phenomenologically [53] before the formal development of TDDFT. In the TDLDA, the KS response is constructed from the knowledge of the LDA band structure and associated one-particle orbitals; as for the exchange-correlation kernel, f_{xc}, its frequency dependence is ignored ("adiabatic approximation"), as is its spatial non-locality. For simple metals [37,39-43], semiconductors [38], and clusters of these materials [56], the TDLDA performs well, by comparison with experiment.

Now, as suggested in the Introduction, the TDLDA fails qualitatively for the case of Ag, as is discussed below. Its limitations are also apparent for the other metals we have investigated as we briefly discuss in the summary remarks for this Chapter. Related problems with the LDA have been encountered in the recent literature in the case of semiconducting compounds such as CdTe, stemming from the presence of cation 4*d* electrons [21]. The issue of how to go beyond the LDA in the present dynamical context is a highly non-trivial one. Clearly, beyond-the-LDA physics is contained in both the exact Kohn-Sham response and in the exact many-body kernel. Perturbative improvements to the LDA in terms of generalized-gradient corrections (GGA's) of increasing sophistication have been developed in recent years. GGA's —which we have also implemented in our ground-state calculations— play a minor role in the dynamical-response studies reported herein, since they give rise to small shifts of the LDA eigenvalues corresponding to flat bands. Consequently, and for brevity, we make no further reference to this issue.

On the other hand, in the discussion of Ag below we present a semi-empirical exploration of "beyond-the-LDA-physics" for the dynamical response of extended systems, motivated by recently reported work for simpler systems such as atoms [54,55]. The issue of whether further progress in the study of excitation energies of the N -particle system via Eq. (14) will come from improvements in the description of the "ground-state" correlations built into $v_{xc}(\vec{x})$ or from new approximations for the dynamical kernel

$f_{xc}(E)$ has been discussed at some length recently. Van Gisbergen *et al.* [54] have presented *ab initio* results for small atoms based on the evaluation of the exact $v_{xc}(\vec{x})$, obtained "working backwards" from the knowledge of the exact ground-state density [55]. These authors concluded that the quality of the excitation energies is determined mainly by the quality of the $v_{xc}(\vec{x})$ used in evaluating the ground state, and hence χ_S. Although we are aware of other recent work in which the role of the exchange-correlation kernel was found to be important for the singlet-triplet splitting in He and Be atomic systems [56], the results of Van Gisbergen *et al*. are suggestive that $f_{xc}(E)$ may play only a minor role in the excitation spectra of solid systems. The exchange-correlation potential then plays a direct and critical role in the theoretically determined excitation spectra.

As well, one could justify this viewpoint with the argument that RPA-type physics will dominate the loss spectra in the long wavelength limit. Since the Coulomb potential diverges like $1/\vec{q}^2$ in this limit, and since there is no known model of the exchange-correlation kernel that can compete with this effect (see Eq. (14)), we can expect to identify features in χ directly with the "bare" Coulomb interaction and the one-particle band structure. Motivated by this viewpoint we present "beyond-TDLDA" results for the case of Ag obtained on the basis of self-consistent band structure calculations, involving *d*-band shifts which increase the binding energy of the *d* levels.

With one parameter, fixed by the long wavelength experimental EELS results, we perform a series of response calculations over a large phase space of energy and momentum. The results of these calculations agree quantitatively with experiment and shed new light on the physics of Ag, including a discussion of the anomalous dispersion of the plasmon observed in EELS experiments [10] and the prediction of an anomalous dispersion of the plasmon lifetime; this new feature is understood on a conceptual basis similar to that invoked in Ref. [10] to explain the dispersion of the plasmon energy.

Ag – *d*-plasmons

Recent TDLDA results for the dielectric and loss functions of Ag have been reported [17, 18]. Based on a model Hamiltonian, involving plasmons and a continuum of oscillators, with minimal coupling of these two types of excitations, Cazalilla *et al*. gave a qualitative account of the complex frequency dependence of their TDLDA results for Ag. These authors refer to the low energy resonance observed in Ag as a polaron-like mode involving vibration of the conduction electrons independently of the 4*d* electrons. However, in that work it is clear that the *ab initio* line shape, in particular, the low energy resonance at ~3.8 *eV* is markedly different than that of the experimentally determined [9,10] spectra (see for example Figs. 4 and 6 of Ref. [17]). It is suggested by the authors of Ref. [17] that this difference could be due to an inadequate description of the "strong

correlations occurring amongst the electrons in the flat *d*-like bands of Ag" as described, for example, in the LDA.

The optical properties of Ag are well known [13]; Ehrenreich and Philipp (ER), in their pioneering work with reflectance spectroscopy, describe the loss function of Ag in terms of two modes of excitation of the many body system. They note that the nominal plasmon energy of the *sp* electrons of Ag is 9.08 *eV*; accounting for a polarizable core background suggests a decrease of the plasma frequency by $1/\varepsilon_c$, with ε_c the polarizability of the *d*-electrons. This simple model is too crude in that it lacks the salient features of the first principles results as described next and in Ref. [17]; however, it is useful for a qualitative explanation of the red shift of the "*sp*-plasmon" defined below, and is consistent with the trends observed experimentally and theoretically for a variety of systems [17,62]. In the present work we shed light on the critical role that the 4*d* binding energies play in the complex line shape of the experimental loss spectra, including this red shift; our findings are consistent with the speculation of Ref. [17] that the LDA poorly describes the 4*d* levels. We also indicate how ours results suggest a different interpretation from that of ER. The methods used are similar to those recently reported for the case of Zn [45-47] in which the $X\alpha$ approach [58] is used to yield loss spectra which emulates experiment.

In Figure 2 we display the loss function of Ag as determined experimentally [59] as well as present results for the TDLDA loss spectra (dotted line). Also shown in Figure 2 is the loss spectra obtained based on the $X\alpha$ approximation (dashed line). We first discuss the comparison of the TDLDA results relative to experiment. It is quite clear that both the TDLDA and experiment show two loss features in the energy range between 3 and 8 *eV*. However, the energy position and intensity in the TDLDA loss spectra, especially for the low energy resonance, is a poor approximation to the experimental spectra. Now, it is well known [9-13,17,18] that the low energy resonance in Ag is quite sensitive to the energy location of the occupied *d*-bands. Thus, as we outlined above, we view this discrepancy as a signature of the inadequacy of the LDA exchange-correlation potential.

To circumvent this deficiency with the LDA, we adopt an $X\alpha$ treatment [58] to shift the 4*d* bands relative to the *sp* bands by adjusting the α parameter in the $X\alpha$ exchange-correlation potential

$$v_{xc}^{X\alpha}[n](\vec{x}) = \frac{3}{2}\alpha v_x^{KS}[n](\vec{x}). \tag{22}$$

In Eq. (22) v_x^{KS} is the KS exchange potential [19]

$$v_x^{KS}[n](\vec{x}) = -\left(\frac{3}{2\pi}\right)\left\{3\pi^2 n(\vec{x})\right\}^{1/3}. \tag{23}$$

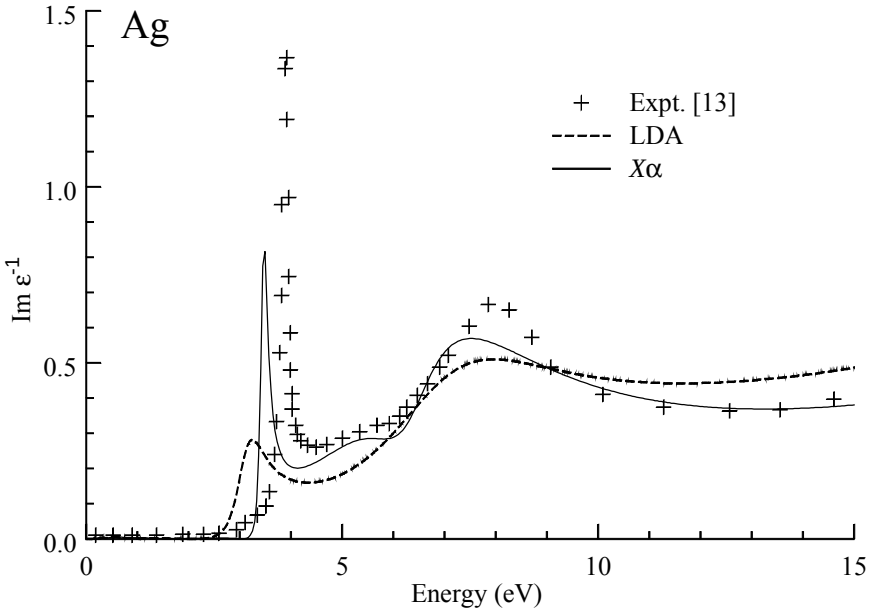

Figure 2 Loss function of Ag for $\vec{q} \approx 0$. Theoretical results obtained in the local density approximation (dashed line) and the $X\alpha$ approximation for $\vec{q} = 2\pi(1,1,1)/20a$. The experimental spectra are taken from Ref. [13].

For $\alpha = 1$ in Eq. (23) we have "Slater exchange", originally obtained [58] by minimizing the total energy with an effective potential obtained as the average Fock potential for the occupied orbitals. For $\alpha = 2/3$, we have KS exchange, obtained by minimizing the total energy with a local effective potential taken to be the value of the Fock potential for the highest occupied orbital [19].

The value of α for the present work has been optimized to achieve the best possible agreement between the theoretical loss spectra (as obtained from the self-consistently computed $X\alpha$ ground state) and experimental loss spectra at $\vec{q} \approx 0$ (Figure 2), while at the same time leaving unaffected the effective mass at the Fermi level or bandwidth of the *sp*-electrons. In this respect, the calculations are semi-empirical.

The value of α obtained in the above procedure is also consistent with the criterion of a self-interaction-free theory put forth by Perdew and Zunger [60]. In the LDA, the exchange-correlation energy for the occupied orbitals does not exactly cancel the self-Hartree-energy; thus the LDA KS orbitals see their own bare field directly. This effect increases the orbital energy of the occupied levels; the effect is also most severe for localized states. By performing additional self-consistent *atomic* calculations for Ag in the $X\alpha$ approximation, optimizing α under the requirement that the electrostatic and exchange-correlation energy for the valence orbitals exactly cancel [60]

$$U\left[n_v^\alpha\right]+E_{xc}^{X\alpha}\left[n_v^\alpha\right]=0\,, \tag{24}$$

we account for, in a phenomenological fashion, the spurious self-interactions which are present in LDA-based calculations. In Eq. (24) the notation, $n_v^\alpha(\vec{x})$, is used to denote that the orbital density, $\left|\phi_v(\vec{x})\right|^2$, is recomputed self-consistently in the atomic KS ground state for the specified value of α. The optimal value of α from this procedure yields values in the range of 0.9 to 1.0 [61], whereas our results for the crystal yield $\alpha=0.82$. The fact that the atomic results suggest a value that is larger than its crystal counterpart is consistent with our physical picture that the extended states in the crystal suffer less from the self-interaction.

In Figure 3a we show the LDA band structure, while Figure 3b is the $X\alpha$ band structure for $\alpha=0.82$. In comparison to the LDA results, the 4*d* levels in the $X\alpha$ results are roughly 1 *eV* lower. Note that the bandwidth of the 4*d* levels in the $X\alpha$ is also nearly 1 *eV* smaller relative to the LDA. The topology of the rest of the bands is essentially unaffected, in particular the effective mass at the Fermi level or the valence bandwidth.

Returning to Figure 2, we note that the loss function obtained from the $X\alpha$ band structure is in much better agreement with the experimental results. In particular, the line shape of the low energy resonance is much narrower and more intense; both of these

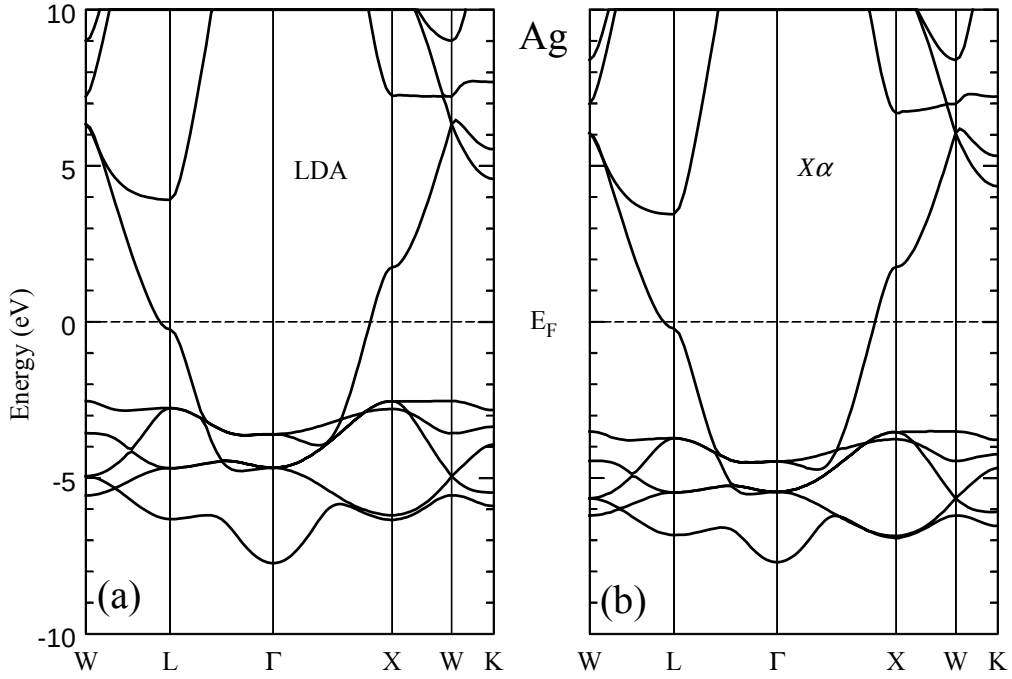

Figure 3 Band structure of Ag in the LDA (left panel) and the $X\alpha$ for $\alpha = 0.82$ (right panel). The zero of energy has been normalized to the Fermi level for both results.

trends are in agreement with experiment. As well, the high-energy portion of the spectrum is better described in the $X\alpha$ results. We discuss next, from a microscopic point of view, the underlying subtleties in the two respective dielectric functions that result in such distinct loss functions.

Figure 4 displays the TDLDA (dashed lines) and $X\alpha$ (solid lines) dielectric function and loss functions. The upper panel concentrates on the dielectric function, while the lower panel only shows the corresponding loss functions. The vertical scale of the upper panel has been chosen to emphasize the frequency region between 2 and 10 *eV*. The large feature in $\mathrm{Im}\,\varepsilon$ for energies between 0 and 2 *eV* is the conventional Lindhard-like peak; it has been truncated vertically for the purposes of the figure. Both calculations have a natural frequency at approximately 3.4 *eV* (For a reminder of the definition of the term "natural" frequency, see Eq. (19) and the discussion that follows it); however $\mathrm{Im}\,\varepsilon$ for the two calculations is quite different. The lineshape in $\mathrm{Im}\,\varepsilon$ beginning at 2.5 *eV* and 3.0 *eV* in the LDA and $X\alpha$, respectively, is due to interband transitions involving occupied *d*-levels. Therefore, it is clear that the reason for the difference between the LDA and $X\alpha$ loss spectra is due primarily to the large "damping channel" available in the former for energies just below the natural frequency predicted by the LDA. Furthermore, the slope of $\mathrm{Re}\,\varepsilon$ near the natural frequencies is also quite different in the two calculations. As a result, relative to the $X\alpha$ spectra, the low energy

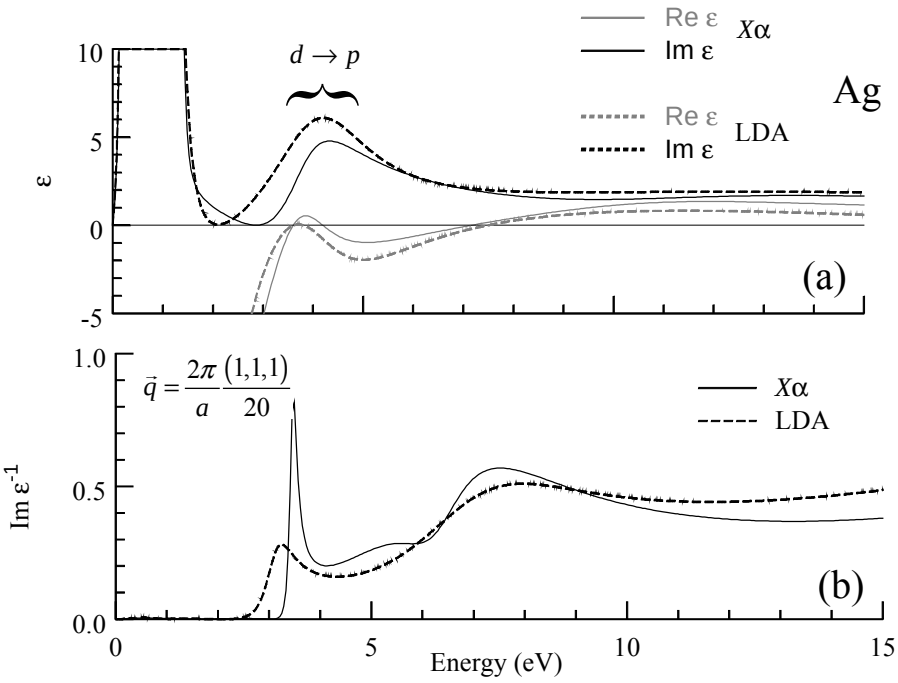

Figure 4. Dielectric function (upper panel) and loss function (lower panel) of Ag as obtained in the LDA and $X\alpha$ approximations. Upper panel- Solid lines correspond to results obtained in the $X\alpha$ approximation, while the dashed lines are the corresponding LDA results. Lower panel- Solid line is the loss function obtained based on the $X\alpha$ ground state, while the LDA result is shown as a dashed line.

resonance is red shifted, reduced in intensity, and significantly broadened. The stronger coupling to electron-hole pairs, via $\mathrm{Im}\,\varepsilon$, and polarization effects, via the slope of $\mathrm{Re}\,\varepsilon$ in the vicinity of $\mathrm{Re}\,\varepsilon = 0$ are essentially what distinguish the LDA and $X\alpha$ loss spectra.

As it sheds intuitive light on the predicted dispersion of the two main loss features, we first discuss the physical interpretation of the low energy resonance. For small wave vectors, this resonance falls just below the binding energy of the 4*d* levels measured by photoelectron spectroscopy [63,64]. Moreover, it is also outside the *sp*-electron contribution to the $e^{-}h$ continuum. Correspondingly, there are very few damping channels available and the low energy feature is, thus, quite narrow. Above threshold for *d*-electron excitation, there are large contributions to the $e^{-}h$ continuum from the 4*d* levels, and the density of such decay channels is quite large as the transition strengths of the *d*-electron transitions to *p*-like states at the Fermi surface is enhanced according to dipole selection rules. Thus the high-energy tail of this features will be significantly broadened. For reasons that will become clear as we discuss the loss spectra, we will refer to this feature as a *d*-plasmon, while the resonance at ~7.8 *eV* is more aptly referred to as an *sp*-plasmon.

In Figure 5 we display the experimentally determined dispersion (crosses) for the *sp*- and *d*-plasmons [10] compared to the present $X\alpha$ results (circles) along the (111) direction. Also shown is the nominal dispersion (solid curve) obtained by modeling the

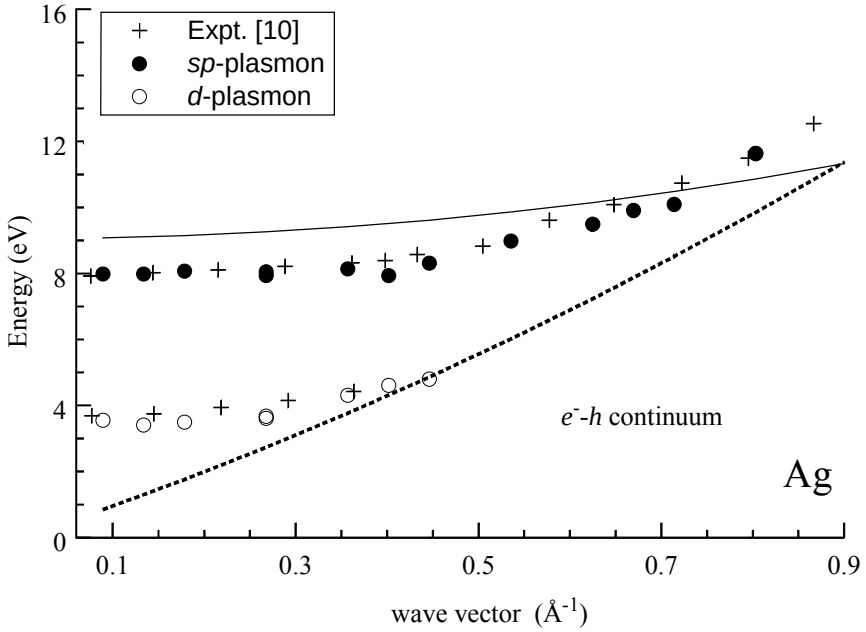

Figure 5 Dispersion of loss features of Ag. Present results in the $X\alpha$ approximation (solid circles) are compared to experimentally determined [10] dispersions (crosses). For reference is also shown the nominal plasmon dispersion assuming each Ag atom to be a monovalent electron gas, as well as the *e-h* continuum (see text) from the present *ab initio* results.

conduction electrons of Ag as an electron gas with each atom contributing one electron to the Fermi sea; the corresponding electron-hole ($e^{-}h$) continuum is the region to the right of the dashed curve. Note that although the *d*-plasmon dispersion is quite flat, it actually has a quadratic dispersion with a dispersion coefficient determined from experiment to be 0.76 [10]. The calculations suggest that this weak dispersion is a consequence of the wave vector dependence of the *sp*-electron-hole contribution, rather than a result of the intrinsic wave vector dependence of the *d*-electron interband transitions. This is also consistent with the fact that the *d* bands are fairly non-dispersive and oscillator strengths, $v_{\vec{q}} f_{n,n'}\left(\vec{k} \mid \vec{q}\right)$ are only weakly $\vec{q}$ independent. Compared to experiment the predicted energy dispersion for the *d*-plasmon is too low. There is also much more fine structure in the predicted dispersion; we come back to this point in the conclusions of this Section and of Chapter One. For our purposes though, these results serve as a critical test of our numerical techniques for the transition strengths since it reproduces the experimental dispersion quite well.

In Figure 6 we have the dielectric function and loss function for two wave vectors along the (111) direction. Figure 6a shows the dielectric function for $\vec{q} = 2\pi(111)/20a$, and Figure 6b is the corresponding loss function. Note the "energy gap" between the Lindhard-like peak and the onset of *d*-electron interband transitions. In Figure 6c and Figure 6d are shown the dielectric function and loss function for $\vec{q} = 2\pi(333)/20a$.

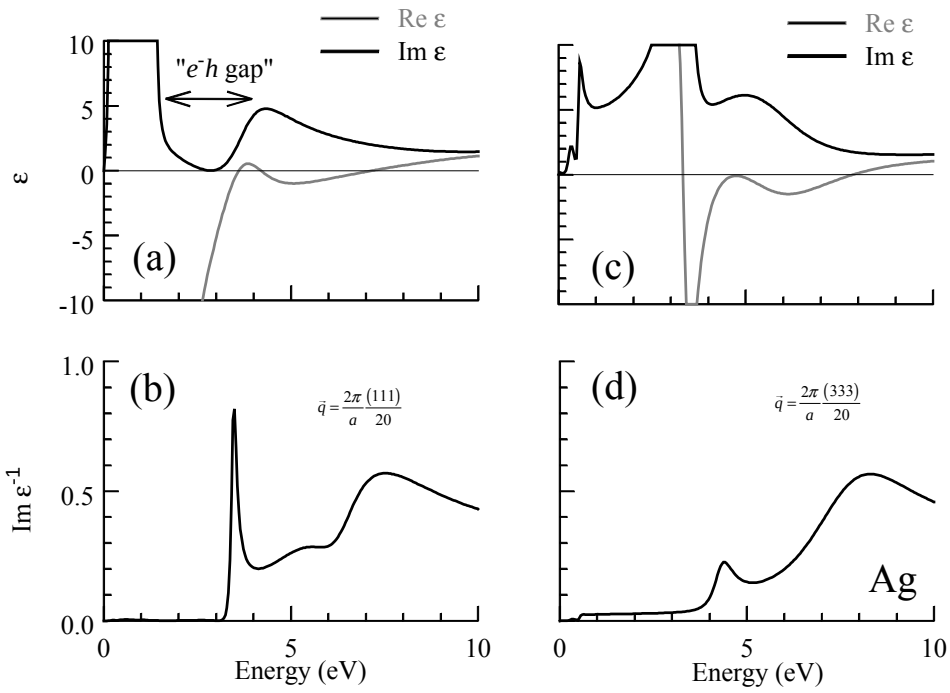

Figure 6 Loss functions and dielectric functions for Ag for two wave vectors obtained in along the (111) direction. All results are obtained based on the $X\alpha$ band structure and wave functions. Panel (a). $\mathrm{Re}\,\varepsilon$ (gray line) and $\mathrm{Im}\,\varepsilon$ (black line) for $\vec{q} = 2\pi(1,1,1)/20a$. Note the electron-hole "gap" between ~1.5 *eV* to ~3 *eV*. Panel (b). Loss function for $\vec{q} = 2\pi(1,1,1)/20a$. Panel (c). $\mathrm{Re}\,\varepsilon$ (gray line) and $\mathrm{Im}\,\varepsilon$ (black line) for $\vec{q} = 2\pi(3,3,3)/20a$. Note that the *sp* electron-hole continuum has dispersed into the *d*-electron interband transition region. Panel (d). Loss function for $\vec{q} = 2\pi(3,3,3)/20a$.

We see that, in comparison of Figure 6a and Figure 6c, the "energy gap" is closed as the *sp* $e^{-}h$ continuum disperses with wave vector.

The triple root structure of $\mathrm{Re}\,\varepsilon$ in Figure 6a is quite different from all previous works. On the experimental side, the interpretation of optical data by forth by ER is very different. From their reflectance data, ER constructed the dielectric function of Ag finding the *sp*-plasmon mode is not associated with a natural frequency of the system (see Fig. 2 of Ref. [13]) and with only one natural frequency associated with the *d* electrons . Clearly, the present results do not support this picture entirely, for we have clearly defined resonance frequencies in the range of 8 *eV* to 9 *eV* over a large range of wave vectors as well as a double root associated with the *d* electrons. On the theoretical side, the only other *ab initio* work on Ag is that of Ref. [17,18]. Figure 6 of Ref. [17] displays a double root in the TDLDA dielectric function in the region of the *d*-electron threshold, but this is, in fact, a numerical artifact associated with the use of pseudo wave functions in the evaluation of the transition strengths of Eq. (20) as we discuss in the Section II of this Chapter. The all-electron TDLDA result has only a single root (see 0 and the second Section of this Chapter) to be compared with the double root of the $X\alpha$ dielectric function.

The final point we wish to discuss is of similar physical origin as the anomalous dispersion of the energy of the *sp*-plasmon [10]. Figure 7 shows the loss function for

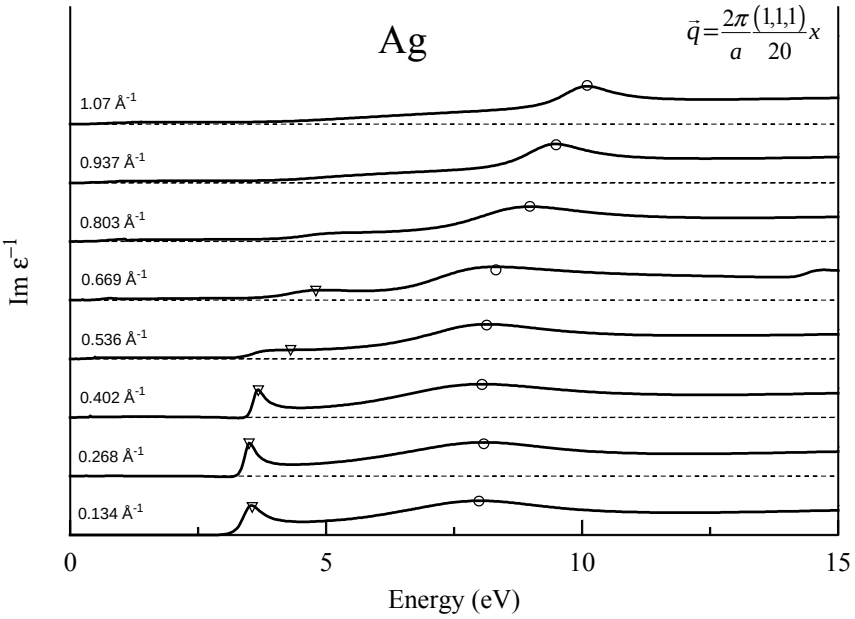

Figure 7 Line shape of the loss function along the (111) momentum direction. For reference is shown the plasmon frequencies for the *sp*-plasmon (open circles) and the *d*-plasmon (open triangles). The curves have been adjusted on the vertical scale for presentation purpose.

wave vectors along the (111) direction. As the wave vector is increased from $0.134\mathring{A}^{-1}$ to $0.670\mathring{A}^{-1}$ the *sp*-plasmon line width narrows. This narrowing is quantified via a calculation of an effective line width, Δ, defined as

$$\Delta = \mathrm{Im}(\varepsilon)\,\mathrm{x}\left(\frac{\partial \mathrm{Re}\varepsilon}{\partial \omega}\right)^{-1}\Bigg|_{\omega_p}, \tag{25}$$

where the real and imaginary parts of the dielectric function are to be evaluated at the natural frequency in question. Equation (25) is motivated by formal work on the lifetime of the plasmon in inhomogeneous systems [62]. As a testament to its utility, we note that this definition gives the full width at half-maximum of the plasmon peak in the loss function in a simple system such as Na or K, for which the peak is nearly symmetric. In these same systems $\mathrm{Im}\,\varepsilon$ is approximately constant in the neighborhood of ω_p and $\mathrm{Re}\,\varepsilon$ is a monotonically increasing function near ω_p.

With the present results for the dielectric function, we have computed Δ for wave vectors along the (111) direction. The results are shown in Figure 8 as open symbols; the line through the points is a guide to the eye. For reference we display the plasmon dispersions and the *ab initio* $e^{-}h$ continuum (shaded contours). Note that the line width as defined above is monotonically decreasing for wave vectors up to approximately 0.5 $\mathring{A}^{-1}$, at which point it starts to increase. The increase above 0.5 $\mathring{A}^{-1}$ is understood as Landau damping provided by the background of *sp* and *d* electrons. The decrease for momenta

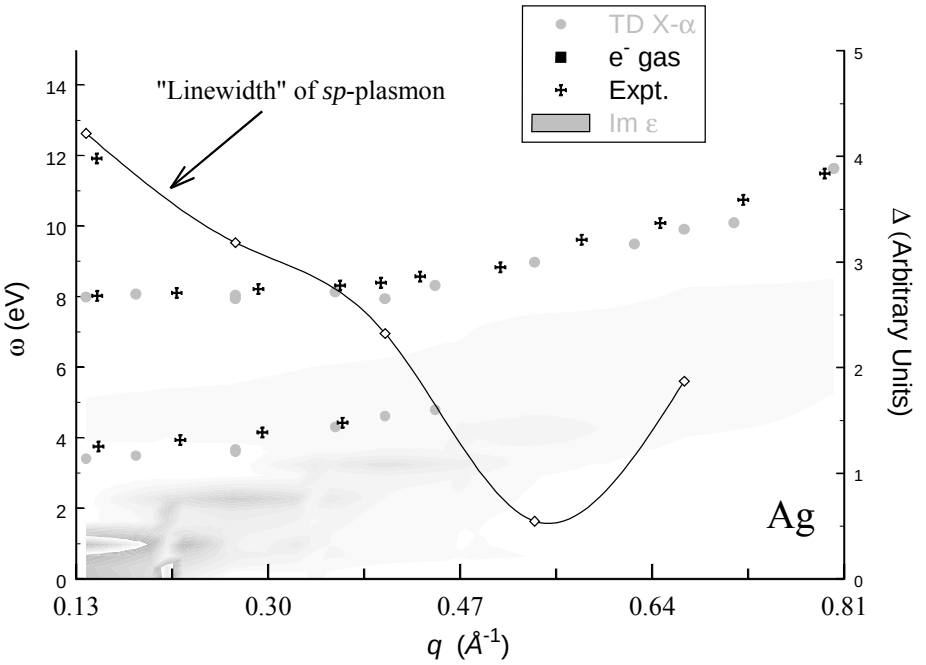

Figure 8 Dispersion of the *sp*- and *d*-plasmons with the electron-hole continuum. The effective line width, Δ, of the *sp*-plasmon is also shown (see text for details) plotted against the right vertical axis.

up to this point is understood on the basis of the dielectric function. With reference to Figure 6a, note that the *d*-electron contribution is peaked between 3.0 and 6.0 *eV*, the binding energy plus bandwidth of the valence 4*d*-levels. Hence, as the *sp*-plasmon disperses with momentum it will leave the energy range for which the coupling to *d*-electrons is strong, entering a domain where $\mathrm{Im}\,\varepsilon$ is still appreciable, but featureless. In addition, at these intermediate momenta the screening provided by the *sp*-electrons, being modulated by the presence of the 4*d*'s, is incomplete and gives rise to a steeper slope in $\mathrm{Re}\,\varepsilon$ compared to the same for small momenta. The combination of these two effects, damping which decreases for increasing momentum and enhanced polarization effects at large momentum, leads to the behavior predicted in Figure 7 and Figure 8. It does not appear from the experimental data [10] that this effect has been observed; however, the energy resolution of the only available data is quite poor (0.8 – 1.0 *eV*) and has only been taken on polycrystalline samples. We come back to this point as well in the conclusions for Section I of this Chapter; for now we move to the case of Ni to discuss prominent loss features observed in this material.

Ni – final state effects

There are two key points to be made in presenting our results in light of the only other previous theoretical study of the loss spectra of Ni [16]. First, we have evaluated χ_S in the highly accurate LAPW+LO basis [50,52]. Secondly, we give a detailed discussion of the dielectric function as it relates to the two main loss features observed

experimentally [22]. We present a new understanding of these features, with an interpretation of them rooted in the modulation of $3d \rightarrow 4p$ excitations embedded in a rather featureless background of interband transitions. We discuss the band structure and density of states (DOS) as they relate to these coherent and incoherent aspects of the loss function and hybridization effects which enter through the transition strengths.

In Figure 9a we display $\mathrm{Im}\,\varepsilon^{-1}$ as obtained in the TDLDA (solid line) with the recent theoretical study of Ref. [16] (dashed line) for a small wave vector. The loss spectra of Ref. [16] was evaluated in the LMTO basis; to our knowledge it is the only other theoretical study of the dynamical excitation spectra of Ni. The two results are in qualitative agreement for the intensity and energy location of the two main loss features. There is, however, a shift of the position of the two peaks in the present work to lower energies compared to the results of Ref. [16]. We argue in Appendix E that the present results are numerically more accurate.

In Figure 9b we show $\mathrm{Im}\,\varepsilon^{-1}$ determined by EELS (crosses) [22] as well as the present results. Note that the EELS data are for $\vec{q} = 0$ while our results (solid line) are for a small, but finite, wave vector ($\vec{q} = 2\pi(111)/20a$). Although there is considerably more fine structure in the theoretical spectra, both the experimental results and the present work show a broad spectrum with a prominent dip at 22 *eV*. Some of the fine structure in the present work is due to the numerical sampling of the BZ [66]. The two prominent

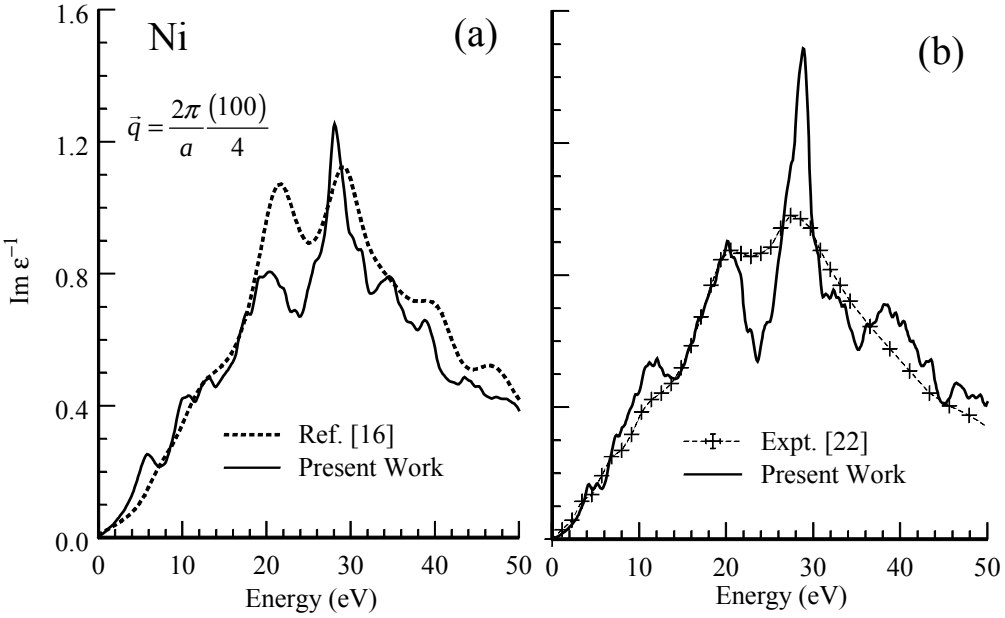

Figure 9 Loss function for Ni. Left panel. Comparison of the present results to that of Ref. [16] for $\vec{q} = 2\pi(1,1,1)/4a$. Right panel. Comparison of the present results to that of a experimentally determined EELS spectra [22]. Note that the experimental spectra correspond to $\vec{q} \approx 0$ while the theoretical results are obtained for a small but finite momentum, $\vec{q} = 2\pi(1,1,1)/4a$.

features are, however, clearly of physical origin and have been discussed at great length in Ref. [16]. The experimental spectra suffer from poor instrumental resolution, with a width in the range of 1 to 1.5 *eV* [22]; this would account for appreciable broadening in the loss spectra of Figure 9b. Note, however, that the width of the two main loss features is much larger and can be attributed to physics rather than the resolution function of the experiment. We also note that these two loss features are reasonably well reproduced by the TDLDA results. We discuss our interpretation of these features via phase space and hybridization arguments in the following paragraphs.

The complex form of the loss function for the energies between 20 and 30 *eV* can be understood qualitatively by examining the LDA band structure and density of states (DOS),

$$\rho(E) = \sum_{\vec{k},n} \delta\left(E - E_{\vec{k},n}\right), \tag{26}$$

which are shown together in Figure 10a and Figure 10b [67]. In Eq. (26), the sum is over the eigenstates, $\left|\vec{k},n\right\rangle$, of the KS Hamiltonian. The shaded region between 22 *eV* and 28 *eV* in Figure 10b is important for the loss features we discuss below. Also shown is the angular decomposition of the DOS for angular momentum, l,

$$\rho_l(E) = \sum_{\vec{k},n} \delta\left(E - E_{\vec{k},n}\right)\left\langle \vec{k},n\left|\hat{Y}_{l0}\right|\vec{k},n\right\rangle_I, \tag{27}$$

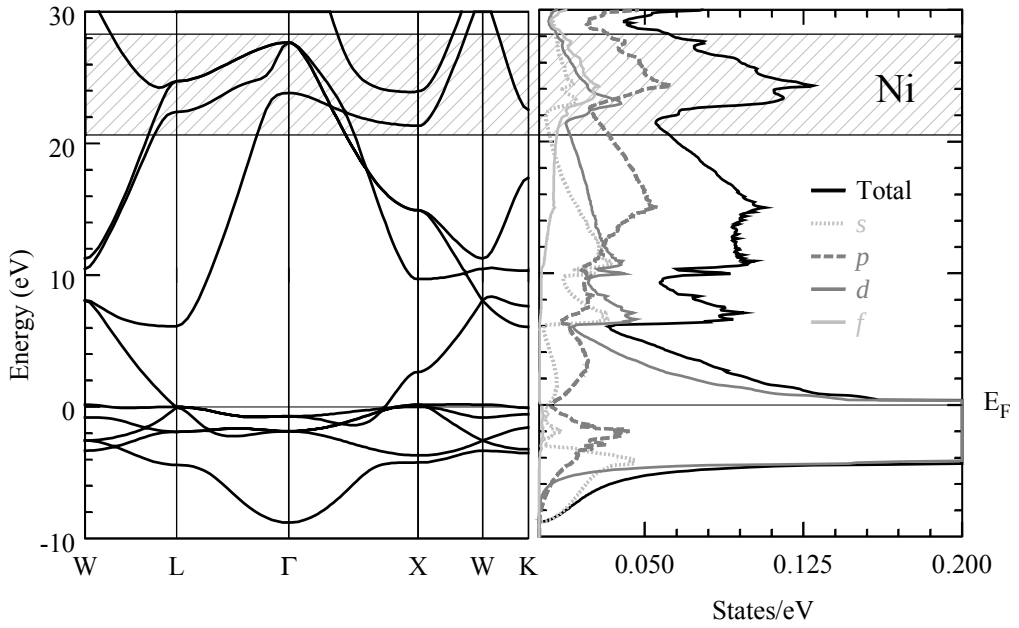

Figure 10 Band structure and density of states (DOS) of Ni as obtained in the local density approximation. Left panel. Electronic structure along high symmetry directions in the BZ. The region shaded between ~22 and ~28 *eV* is important for the dielectric and loss functions (see text). Right panel. DOS of Ni as obtained in the LDA. The angular decomposition of the DOS is shown as well (see text for details).

with $\hat{Y}_{lm}$ a spherical harmonic. By the convention of the WIEN [51] ground state program, the matrix element, $\left\langle \vec{k},n\left|\hat{Y}_{l0}\right|\vec{k},n\right\rangle_I$ considers only contributions from the atomic spheres; thus Eq. (26) can be thought of as a "local" DOS, projected onto the atomic sites. Inspection of $\rho_l(E)$, in particular, for energies between 22 and 28 eV above the Fermi level, reveals a local maximum that is predominantly of *p* and *f* angular character. Correspondingly, the joint density of states (JDOS),

$$\rho_{jdos}(E)=\sum_{\vec{k},n,n'}\left[f_{\vec{k},n}-f_{\vec{k},n'}\right]\delta\left(E+E_{\vec{k},n}-E_{\vec{k},n'}\right)\left|f_{n,n'}\left(\vec{k}\mid\vec{0}\right)\right|^2, \tag{28}$$

displays a local maximum for this same energy range of interest as a result of transitions from the occupied *d*-levels to the large density final states of *p* and *f* symmetry. This is consistent with dipole selection rules ($l\leftrightarrow l\pm1$); however, because of significant hybridization effects in both the initial states and final states, there are competing contributions from $s\leftrightarrow p$, $p\leftrightarrow d$ and $d\leftrightarrow f$ excitations. This competition manifests itself in the transition strengths and is, of course, absent in model calculations based on the electron gas. Before discussing in detail the transition strengths of Ni, we first provide some more general insight into the form of the loss and dielectric functions.

In Figure 11 we show ε for the same wave vector as that of Figure 9b. The vertical scale of the plot has been chosen to emphasize the frequency range between 20

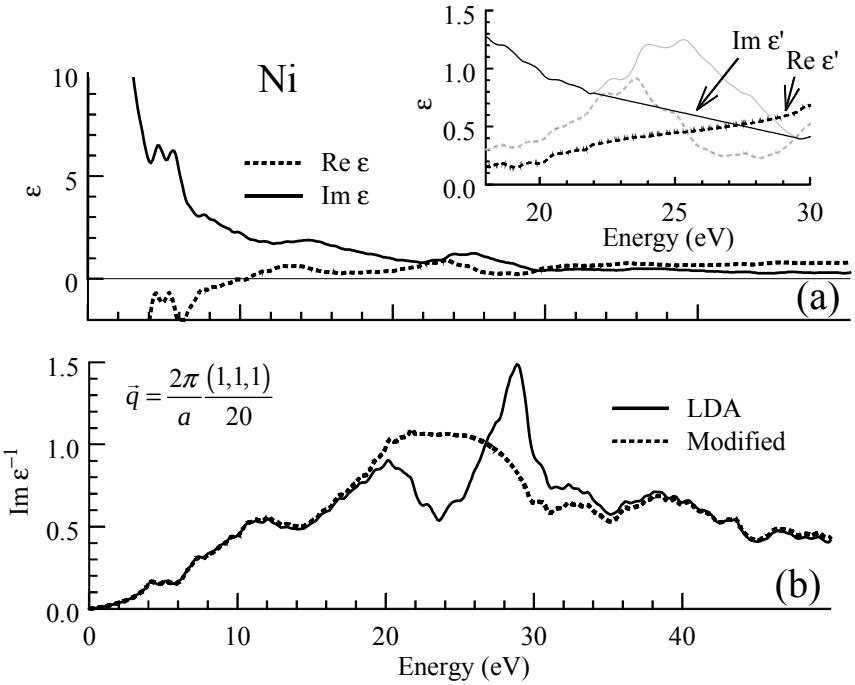

Figure 11 Dielectric function and loss function of Ni. Upper panel. $\mathrm{Re}\,\varepsilon$ (solid line) and $\mathrm{Im}\,\varepsilon$ (dashed line) for $\vec{q} = 2\pi(1,1,1)/20a$. Inset. $\mathrm{Re}\,\varepsilon$ (light dashed line) and $\mathrm{Im}\,\varepsilon$ (light solid line) as obtained in the TDLDA contrasted with a model calculation of $\mathrm{Re}\,\varepsilon'$ (dashed line) and $\mathrm{Im}\,\varepsilon'$ (solid line). Lower panel. Loss function of Ni as obtained in the TDLDA (solid line) and a model calculation (dashed line) (see text).

and 30 *eV*. The local maximum in the DOS (and the JDOS) reflects itself in the local maximum in $\mathrm{Im}\,\varepsilon$ centered at approximately 25 *eV*. Correspondingly, $\mathrm{Re}\,\varepsilon$ exhibits two local minima in this energy range. Other than being a result of the Kramers-Kronig (KK) relationship between $\mathrm{Re}\,\chi_S$ and $\mathrm{Im}\,\chi_S$, this modulation in $\mathrm{Re}\,\varepsilon$ can be interpreted as a local manifestation of incomplete screening for energies just above and just below the relevant "resonance" energy. That is to say, if one applied an external field to the Ni crystal for frequencies in the range of 22 to 28 *eV*, the electrons are less effective in screening this perturbation (gauged by the proximity of $\mathrm{Re}\,\varepsilon$ to zero) for energies in the neighborhood of the resonance energy. The combination of these two features, a local maximum in $\mathrm{Im}\,\varepsilon$ and the local minima in $\mathrm{Re}\,\varepsilon$, leads to the two peaks in the loss function of Figure 11. Clearly then, these features clearly reveal the third energy scale relevant to Figure 1 for which *final state effects* are as important as initial states. We come back to this point in the conclusions of this Chapter. Similar phenomena have been observed in a variety of other 3*d* and 4*d* metals, including Ni [16], Pd [24], Ag [17] and Cu [18] and even for NiO [16].

In the inset to Figure 11a, we present a numerical model of the dielectric function designed to elucidate the complexity of the first principles results. This numerical model differs from the first principles result in that the imaginary part ($\mathrm{Im}\,\varepsilon'$) has been interpolated to a straight line between 22 and 28 *eV*; the corresponding real part ($\mathrm{Re}\,\varepsilon'$) is obtained by on the basis of the KK relationship between $\mathrm{Re}\,\chi_S$ and $\mathrm{Im}\,\chi_S$. We then

evaluate the corresponding loss function (dashed line) shown in Figure 11b. Physically, this model dielectric function corresponds to either a suppression of the transition strengths for the relevant single-particle excitations, or a reduction in the density of final states, or both effects taken together. Note that the loss function which corresponds to this modified dielectric function has, instead of the two peaks at ~20 and ~30 *eV*, a broad peak of FWHM of ~10 *eV* centered at 22 *eV*. Clearly, interband transitions are responsible for the existence of this broad loss. Therefore it seems reasonable, to refer to the two loss features present in the full evaluation of $\mathrm{Im}\,\varepsilon^{-1}$, as a single peak due to interband transitions, which is modulated by resonance excitations involving the occupied *d*-levels. From other systems we have investigated, including Pd, Ag and Cu, this appears to be a universal feature of select $3d$ and $4d$ systems, reflecting strong interband transitions of the form $3d \to 4p, 4f$ and $4d \to 5p, 5f$.

Further insight into the complex line shape of the loss function of Ni is gained by closer inspection of the transition strengths. In Figure 12 we have the transition strengths for the wave vector corresponding to that of Figure 11, plotted versus the KS excitation energies for the transition $\left(\vec{k}, n\right) \to \left(\vec{k}+\vec{q}, n'\right)$, defined by

$$E_{n,n'}\left(\vec{k}, \vec{k}+\vec{q}\right) = E_{\vec{k}+\vec{q},n'} - E_{\vec{k},n'}\,. \tag{29}$$

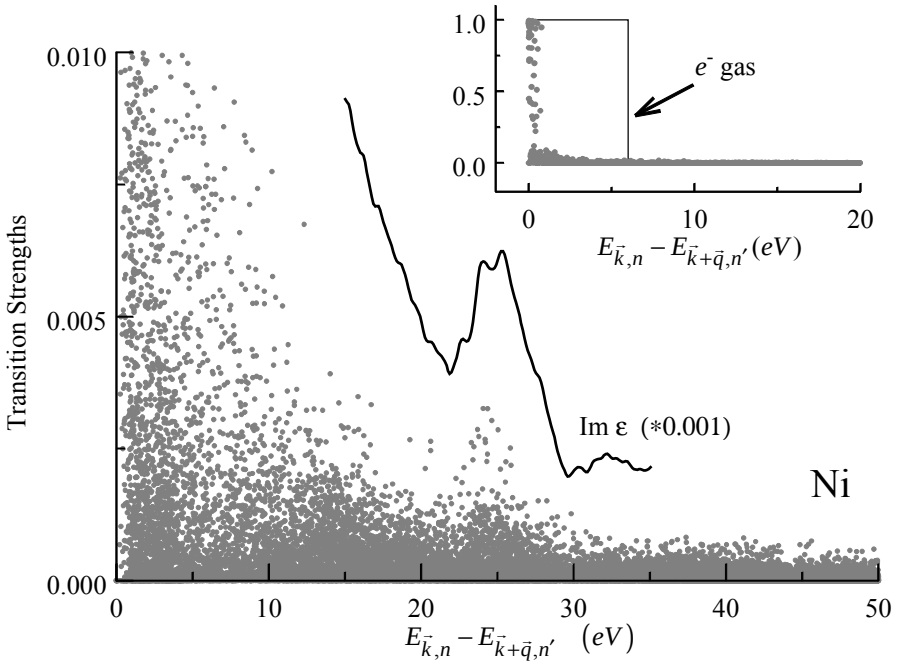

Figure 12 The transition strengths of Ni plotted versus the corresponding KS excitation energies, $E_{\vec{k},n} - E_{\vec{k}+\vec{q},n'}$ (see text). Solid line is $\mathrm{Im}\,\varepsilon$ in arbitrary units. The inset displays the transition strengths of Ni contrasted with electron gas results for the *sp*-electrons.

Also shown for the purposes of illustration, is $\mathrm{Im}\,\varepsilon$ for energies between 15 and 35 *eV* on a separate vertical scale chosen to emphasize energies in the neighborhood of the two loss features. The inset to Figure 12 shows the transition strengths on an expanded vertical scale; we also show the transition strengths that result from modeling the *sp* electrons of Ni as a homogeneous electron gas. Note that there is an intrinsic energy dependence in the transition strengths, which display a local maximum between 22 and 28 *eV*. This reflects a local enhancement in the probability for crystal momentum conservation and is a subtle feature that has never been revealed to date. Therefore, the complex frequency dependence of $\mathrm{Re}\,\varepsilon$ and $\mathrm{Im}\,\varepsilon$ for energies between 22 and 28 *eV* is determined by local enhancements in both the DOS (which provides a large density of final states) and in $f_{n,n'}$ (which is a reflection of hybridization). We note that, although not explicitly shown here, the transition strengths for Pd show a similar behavior.

In conclusion, we provide a quantitative assessment of the distribution of spectral weight in the excitation spectra of Ni. In a simple metal, the plasmon mode saturates the f-sum rule, and the distribution of spectral weight is very nearly a step function, the step taking place at the plasmon energy. The distribution of spectral weight can be quantified through an evaluation of a wave vector- and energy-dependent effective "charge density"

$$n_{eff}(\vec{q},\omega) = \frac{1}{2\pi}\int_0^{\omega} \omega' \,\mathrm{Im}\,\varepsilon^{-1}(\vec{q},\omega')\,d\omega' . \qquad (30)$$

Though the language suggests otherwise, one should not interpret $n_{eff}(\vec{q},\omega)$ as a physical charge density; it is a cumulative spectral weight which has often [10,13,69] been used for determining the physical nature of peaks in the measured loss spectra.

The loss function of Ni (solid line) along with this effective charge (dotted) is shown in Figure 13. In the inset is the same quantities evaluated for Al. Both the main plot and the inset are evaluated for a small wave vector, and the right hand axes (on which $n_{eff}(\vec{q},\omega)/n_{eff}(\vec{q},\infty)$ are plotted) are normalized via the first frequency moment sum rule

$$\int_{-\infty}^{+\infty} d\omega \,\mathrm{Im}\,\varepsilon^{-1}(\vec{q}\,|\,\omega) = \omega_p^2 \,. \tag{31}$$

with the plasma frequency $\omega_p^2 = 4\pi\overline{n}$. Clearly, the case of Al is very nearly a perfect realization of an electron gas. In contrast, $n_{eff}(\vec{q},\omega)$ for Ni is quite featureless; in particular, the lack of any significant structure in $n_{eff}(\vec{q},\omega)$ between 22 and 28 *eV* lends further support to our interpretation of the loss function of Ni.

Conclusions for Section I

We conclude Section I with a summary of the most salient concepts that we have been revealed with the present theoretical approach applied to the excitation spectra of Ag and Ni.

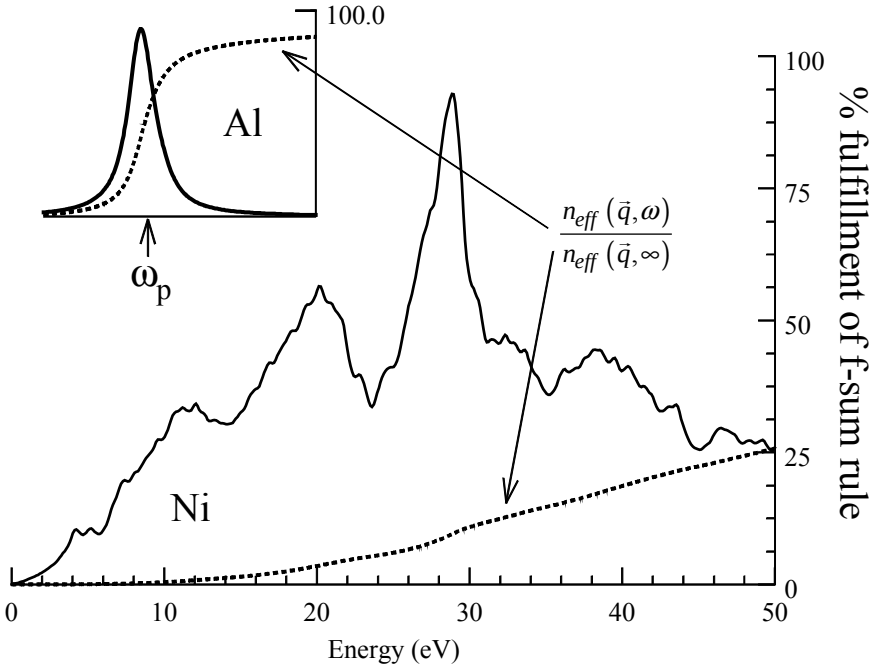

Figure 13 Loss function and spectral weight function normalized by the f-sum rule. The spectral weight function of Ni (dashed line) is displayed with the corresponding loss function. The inset displays the loss function and spectral weight function for Al normalized in the same fashion.

Corroborating the intuitive view of ER, we find that the charge density and band structure of Ag satisfies the conditions necessary for plasma oscillation at two distinct frequencies as observed in the loss function. The dielectric function supports the existence of two "natural" frequencies involving resonant excitation of the *d* electrons and a frequency for plasma oscillations akin to the free electron value. The large density of decay channels available to the *sp*-plasmon provided by interband transitions involving the 4*d* electrons, has an intrinsic line shape set by the band structure of the occupied *d*-levels. This band structure effect accounts for the anomalous dispersion of the *sp*-plasmon energy [10]. As well this leads us to predict an anomalous dispersion of the lifetime of the *sp*-plasmon. High-resolution IXS experiments on single crystal samples would certainly benefit our microscopic understanding of the loss spectra of Ag, in particular for the lifetime of the *sp* and *d* plasmons and to delineate crystalline effects from that of correlation in the fine structure of the predicted dispersion.

The case of Ni reveals a third relevant energy scale for materials in the 3*d* and 4*d* metals, involving final state effects. These effects are controlled by phase space (the proximity of the *d* levels to the Fermi level) and hybridization (manifested in the transition strengths). This energy scale is reflected in the two loss features observed by EELS and is of physical nature quite distinct from plasma oscillations. High-resolution experiments for single crystal Ni samples for energies in the range of 0-20 *eV* would certainly help elucidate whether the low energy excitations observed in Pd [69] are

universal to the case of Ni [70] as well as a better understanding of the intrinsic line widths seen in the loss spectra.

Before concluding this Chapter we argue for the necessity of the all-electron method in these systems. We reveal a fundamental problem with pseudopotential-derived response properties of systems with localized electronic states.

II. ALL-ELECTRON AND PSEUDOPOTENTIAL RESPONSE

As already discussed in Section I of this Chapter, most *ab initio* studies [17,18,21,24-41] of the loss function and dielectric function of crystals have been implemented using band structures and wave functions obtained with *ab initio* pseudopotentials. The success of the pseudopotential method for ground state problems in a variety of systems including alkali metals, simple metals, semiconductors and even 3*d* and 4*d* metals notwithstanding, there are not any systematic studies on the quality of the pseudopotential-based response. Indeed this is a fundamental question, when one considers that central to the modern approach to pseudopotential theory is the use of non-local potentials [49,71,72] for "pseudizing" the ground state, although DFT has only been established for local potentials. The lack of any systematic comparison mainly stems from the complexity of all-electron methods; to our knowledge, the only other response studies implemented with all-electron techniques are those of Refs. [16,42,44]. This is of even more immediate interest when one considers that a variety of popular many-body

approaches, including quasiparticle techniques such as the *GW* approximation and density functional techniques, such as the optimized potential method, depend explicitly on the response of the system. Thus, there is a clear need for comparison of the response properties as predicted in the two methods [73]; this is especially true in materials such as the 3*d*'s and 4*d*'s where the non-local component of the pseudopotential is strong and thus we could expect the two methods to differ.

In this Section, we provide specific examples of the comparison of response functions obtained based on all-electron and pseudopotential band structures and wave functions. These comparisons reveal a fundamental problem with pseudopotential-based technique for the 3*d* and 4*d* metals that is particularly severe for the case o f Zn. We first discuss the technicalities of the calculations referring the reader to the appropriate Appendices for more detailed discussion of derivations, algorithms, etc. We then discuss the cases of Ag, Cd and Zn, providing detailed comparisons of the electronic structures, dielectric functions, loss functions and transition strengths.

Technical Details

The results presented herein are based on the same all-electron method discussed in Section I of this Chapter, whereas the pseudopotential method is discussed in more detail in Chapter Two. Briefly, ee make use of the full potential linearized augmented plane wave (FLAPW) method for the all-electron calculations [50,51,52]. For the

corresponding pseudopotential evaluations we make use of a plane wave based algorithm [76,77] and *ab initio* norm-conserving pseudopotentials [71]. We do not include a non-linear core correction [79] for any of the results presented here. We find these corrections, although they are known to be important for elastic properties [80], have little or no impact on the band structure or dielectric properties; for brevity we make no further reference to this issue. We adopt a notation convenient for the rest of this Chapter in which results obtained using all-electron wave functions, energies and band structures will be denoted LAPW; quantities obtained on the basis of matrix elements in the pseudopotential approach will be denote PSPW.

Ag

Consider the LDA band structure of Ag as shown in Figure 14 for both the pseudopotential [81] and all-electron band structures and wave functions. Note the excellent agreement for wave vectors throughout the zone, for both the occupied and unoccupied levels; the largest differences are on the order of 200 *meV*.

In Figure 15, we plot the TDLDA loss function of Ag for $\vec{q} = 2\pi(1,1,1)/20a$ obtained with the all-electron (solid line) and pseudopotential approaches (dashed line) [82]. For reference is also shown the nominal plasma energy obtained by modeling the *sp* electrons of Ag as a homogeneous electron gas. The two main features at ~3.2 *eV* and ~7.5 *eV* are of a collective nature; they are discussed in detail in Section I of this Chapter.

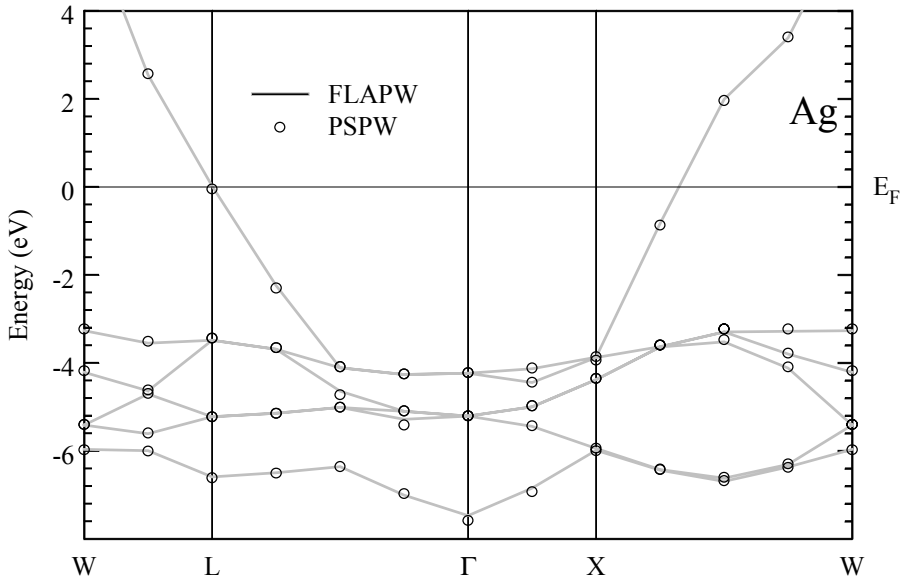

Figure 14 LDA band structure of Ag. All-electron results (solid line) are contrasted with pseudopotential results (dashed line).

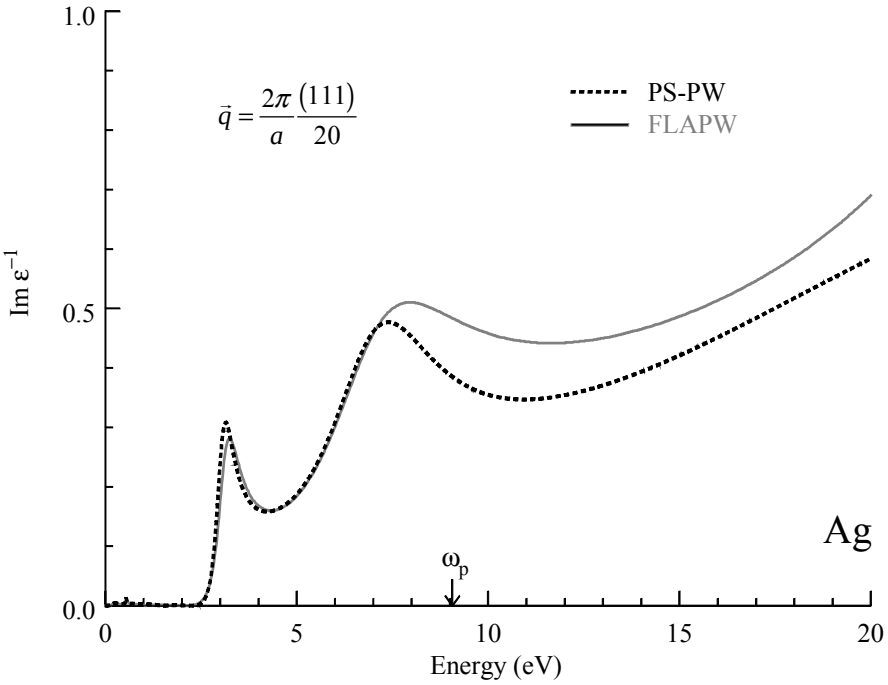

Figure 15 Loss function of Ag obtained in the TDLDA for $\vec{q} = 2\pi(1,1,1)/20a$. The all-electron result (LAPW) is given by the solid line, while the pseudopotential result (PSPW) is the dashed line. For reference, the nominal plasmon frequency is denoted (see text).

For our purposes here, it suffices to say that the low energy resonance, a "*d*-plasmon", is extremely sensitive to the binding energy of the *4d* electrons, while the high energy, resonance is an over-damped plasmon. Note that the pseudopotential results trace rather well the all-electron loss function, especially for energies up to 7 *eV*. Note that the *sp*-plasmon energy (defined as the position of the peak intensity in the loss function) is shifted to lower frequencies in the pseudopotential result. Moreover, the pseudopotential result fails to provide the correct line shape of the plasmon, predicting its lifetime (inverse of the line width) to be significantly larger. As well, the portion of the spectrum for energies comparable to, and larger than, the *sp*-plasma resonance shows too little intensity relative to the all-electron result. Physically this corresponds to a larger dielectric screening in the "pseudized" system compared to that of the true (all-electron) system.

The dielectric function of Ag for $\vec{q} = 2\pi(1,1,1)/20a$ is shown in Figure 16 from the all-electron (solid lines) and pseudopotential approaches (dashed lines). For energies for which transitions involving the *sp*-electrons are dominant (0-2 *eV*) the two results are nearly identical; however, for energies in the neighborhood of the *d*-electron interband transition, the two approaches are qualitatively different, especially for the predicted behavior of $\mathrm{Re}\,\varepsilon$. The pseudopotential-based result suggests two natural frequencies at roughly 3 and 4 *eV* associated with the *d* electrons, whereas the all-electron result has but

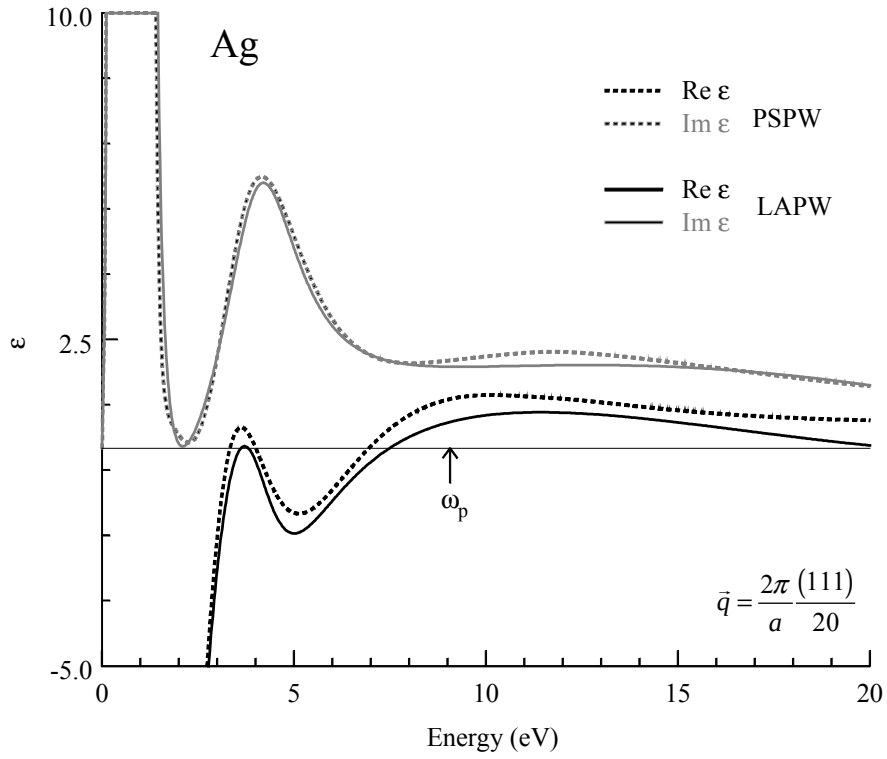

Figure 16 Dielectric function of Ag for $\vec{q} = 2\pi(1,1,1)/20a$. The all-electron results (LAPW) are given by the black and gray lines for the real ($\mathrm{Re}\,\varepsilon$) and imaginary ($\mathrm{Im}\,\varepsilon$) parts respectively, while the pseudopotential results (PSPW) are shown using a dashed black line for the real part and a dashed gray line for the imaginary part.

a single natural frequency associated with *d* electron transitions. There are also clear differences in $\mathrm{Im}\,\varepsilon$, especially for energies between 10 *eV* and 15 *eV*. Concomitant is a red shift of the *sp*-plasmon energy in the pseudopotential results relative to the all-electron values.

These results can be understood in terms of the transition strengths obtained in the two methods. In Figure 17 we compare the all-electron (small black diamonds) and pseudopotential (full gray circles) transition strengths. These are plotted versus the corresponding KS excitation energies, $E_{\vec{k},n} - E_{\vec{k}+\vec{q},n'}$. For low energies the transition strengths are very similar; near the threshold energy for *d*-electron excitations, the pseudopotential results are noticeably larger than the all-electron results. There are also numerical differences for larger energies, the pseudopotential are larger than the all-electron results for energies of 8 *eV* and higher.

Cd

In Figure 18 we compare the LDA band structure of Cd from the all-electron (solid lines) and pseudopotential [84] (dashed lines) ground states. The agreement is quantitatively as good as that obtained for Ag, with differences in the two methods of the order of 200 *meV*.

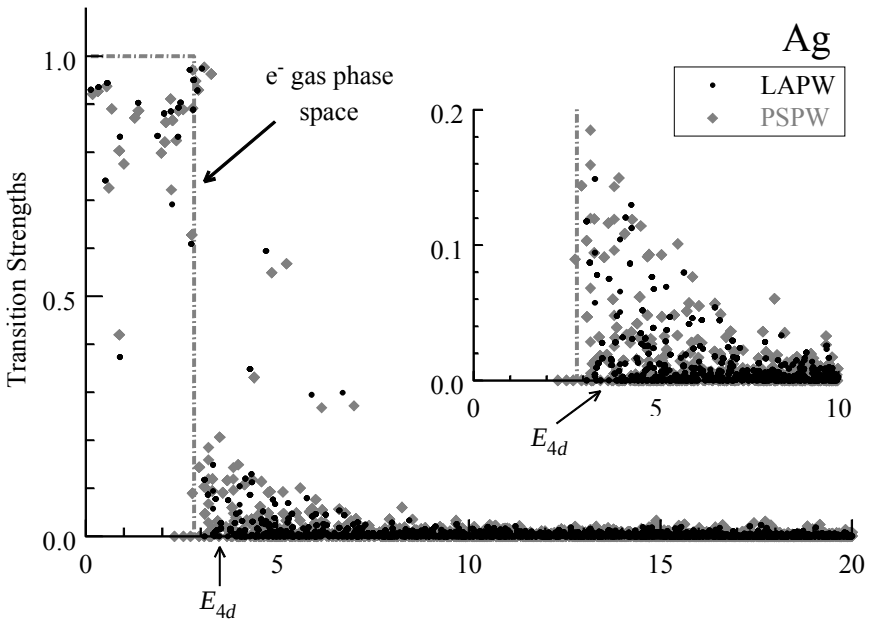

Figure 17 Comparison of the transition strengths, $f_{n,n'}\left(\vec{k}\,|\,\vec{q}\right)$, (see text) of Ag obtained with the all-electron (small black dots) and pseudopotential (full gray circles) methods versus the corresponding Kohn-Sham excitation energies, $E_{\vec{k},n} - E_{\vec{k}+\vec{q},n'}$, for $\vec{q} = 2\pi\left(1,1,1\right)/8a$. For reference, the results for the non-interacting electron gas (dashed line) are shown, as well as the LDA binding energy of the 4*d*-electrons. The inset shows the same but on a reduced horizontal and vertical scale to emphasize the region near the threshold for excitation of *d* electrons.

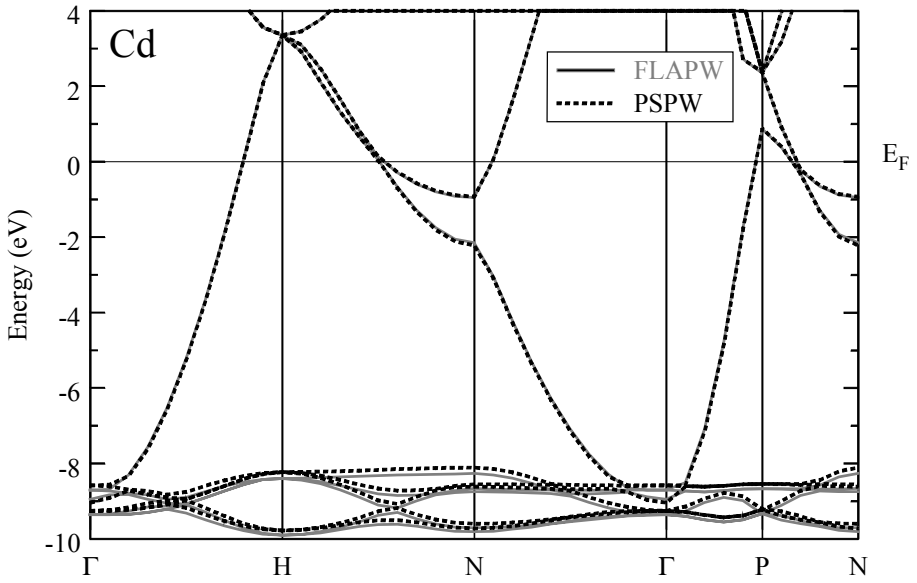

Figure 18 LDA band structure of Cd. All-electron results (solid line) are contrasted with *ab initio* pseudopotential results (dashed line).

We proceed to discuss the loss function as shown in Figure 19. Note that the loss function has a sharp onset at ~8 *eV*, which is due to excitations involving the 4*d* electrons. In the absence of these transitions, Cd would have a plasmon loss feature at ~11.4 *eV* corresponding the oscillation of the *sp*-electrons. As we discuss next, the 4*d* electron interband transitions enhance the dynamical screening so dramatically that the *sp*-plasmon is no longer well defined.

Consider the dielectric function of Cd shown in Figure 20 obtained with the all-electron and pseudopotential band structures and wave functions. The natural frequencies attributed to the *d*-electrons are nearly the same in the two calculations. By contrast, for larger energies the two results disagree; the all-electron results predict a modulation in both $\mathrm{Re}\,\varepsilon$ and $\mathrm{Im}\,\varepsilon$ around 13 *eV*. This feature is quite subtle, and is due to a complicated interplay between band structure effects and the Coulomb interaction. We come back to discuss this remnant of the *sp*-plasmon at the end of this Section.

With reference to the transition strengths, as shown in Figure 21, we note that the two methods yield similar results for small energies, but there are notable departures in the two especially for energies comparable to and above the binding energy of the 4*d*'s. For reference in Figure 21 we also denote the transition strengths appropriate for the *sp* electrons of Cd and the binding energy of 4*d* levels. The inset shows the same on a reduced vertical and horizontal scale to emphasize the region near the 4*d* binding energy.

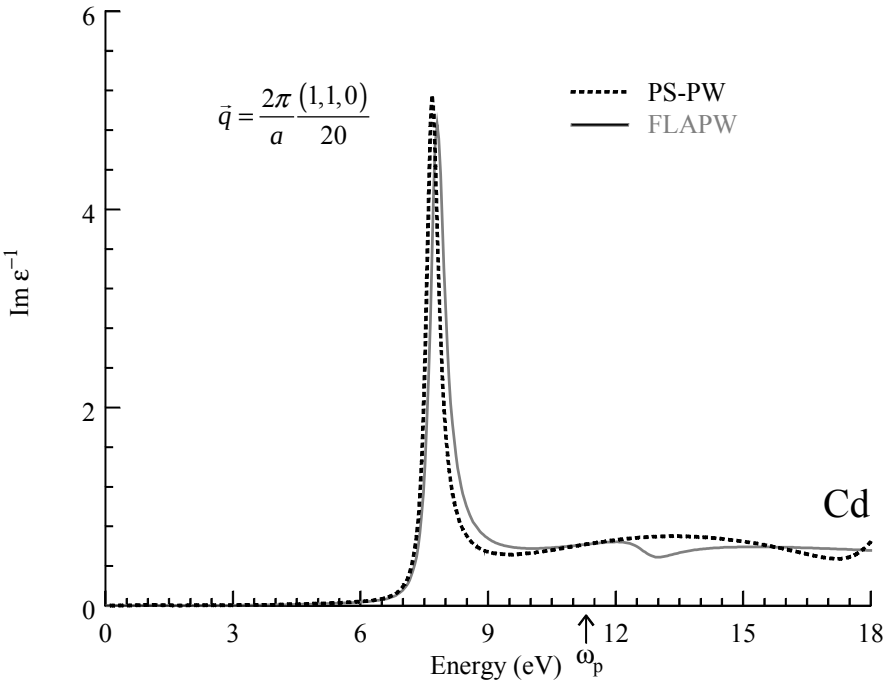

Figure 19 TDLDA loss function of Cd for $\vec{q} = 2\pi(1,1,0)/20a$. All-electron results (solid line) are contrasted with ab initio pseudopotential results (dashed line). For reference, the nominal plasmon frequency is also denoted.

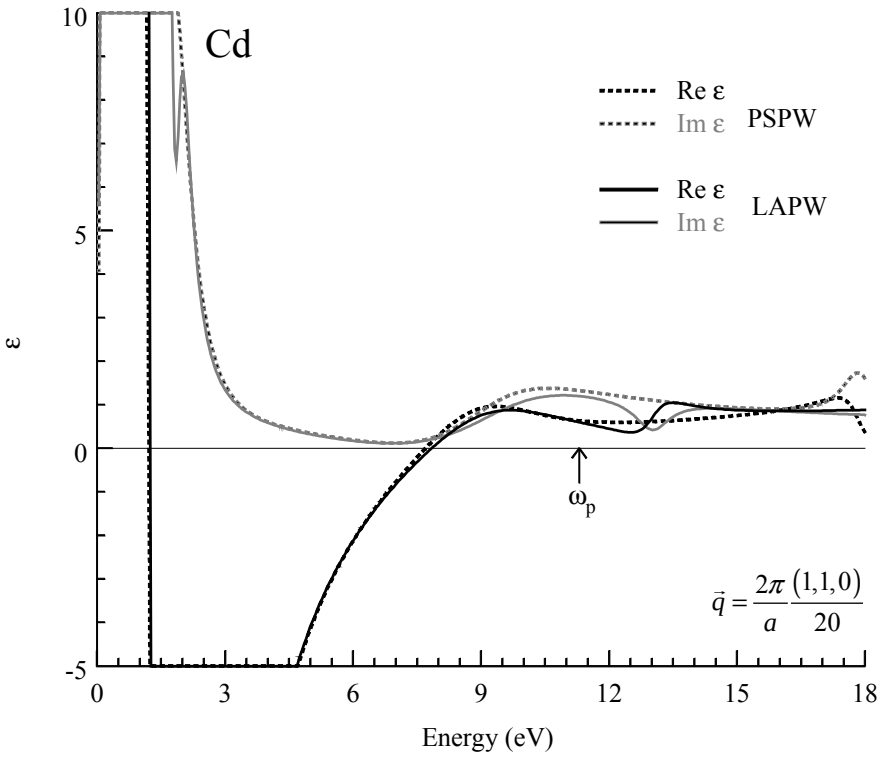

Figure 20 TDLDA dielectric function of Cd for $\vec{q} = 2\pi(1,1,0)/20a$. The all-electron results are denoted with solid lines for the $\mathrm{Re}\,\varepsilon$ (solid black line) and imaginary $\mathrm{Im}\,\varepsilon$ (solid gray line) while the pseudopotential results are denoted with dashed lines with the same color convention. For reference is shown the nominal plasmon frequency for the *sp*-electrons.

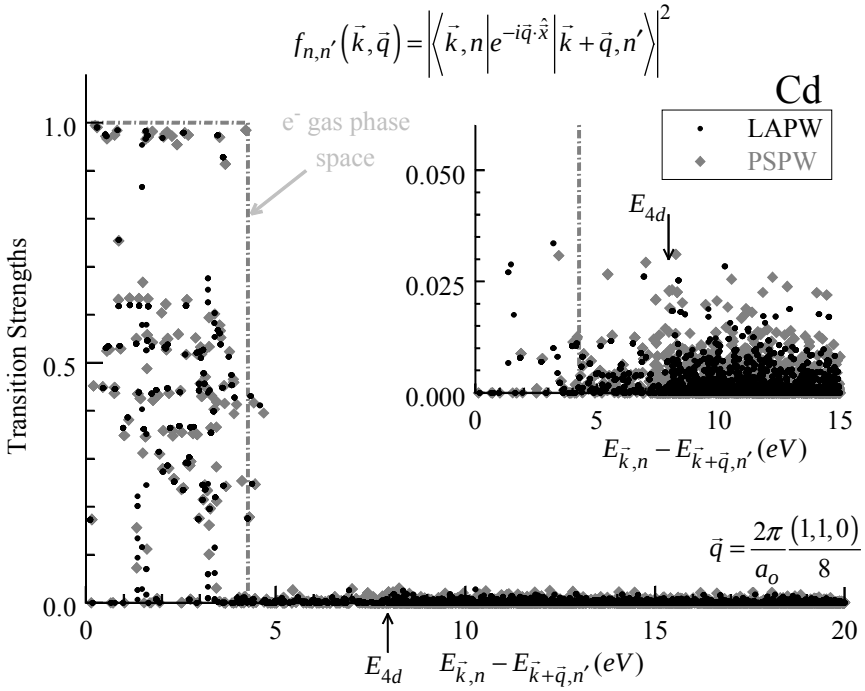

Figure 21 Comparison of the transition strengths for Cd with the all-electron (small black circles) and pseudopotential (full gray circles) methods, plotted versus the corresponding Kohn-Sham excitation energies. All results are obtained in the LDA. For reference, the corresponding results for the non-interacting electron gas (dashed line) is shown, as well as the binding energy of the 4*d*-electrons as obtained in the LDA. The inset shows the same on a reduced horizontal and vertical scale to emphasize the region near the 4*d* threshold energy.

We also make the following observation. In the electron gas region, the transition strengths appear to be consistent with the existence of two types of final states, one of an *s*-like nature giving rise to transition strengths near unity and *p*-like final states which give transition strengths in the range of 0.2 to 0.6. This should be contrasted with the results for Ag (Figure 17) which are essentially featureless in the electron gas region. Note that this is consistent with the nominal valence electronic structure of Ag, which is $4d^{10}5s^{1}$, for we then expect nearly free-electron-like contributions arising from transitions between the *s*-like states at the Fermi surface. We move next to discuss the case of Zn.

Zn

For the case of Zn we adopt the $X\alpha$ [58,85] approximation for the treatment of exchange and correlation. The reason for doing so is obvious with reference to the TDLDA loss function, which disagrees qualitatively with the experimental spectra [45,46]; we view this discrepancy as a signature of the spurious self-interactions contained in the LDA. Thus, we perform self-consistent ground state calculations within the $X\alpha$ approach with a value of α [45,46] optimized such that the loss function emulates experiment; this optimal value turns out to be 0.9 for Zn [45,46].

Consider the $X\alpha$ band structure of Zn as shown in Figure 22 for the optical value of α obtained in the two methods. Note the close agreement for all wave vectors in the

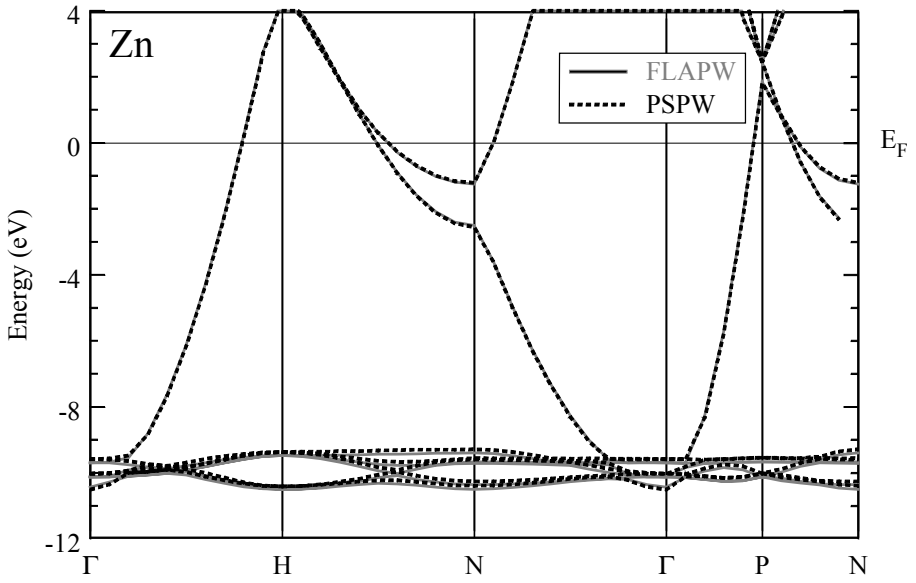

Figure 22 Band structure of bcc Zn in Slater's $X\alpha$ approximation for $\alpha = 0.9$. All-electron results (solid line) are contrasted with *ab initio* pseudopotential results (dashed line).

BZ and for both occupied and unoccupied KS levels; in fact, the agreement between the two methods is even better than the 200 *meV* differences that we find in Ag and Cd.

In Figure 23 we compare the loss functions from the pseudopotential and all-electron band structures and wave functions. Note the striking disagreement between the two spectra; both methods predict a sharp onset starting at ~8.8 *eV*, however the pseudopotential-based loss function is much more intense than the all-electron loss. For energies above this onset, the spectra are also quite different. The all-electron result clearly has a second loss feature at ~13.4 *eV* while the pseudopotential result has only a mild shoulder in this same energy range. Recent EELS measurements by Fink found an anomalous dispersion of the plasmon energy in Zn as well as a strong wave vector dependence of the oscillator strengths [6]. It would digress too much here for our purposes to discuss at length how the first principles results differ in interpretation compared to that of Ref. [6]. Instead, we briefly discuss the physical nature of this second loss feature at ~13.4 *eV* in Figure 23.

In Figure 24 we show the dielectric function of Zn for $\vec{q} = 2\pi(1,1,0)/20a$. Both the all-electron and pseudopotential values are shown, as well as results obtained by "freezing" the *d*'s out of polarization processes as discussed beloew. Note the marked disagreement in $\mathrm{Im}\,\varepsilon$ from the two methods, especially for energies at and beyond the threshold for *d*-electron excitation. Concomitant with this is a very different description

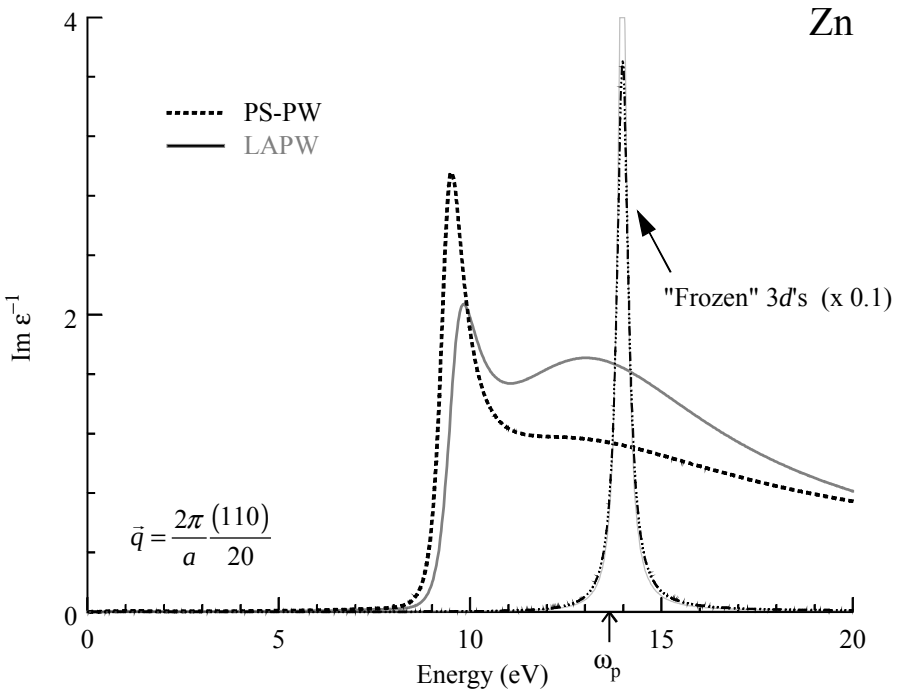

Figure 23 Loss function of Zn in the $X\alpha$ approximation for $\vec{q} = 2\pi(1,1,0)/20a$. The all-electron result is given by the solid line, while the pseudopotential result is the dashed line. For reference is also shown the nominal plasmon frequency for the *sp*-electrons. Calculations in which the 3*d* electrons are "frozen" out of polarization processes (see text) are also shown, using thin a solid line for the all-electron result and dashed line for the *ab initio* pseudopotential result.

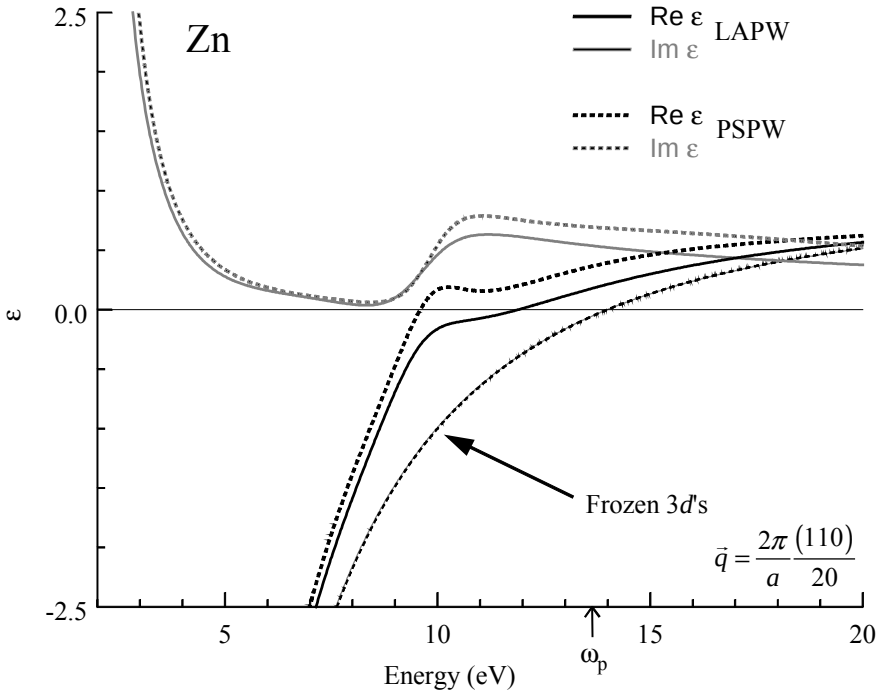

Figure 24 Dielectric function of Zn as obtained in the $X\alpha$ approximation for $\vec{q} = 2\pi(1,1,0)/20a$. The all-electron results are given by the black and gray lines for the real ($\mathrm{Re}\,\varepsilon$) and imaginary ($\mathrm{Im}\,\varepsilon$) parts of the dielectric function, respectively, while the pseudopotential results are shown using dashed lines and the same color convention. For reference is also denoted the nominal plasmon frequency for the *sp*-electrons of Zn. As well, we denote $\mathrm{Re}\,\varepsilon$ by dashed lines for calculations in which the 3*d* electrons are "frozen" (see text).

of $\mathrm{Re}\,\varepsilon$. Clearly, the all-electron result suggests a natural frequency around 12 *eV* corresponding to plasma oscillation of the *sp* electrons. The pseudopotential result, however, has only a single natural frequency at much lower energy and associated with the excitation of the *d* electrons. This is the dominant reason the two loss spectra are so different.

The two light curves labeled as "frozen 3*d*'s" in Figure 23 and Figure 24 correspond to evaluations of the loss functions which exclude the 3*d* levels from polarization processes; they are "frozen" in place. This simply means that when constructing the KS response function, the 3*d* bands are excluded from the sum over bands (see Eq. (20)). These results exhibit free-electron-like behavior, are in very good agreement with one another, and provide further evidence that the main problem in the pseudopotential approach is the predicted screening (and damping) properties of the 3*d*'s.

These dramatic differences in the dielectric function and loss functions for Zn are most clearly understood with reference to the transition strengths. In Figure 25 we compare the transition strengths from the all-electron (small black circles) and pseudopotential (full gray circles) band structures and wave functions for $\vec{q} = 2\pi(1,1,0)/8a$. The inset emphasizes the region near the binding energy of the 3*d*'s. For low energies the two results are quite similar; however, for energies in the neighborhood of the 3*d* threshold, the transition strengths of the pseudopotential approach

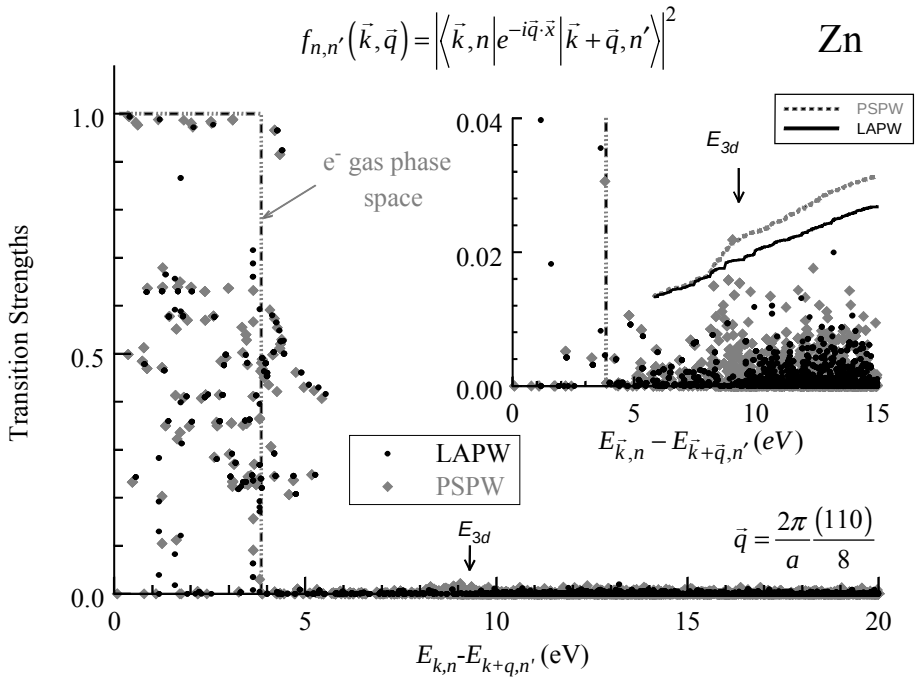

Figure 25 Comparison of the transition strengths (see text) of Zn obtained with the all-electron (small black circles) and pseudopotential (full gray circles) methods versus the corresponding Kohn-Sham excitation energies. For reference, the corresponding results for the non-interacting electron gas (dashed line) are shown, as well as the binding energy of the 3*d*-electrons as obtained in the LDA. Inset. Same quantities but on an reduced horizontal and vertical scale.

are much too large compared to the all-electron results. As a guide to the eye, we also denote the cumulative spectral weight of both the all-electron and pseudopotential transition strengths with

$$I(E) \equiv \int_{E_{3d}-\delta_1}^{E} dE' \sum_{\vec{k},j,j'} \delta\left(E' - \left(E_{\vec{k},j} - E_{\vec{k}+\vec{q},j'}\right)\right) f_{j,j'}\left(\vec{k} \mid \vec{q}\right),$$

where E_{3d} is the (minimum) binding energy of the 3*d*'s (~9.8 *eV*) and δ_1 is a numerical parameter chosen to emphasize the region near the 3*d* binding energy. We take $\delta_1 = 4\,\text{eV}$ and, for the purposes of presentation, displace the curves vertically in the inset. This cumulative weight clearly shows that for energies well below the binding energy of the 3*d*'s the transition strengths are of similar weight

$$I_{LAPW}(E) = I_{PSPW}(E), \quad E_{3d} - \delta_1 \le E \le E_{3d} - \delta_2$$

with $\delta_2 \simeq 1.6\,eV$. However, for higher energies we have

$$I_{LAPW}(E) \le I_{PSPW}(E), \quad E_{3d} - \delta_2 \le E\,;$$

in particular, near the 3*d* binding energy the all-electron spectral weight is only 60% of the pseudopotential-based results and the latter continue to gain spectral weight relative to the former for higher energies. Of curious nature is the non-zero value of δ_2, suggesting that the *sp*-like states just above the 3*d* levels are also poorly described in the

pseudopotential approach. Returning to the transition strengths of Cd as in Figure 21 we find the same trend although it is not nearly as pronounced as in Zn.

It seems fitting here to clarify the microscopic reason that the loss spectra of Zn and Cd are so distinct even though they are essentially isoelectronic. In Cd the oscillator strengths of the $4d \rightarrow 5p$ transitions are much larger than the corresponding $3d \rightarrow 4p$ transitions of Zn (see for example, $\mathrm{Im}\,\varepsilon$ in Figure 20 and Figure 24). This gives rise to a larger density of decay channels and to significant screening at intermediate energies (5 - 30 *eV*). Cd then has no nominal plasma oscillation and has a only single resonant loss feature associated with a natural frequency of the 4*d*'s and consistent with experiment [7]; moreover, the spectral weight of the *sp*-plasmon is distributed over a large range of incoherent loss features. In Zn on the other hand, the screening provided by the 3*d* electrons is incomplete, and such the nominal plasma oscillation still manifests itself in the loss spectra although it is significantly broadened.

Conclusions for Section II

It is suggestive to note that the strength of the non-local component of the pseudopotential in the ground state calculations shows the same trends as the disagreement we find in the transition strengths and loss functions for the three materials presented. As a measure of the strength of the non-local pseudopotential, note that the ratio of the non-local pseudopotential energy to the total energy is 0.96, 1.06 and 1.20 for

Ag, Cd, and Zn respectively. Thus, Zn has the strongest non-local potential, while Ag and Cd are of similar strength.

Of relevance to the same is that the first frequency moment sum rule for the pseudopotential and all-electron results is different. We recall that with the Hamiltonian as defined in Eq. (1), but with a time-independent external potential, one derives the following first frequency moment sum rule for the dynamical density response function of Eq. (12)

$$\int_{-\infty}^{+\infty} d\omega\, \omega\, \mathrm{Im}\, \chi_{\vec{G},\vec{G}'}(\vec{q},\omega) = -\left(\vec{q}+\vec{G}\right)\cdot\left(\vec{q}+\vec{G}'\right)\frac{\omega_p^2}{16}\frac{n_{\vec{G}'-\vec{G}}}{n_{\vec{0}}}. \tag{32}$$

In Eq. (32) $n_{\vec{G}}$ is the Fourier coefficient of the charge density

$$n_{\vec{G}} = \frac{1}{\sqrt{\Omega}}\int_{\Omega} d^3x e^{-i\vec{G}\cdot\vec{x}} n(\vec{x}). \tag{33}$$

One may apply similar arguments as used in deriving Eq. (34) to the KS Hamiltonian (for a definition of the KS Hamiltonian see Appendix H), to obtain

$$\int_{-\infty}^{+\infty} d\omega\omega\, \mathrm{Im}\, \chi_{S,\vec{G},\vec{G}'}(\vec{q},\omega) = -\left(\vec{q}+\vec{G}\right)\cdot\left(\vec{q}+\vec{G}'\right)\frac{\omega_p^2}{16}\frac{n_{\vec{G}'-\vec{G}}}{n_{\vec{0}}}. \tag{34}$$

We note that the right-hand sides of Eqs. (32) and (34) are the same as a consequence of the non-interacting v-representability of the electron charge density [83]. We do stress

however that Eqs. (32) and (34) are obtained on the basis of a local external potential; for non-local external potentials, such as in the pseudopotential approach, the right-hand side of the f-sum rule contains corrections proportional to matrix elements of the non-local potential. We also note that in the long wavelength limit it is well known that pseudopotential-based transition strengths include a contribution that is absent in the all-electron approach [95]. Consider the transition strength, $f_{vc}\left(\vec{k}\,|\,\vec{q}\right)$, for a valence state $\left(\vec{k},v\right)$ and conduction state $\left(\vec{k}+\vec{q},c\right)$. In the limit of vanishing wave vector, $\vec{q}\to\vec{0}$, we have [95]

$$f_{v,c}\left(\vec{k}\,|\,\vec{q}\right)\to\frac{\vec{q}}{\left(E_{\vec{k},c}-E_{\vec{k},v}\right)}\cdot\left[2\left\langle\vec{k},v\left|\hat{\vec{p}}\right|\vec{k},c\right\rangle - i\left\langle\vec{k},v\left|\left[\hat{\vec{x}},\hat{V}_{NL}\right]_{-}\right|\vec{k},c\right\rangle\right] \quad . \tag{35}$$

On the right-hand side of this equation $\hat{\vec{p}}$ is the momentum operator, and $\hat{V}_{NL}$ is the non-local component of the pseudopotential. Of course, in the all-electron case, this second term is non-existent. It turns out that in most simple systems the non-local component of the pseudopotential contributes only minor corrections to the left-hand side of Eq. (35) [95]; this suggests that the first term in Eq. (35) is similar for these same systems, consistent with our findings for the transition strengths of simple materials which are only weakly wave vector independent for small wave vectors. The present work however,

clearly reveals that away from the optical limit of Eq. (35) there are differences in the two methods.

All of these discrepancies are in spite of an almost perfect quantitative agreement of the band structures from the two methods. It is unclear whether formal refinements in the *ab initio* pseudopotential theory or density functional theory will be able to surmount this fundamental ambiguity. Furthermore, it calls in to question the results of a variety of calculations based on pseudopotential matrix elements, including response and quasiparticle lifetime calculations [17,89,90,91] as wells as the optimized potential method [96,97,125-127]. A quantitative assessment of these methods, implemented in the pseudopotential approach, is underway and will be reported in a future publication [47].

SUMMARY FOR CHAPTER ONE

As well as providing a benchmark for future theoretical treatments, the present work reveals the need for further experimental studies. With third generation synchrotron sources that are now coming online, as well as advanced methods for the preparations of single crystal samples, one should be able to probe in greater detail the line shape and line widths of the loss features, serving to corroborate or refute the present findings. For Ag this would benefit the present understanding of the anomalous dispersion of the nominal

plasmon line width, while for Ni it would serve to resolve whether the low energy collective excitation observed in Pd is also universal to Ni.

Clearly one cannot expect to explain all the complex excitations of the many-body system based on only RPA-like physics via the KS response function and the exchange-correlation potential. Given the remarkable line shapes observed in the 3*d* and 4*d* metals and the non-trivial assumption regarding the role of v_{xc}, we have a clear and urgent need to investigate the dynamical processes contained in the exchange-correlation kernel $f_{xc}(E)$. A definitive treatment of both the band dispersions and dynamical interactions will help shed light on the remaining difference with experiment. A formalism for carrying out such an investigation is provided in the time dependent optimized potential method (TDOPM) [96,97], whereby one obtains the exchange-correlation potential and corresponding exchange-correlation kernel in a rigorous manner. The underpinnings of just such an approach are outlined in Chapter Two . In Chapter Two we evaluate the exchange-only potential of the optimized potential method [86,97] for the electronic structure of Si with future studies to be carried out in the direction of $f_{xc}(\omega)$.

Chapter Two: Exact Exchange

INTRODUCTION

Although we adopted the intuitive viewpoint in the first Section of Chapter One that the loss spectra in select 3*d* and 4*d* metals maps specific features of the KS band structure, clearly we cannot expect to be able to account for all the complicated many-body processes probed in inelastic scattering experiments with exchange-correlation potentials of increasing sophistication. Of need then is the construction of a non-trivial (non-local and frequency dependent) exchange-correlation kernels from a *ab intio* exchange-correlation functionals; ultimately this may shed new light on the line shape of materials such as Ag and Zn.

Non-local theories of the exchange-correlation energy for real systems (atoms, molecules, and extended systems) are just now becoming possible with modern computational resources. The present understanding of the various asymptotic properties and scaling relationships satisfied by the exact exchange-correlation energy functional and its functional derivatives [1,29,32,33,60,124-148] has lead to the development of powerful optimized potential and hybrid methods [150,151,152]. These, in principle, exact results not-withstanding, very little in the way of actual calculations has been accomplished, except for few-electron systems [153,154]. For solids, there are only a few studies of non-local contributions to the exchange-correlation energy functional [124,142,149]. Even these yield very distinct results, including, for example, a large

range of reported values for the absolute band gap of Si, ranging from 0.8 [127] to 1.5 [92].

Pursuant to the goal of an *ab initio* treatment of the exchange-correlation potential and kernel as discussed in Chapter one, and for its obvious technological importance, we investigate the band structure of Si through the solution of the optimized potential equations in the exchange-only approximation. The results are encouraging. Out results show consistent trends with Refs. [92,93] and even better still with optimized potential results reported in Ref. [94,125-127]. However, the numerical discrepancies with the results of Refs. [92,93] is alarming, being well outside the numerical error of the method itself.

THEORETICAL ESSENTIALS

Much of the underlying theoretical framework for the present Chapter is discussed in Appendix H; in that Appendix the reader will find a review of fundamental theorems of the ground state put forth by Hohenberg and Kohn [20]. For completeness of presentation here, we simply remind the reader of a few of the most crucial points. We then derive the integral equation satisfied by the exchange-only potential to be evaluated for the Si crystal in a later Section of this Chapter.

The total energy of spin spin-compensated, N -particle system, in the presence of a local external potential, can be obtained with reference to the Kohn-Sham non-interacting system [19]. In the notation of Appendix H, the total energy of the system is

$$E[n]+\int d^3x\, n(\vec{x})\,\mathrm{v}_{ext}(\vec{x}) = 2\sum_{v} E_v - U[n] - U_{xc}[n] + E_{xc}[n]. \tag{36}$$

In Eq. (36) $U[n]$ is the Hartree potential energy, $U_{xc}[n]$ the exchange-correlation potential energy functional and $E_{xc}[n]$ the exchange-correlation energy functional. The single-particle eigenvalues, E_v, correspond to the occupied Kohn-Sham states, ϕ_i, which satisfy the following Schrödinger-like equation

$$\left\{-\frac{1}{2}\vec{\nabla}^2 + \mathrm{v}_{ext}(\vec{x}) + v_H[n](\vec{x}) + v_{xc}(\vec{x})\right\}\phi_i(\vec{x}) = E_i\phi_i(\vec{x}), \tag{37}$$

and contribute to the electron charge density

$$n(\vec{x}) = 2\sum_{v}\left|\phi_v(\vec{x})\right|^2. \tag{38}$$

In Eq. (37) $v_H[n](\vec{x})$ is the Hartree potential and v_{xc} is the exchange-correlation potential, given by the first variational coefficient of the exchange-correlation energy

$$v_{xc}(\vec{x}) = \frac{\delta E_{xc}[n]}{\delta n(\vec{x})}, \tag{39}$$

and whose purpose is to represent all the complexity of the correlated ground state. The self-consistent solution of equations (36)-(39) constitute the Kohn-Sham method [19]. Before providing a derivation of the integral equation for the exchange-correlation potential, we digress briefly on the self-interaction problem, noting its relevance for the exchange-only method to be implemented later in this Chapter.

The Self-Interaction

We return to discuss the concept of the self-interaction as introduced in Chapter One. We begin first by reviewing the concept for the Hartree-Fock approximation as it is more easily examined than in the Kohn-Sham system. The HF equations for occupied state, v, take the form

$$\left\{-\frac{1}{2}\vec{\nabla}^2+\mathrm{v}_{ext}\left(\vec{x}\right)+v_H\left[n\right]\left(\vec{x}\right)\right\}\varphi_v\left(\vec{x}\right)+\int d^3x'v_F\left(\vec{x},\vec{x}'\right)\varphi_v\left(\vec{x}'\right) = \mathrm{E}_v\varphi_v\left(\vec{x}'\right), \tag{40}$$

where the Fock potential, $v_F\left(\vec{x},\vec{x}'\right)$ accounts for exchange effects

$$v_F\left(\vec{x},\vec{x}'\right)=-v\left(\vec{x}-\vec{x}'\right)\sum_{v'}\varphi_{v'}\left(\vec{x}\right)\varphi_{v'}^{*}\left(\vec{x}'\right). \tag{41}$$

The summation in Eq. (41) is over the occupied HF states and the Hartree potential

$$v_H\left[n\right]\left(\vec{x}\right)=\int d^3x'v\left(\vec{x}-\vec{x}'\right)n\left(\vec{x}'\right),$$

includes the mean field from all the occupied orbital densities,

$$\mathrm{n}_{v'}(\vec{x}) \equiv \left|\varphi_{v'}(\vec{x})\right|^2, \tag{42}$$

in particular, the term $v = v'$. We separate this self-contribution, to write Eq. (40) as

$$\left\{-\frac{1}{2}\vec{\nabla}^2 + \mathrm{v}_{ext}(\vec{x}) + \sum_{v' \neq v} v_H\left[\mathrm{n}_{v'}\right](\vec{x})\right\}\varphi_v(\vec{x}) + v_H\left[\mathrm{n}_v\right](\vec{x})\varphi_v(\vec{x}) + \int d^3x' v_F(\vec{x},\vec{x}')\varphi_v(\vec{x}') = \mathrm{E}_v\varphi_v(\vec{x}') \tag{43}$$

The physical nature of third term in Eq. (43) is spurious, for it allows a given electronic state, φ_i to see its own bare field directly. However, an equal and opposite contribution is contained in the Fock potential, to obtain

$$\left\{-\frac{1}{2}\vec{\nabla}^2 + \mathrm{v}_{ext}(\vec{x}) + \sum_{v' \neq v} v_H\left[\mathrm{n}_{v'}\right](\vec{x})\right\}\varphi_v(\vec{x}) - \int d^3x' v(\vec{x}-\vec{x}')\varphi_v(\vec{x}')\sum_{v' \neq v}\varphi_{v'}(\vec{x})\varphi^*_{v'}(\vec{x}') = \mathrm{E}_v\varphi_v(\vec{x}'). \tag{44}$$

The form of Eq. (44) demonstrates that the effective potential seen by any given electronic state consists of contributions from all the other valence orbitals.

This exact cancellation of the self-Hartree field by the self-exchange field ensures that, for a finite system, an electron removed to infinity sees the proper Coulomb field of the system it leaves behind. Consider a finite system, (e.g. an atom); for simplicity, we

also limit ourselves to systems with spherical symmetry, for which the large r expansion of the Hartree potential acting on the v^{th} occupied state yields

$$v_H(\vec{x})\varphi_v(\vec{x}) \underset{|\vec{x}|\to\infty}{} \frac{N}{|\vec{x}|}\varphi_v(\vec{x}). \tag{45}$$

One can do the same for the exchange interaction to obtain

$$\int d^3x' v_F(\vec{x}-\vec{x}')\varphi_v(\vec{x}') \underset{|\vec{x}|\to\infty}{} -\frac{1}{|\vec{x}|}\varphi_v(\vec{x}), \tag{46}$$

so that at large distances the total electronic field [123] acting on the v^{th} electron would go as

$$\frac{N-1}{|\vec{x}|},$$

just as we expect on physical grounds. A given electron should see the system of $N-1$ electrons it "leaves behind" or equivalently, it sees the mean field and its own exchange-hole that it leaves behind "embedded" in the total charge density. For the energetics of the HF system, we note that the self-exchange-energy of a occupied state is

$$E_X^{HF}[\mathrm{n}_v] = -\frac{1}{2}\int d^3x\, d^3x'\, \mathrm{n}_v(\vec{x})\, v(\vec{x}-\vec{x}')\, \mathrm{n}_v(\vec{x}), \tag{47}$$

and exactly cancels the self-Hartree energy

$$U[\mathrm{n}_v] = \frac{1}{2}\int d^3x d^3x' \,\mathrm{n}_v(\vec{x})\, v(\vec{x}-\vec{x}')\,\mathrm{n}_v(\vec{x}')\,. \tag{48}$$

Thus, for all the occupied HF states we have

$$E_X^{HF}[\mathrm{n}_v] + U[\mathrm{n}_v] = 0\,. \tag{49}$$

Perdew and Zunger [60] demonstrated that the exact exchange-correlation energy functional is self-interaction-free in the sense that the self-exchange-correlation energy and self-Hartree energies exactly cancel for all the KS valence states

$$E_{XC}[n_v] + U[n_v] = 0\,. \tag{50}$$

In Eq. (50), $n_v(\vec{x})$ is just the KS valence state density, $|\phi_v(\vec{x})|^2$ and E_{XC} is the exchange-correlation energy functional. The exchange energy functional of DFT as discussed below, satisfies Eq. (50) explicitly, even for *approximate* orbitals (as in the LDA for example), so that the following constraint [60] on the exact correlation energy functional obtains

$$E_C[n_v] = 0\,, \tag{51}$$

for any approximate description of the orbital density, n_v, inserted into the *exact* functional E_C. Ambladh and von Barth [128] demonstrated that for the highest valence state of a finite system, ϕ_h, the exchange-correlation potential takes asymptotic form

$$v_{XC}[n](\vec{x})\phi_h(\vec{x}) \underset{|\vec{x}|\to\infty}{\longrightarrow} -\frac{1}{|\vec{x}|}\phi_h(\vec{x}), \tag{52}$$

which is of same as that of Eq. (46) if one thinks of replacing the HF system by the KS system taking v_{XC} to be the best local approximation to the non-local Fock interaction at the Fermi surface. In fact, one may demonstrate that the exchange potential, v_X, satisfies Eq. (52) exactly because the exchange (Fermi) hole contains exactly –1 unit of charge. Thus by Eq. (52), the correlation potential must fall off faster than $1/r$ for large r.

Construction of local potential satisfying Eq. (52) and with corresponding exchange-correlation energy functional that satisfies Eq. (50) is highly nontrivial; only recently has even the exchange-only approach been applied to solid systems [124-127], at best using an LDA or GGA description (neither of which satisfies Eq. (51)) of correlation. Previous studies concentrated systems of high symmetry where the integral equation can be reduced to one dimension. This is the same as the optimized effective potential (OEP) method of Talman and Chadwick [86].

The Exchange-Correlation Potential

The exchange-correlation energy can be separated into exchange and correlation contributions in a variety of equally valid fashions [129,130,140,141,153,]. The most common choice for the exchange energy is

$$E_X[n] = \left\langle \hat{V} \right\rangle_S - U[n], \tag{53}$$

which is of the form of the traditional Hartree-Fock energy evaluated for the Kohn-Sham system

$$E_x[n] = -\frac{1}{2}\sum_{\nu,\nu'} \int d^3x\, d^3x'\, \phi_\nu^*(\vec{x})\,\phi_{\nu'}^*(\vec{x}')\, v(\vec{x}-\vec{x}')\,\phi_{\nu'}(\vec{x})\,\phi_\nu(\vec{x}')\,. \tag{54}$$

The corresponding correlation energy is given by the difference between the expectation value of the intrinsic electron Hamiltonian taken in the many-body and Kohn-Sham ground states

$$E_C[n] = \left\langle \hat{T} + \hat{V} \right\rangle - \left\langle \hat{T} + \hat{V} \right\rangle_S, \tag{55}$$

which consists of a kinetic and exchange-like contribution.

Note that, although we have an explicit expression for E_X, as in Eq. (54), and, although we can evaluate the corresponding exchange potential exactly (as we do in Section II of this Chapter), we do not have explicit the functional dependence, $v_X[n](\vec{x})$ or $E_X[n]$. As such, the integral equation for the exchange potential is rather complicated, which explains the lack of any major *ab initio* thrust in this direction except for those few studies already referenced.

Since the KS orbitals are functionals of the density, and since we have explicit the functional dependence of the exchange energy on the KS orbitals, we affect the chain rule to for functional differentiation to obtain

$$\frac{\delta E_X}{\delta n(\vec{x})} = \sum_v \int d^3x' \left\{ \frac{\delta E_X}{\delta \phi_v(\vec{x}')} \frac{\delta \phi_v(\vec{x}')}{\delta n(\vec{x})} + \frac{\delta E_X}{\delta \phi_v^*(\vec{x}')} \frac{\delta \phi_v^*(\vec{x}')}{\delta n(\vec{x})} \right\}. \tag{56}$$

We may apply the chain rule once more, for the KS orbitals are also functionals of the KS potential, which is itself a functional of the density

$$\frac{\delta \phi_v(\vec{x})}{\delta n(\vec{x}')} = \int d^3x'' \frac{\delta \phi_v(\vec{x})}{\delta v_S(\vec{x}'')} \frac{\delta v_S(\vec{x}'')}{\delta n(\vec{x}')}. \tag{57}$$

The functional derivatives occurring in the integrand of Eq. (57) are easily carried out. $\delta v_S / \delta n$, is simply the static inverse Kohn-Sham susceptibility, χ_S^{-1}; note that in our construction we have excluded constant changes from the space of allowable potentials and charge densities so that the inverse KS response exists (see Appendices C and H) . The functional derivative, $\delta \phi_i / \delta v_S$, can be obtained from first order perturbation theory as

$$\frac{\delta \phi_v(\vec{x})}{\delta v_S(\vec{x}')} = \phi_v(\vec{x}') \sum_{j \neq i} \frac{\phi_j(\vec{x}) \phi_j^*(\vec{x}')}{E_i - E_j}. \tag{58}$$

The right-hand side of Eq. (56) is then

$$v_X[n](\vec{x}) = \sum_{v,c} \int d^3x' dx'' \left[\frac{\phi_v^*(\vec{x}') u_{X,v}(\vec{x}') \phi_c(\vec{x}')}{E_v - E_c} \phi_c^*(\vec{x}'') \phi_v(\vec{x}'') + \text{c.c.} \right] \chi_S^{-1}(\vec{x}'', \vec{x}) \quad , \tag{59}$$

where c.c. denotes complex conjugation and the orbital dependent "potential", $u_{X,v}$, is defined by

$$u_{X,v}(\vec{x}) = \frac{1}{\phi_v^*(\vec{x})} \frac{\delta E_X[n]}{\delta \phi_v(\vec{x})} . \tag{60}$$

In Eqs. (59) and (60) v and c refer to occupied and unoccupied KS states. Note that only "off-diagonal" terms occur in Eq. (59), i.e. there are no matrix elements of $u_{X,v}$ between two occupied states; these terms, which are initially present due to the summation over states in Eq. (58), cancel out in the final expression because of the c.c. terms in Eq. (56). The correlation potential satisfies a similar equation, with $u_{X,v}$ and E_X replaced by $u_{C,v}$ and E_C, but also with the consideration that the KS conduction states may explicitly enter a description of the correlation energy functional.

For the exchange-only case, one may evaluate the orbital-dependent potentials, $u_{X,v}$ explicitly. The matrix elements $\langle v | \hat{u}_{X,v} | c \rangle$ are easily evaluated to be

$$\langle v | \hat{u}_{X,v} | c \rangle = \langle v | \hat{v}_{HF}^{KS} | c \rangle . \tag{61}$$

At this point, we adopt a notation more appropriate for a solid system using Bloch indices. We can then write Eq. (59) as

$$v_X\left(\vec{x}\right)=\sum_{\vec{k},v,c}\frac{\left\langle \vec{k},v\left|\hat{v}_{HF}\right|\vec{k},c\right\rangle}{E_{\vec{k},v}-E_{\vec{k},c}}\int d^3x'\,\chi_S^{-1}\left(\vec{x},\vec{x}'\right)\phi_{\vec{k},c}^{*}\left(\vec{x}'\right)\phi_{\vec{k},v}\left(\vec{x}'\right)+\text{c.c.}. \tag{62}$$

with KS occupied and unoccupied Bloch states, $\left(\vec{k},v\right)$ and $\left(\vec{k},c\right)$ respectively. Rather than solve Eq. (62) directly, i.e. for $v_x\left(\vec{x}\right)$, we instead work with a complete basis of functions. For which, Eq. (62) becomes a matrix equation for the coefficients of the exchange potential projected on the basis.

For the solid system, an appropriate choice of basis is the restricted momentum basis [157] (see Appendices C and H). In this representation, Eq. (62), is a matrix equation for the Fourier coefficients of the exchange potential

$$v_X\left(\vec{G}\right)=\frac{1}{\sqrt{\Omega}}\int d^3x\,e^{-i\vec{G}\cdot\vec{x}}v_X\left(\vec{x}\right), \tag{63}$$

of the form

$$v_X\left(\vec{G}\right)=\sum_{\vec{G}'\neq\vec{0}}\left\{n_X\left(\vec{G}\right)+n_X^{*}\left(-\vec{G}\right)\right\}\left(\chi_S^{-1}\right)_{\vec{G}',\vec{G}}. \tag{64}$$

In Eq. (64), we have introduced the notation, $n_X\left(\vec{G}\right)$, to stand for the charge density modulations

$$n_X\left(\vec{G}\right)=\frac{1}{\sqrt{\Omega}}\sum_{\vec{k},v,c}\frac{\left\langle \vec{k},v\left|\hat{v}_{HF}^{KS}\right|\vec{k},c\right\rangle}{E_{\vec{k},v}-E_{\vec{k},c}}\left\langle \vec{k},c\left|e^{-i\vec{G}\cdot\hat{\vec{x}}}\right|\vec{k},v\right\rangle . \tag{65}$$

In comparison to Eq. (17) of Refs. [92,93] we note the different prefactor ($1/\sqrt{\Omega}$ vs. $1/\Omega$) of Eq. (65), consistent with out different convention for the normalization of the Fourier coefficient of the exchange-potential. Note, that the summation over reciprocal lattice vectors in Eq. (64) excludes $\vec{G}'=\vec{0}$ since we have excluded constants from the space of allowable potentials (see Appendices C and H); by the same arguments the right hand side is only valid for finite $\vec{G}$. In practice this does not present any difficulty since $v_X^0\equiv v_X\left(\vec{G}=\vec{0}\right)$ represents a constant shift of all the KS energies and thus has no physical consequences. Therefore, in all that follows we set the average value of the exchange-correlation potential equal to zero without loss of generality. There is a formal expression relating the exchange-correlation potential and the Fock potential for the highest occupied state [138]. In principle, this could be used to set the absolute normalization of the exchange potential, i.e. v_X^0, although that is not done in the present work.

For technical details, the reader is referred to the following Appendices. The treatment of the singularity of HF integrand is discussed in Appendix F. The integration of the exchange-potential algorithm with the ground state program is explained in Appendix G. For more general details, such as the use of symmetry, the wave vector

sampling of the BZ, and the evaluation of the KS response function, the reader is directed to Appendices A, B, and C.

The ground state calculations are carried out using plane wave basis functions [76] with *ab initio* norm-conserving pseudopotentials [49]; both LDA and Krieger-Li-Iafrate (KLI) [142] exchange-correlation functions are considered [159]. A 25 Ry plane wave cutoff proved to be sufficient for the quantities under investigation; the lattice constant was fixed at the experimental value of 10.26 Bohr. We only briefly refer to the various numerical parameters of the calculation, including the number of bands and reciprocal lattice vectors in the KS response function, the number of bands kept in the summation on the right-hand side of Eq. (65), and the number of iterations of the KS ground state. As this represents a preliminary exploration of the method, we save a more exhaustive discussion for a future publication [160].

THE EXCHANGE-ONLY BAND STRUCTURE OF SI

Let us consider what is known to date regarding the electronic structure of Si in density functional theory. Although there is no formal correspondence between energy differences as measured with photoemission and KS eigenvalues, they do serve as a good reference for the comparison of approximate DFT techniques. It is well known that the LDA is poor in comparison to photoemission for the band structure of Si. The minimum (absolute) band gap of Si is defined by a 3-fold degenerate band at the Γ point and a

point 80% of the way to the zone boundary along ΓX [163]. The absolute gap determined by photoemission [163] is 1.17 *eV* while that of the LDA obtained in the present study is 0.6 *eV* and is representative of those values reported in the literature [92-94]. Various schemes for improving upon the LDA results have been suggested, including a variety of KS and many-body approaches.

For convenience of discussion of the results we have need to define a few convenient notations. We will have need to refer to exchange-correlation functional in both the ground state (crystal) calculation and in the pseudopotential construction. We will use the notation A/B to refer to the results, where A and B are generic for the type of exchange correlation treatment; A refers to the crystal calculation, while B refers to the pseudopotential construction. For example, we use L/KE to represent results obtained with the LDA for the valence electrons and with the KLI [142] approximation to the exchange-only potential [160] in the pseudopotential construction, hence the notation "L" and "KE".

The eigenvalue gaps relative to the valence band maximum at the L point, Γ point, and X point as well as the point enclosed by a circle, which defines the absolute (fundamental) gap in our numerical work, are convenient for comparing the quality of the calculations among the various theories and in relation to experiment. We list eigenvalue

gaps for the present work and other theoretical approaches, as well as experiment in Table 1 [163,164].

Consider the LDA band structure of Si, shown in Figure 26. The solid lines (L/L) refer to calculations that use the local density approximation for both the solid system and the pseudopotential construction. The dispersion of the bands, especially in the critical region from Γ to X, the value of the energy gaps defined by the L, Γ, and X points, as well as the valence band width (VBW) are poor in comparison to experiment [163-165]; the present LDA results yield a VBW which is 0.5 eV narrower than experiment, consistent with the other recent studies of Si [92-94]. The numbers in parentheses for the present work are all-electron results obtained in the LDA using the FLAPW [51] method; the agreement between the two approaches is critical test for the fundamental gaps except those in the critical region of ΓX for which the pseudopotential results are 0.12 eV too large.

Also shown in Figure 26 is the band structure obtained with a KLI [142] treatment of exchange for the core electrons in constructing the pseudopotential and a LDA treatment for the valence electrons in the crystal (L/KE). The band structures are nearly identical (numerically); note that the bands have been normalized to the same chemical potential for ease of comparison of the fundamental gaps. As shown in Table 1, these

Table 1 Band gaps of Si in the present work and other DFT methods. See text for explanation of the labels.

	L	G	X	VBW	Fund.
Expt.	2.1	3.05	1.25	12.5	1.17
L/L	1.472 (1.420)	2.562 (2.53)	0.680 (0.568)	11.96 (11.97)	0.572 (0.4721)
L/KE	1.528	2.520	0.577	12.02	0.484
E/L	1.876	2.783	0.973	_	0.885
E/KE	1.931	2.771	0.894	11.84	0.817
L/L [92]	1.43	2.56	0.64	11.95	-
EL/E [92]	2.30	3.26	1.5	11.58	1.44
L/E [92]	1.49	2.53	0.49	_	_
L/L [94]	1.37	2.545	0.626	12.026	_
K/HF [125]	1.88	2.86	0.963	11.878	_
KEG/HF [126]	1.506	2.633	0.492	12.32	_

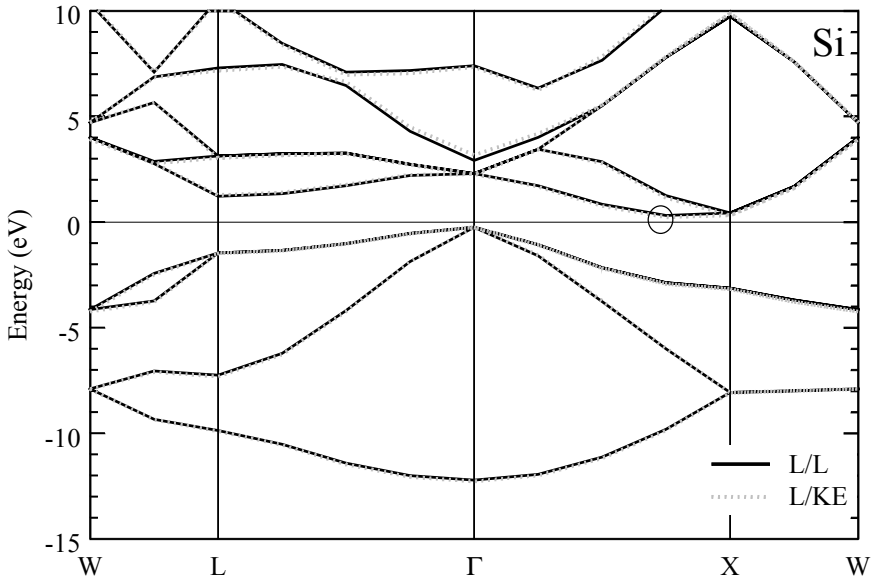

Figure 26 Band structure of Si obtained using *ab initio* pseudopotentials. The point enclosed by the circle defines the conduction band minima in our numerical results. The L/L values denoted with solid lines are obtained using the LDA for exchange and correlation in both the ground state and pseudopotential calculations.

results yield gaps are slightly worse for the direct gap at the Γ point and for the critical gap near the X point, while it obtains slight improvement for the gap at the L point. Each of these points is consistent with the trends already noted by Städele, *et al.* [92] whose results are also shown in Table 1. We next examine the impact of the exchange-only potential as implemented in the present work.

In Figure 27 we show the band structure of Si obtained using the exchange-only as outlined in the beginning of this Chapter along with the band structures in Figure 26. Figure 28 is the same on a reduced vertical scale, to emphasize the critical region near the chemical potential. Note the opening of the band gap (see also Table 1) relative to the L/L and L/KE results;. there is also a band narrowing in the exchange-only results. Both of these trends are in line with the Refs. [92-94,125-127]; however, that the present E/KE results are more consistent with the KE/KE results of Bylander and Kleinman [94,125-127]. This is somewhat surprising since the present work uses the same formalism of generating the exchange-only potential as that of Refs. [92,93].

We quote here the numerical parameters used in the evaluation of the exchange-only potential via Eqs. (62)-(64). We have tested that 200 bands proves to be sufficient for the evaluation of the KS response and in "screening" the HF matrix element in Eq. (65). For the KS response function and the exchange-only potential a plane wave cutoff

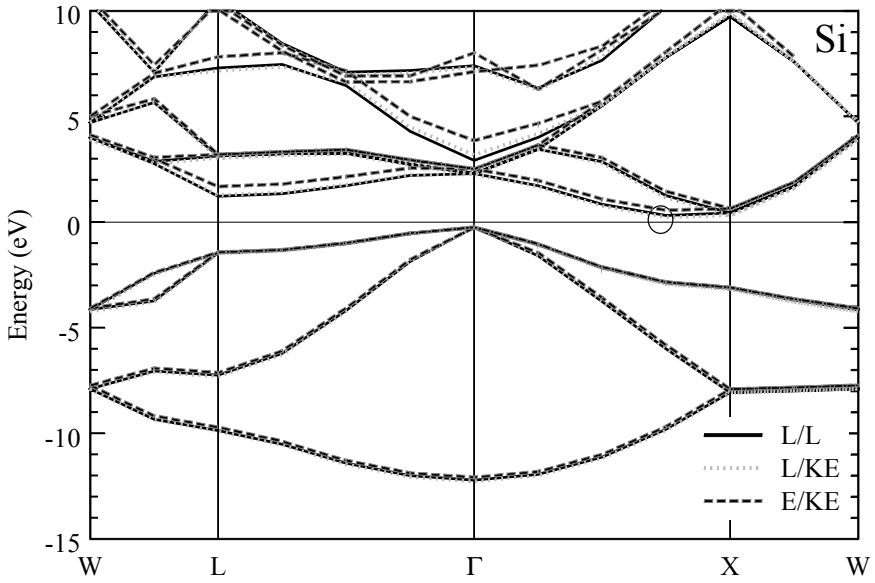

Figure 27 Pseudopotential-based band structure of Si. Exchange-only (dashed gray lines) (E/KE), L/KE and L/L results obtained in the present work.

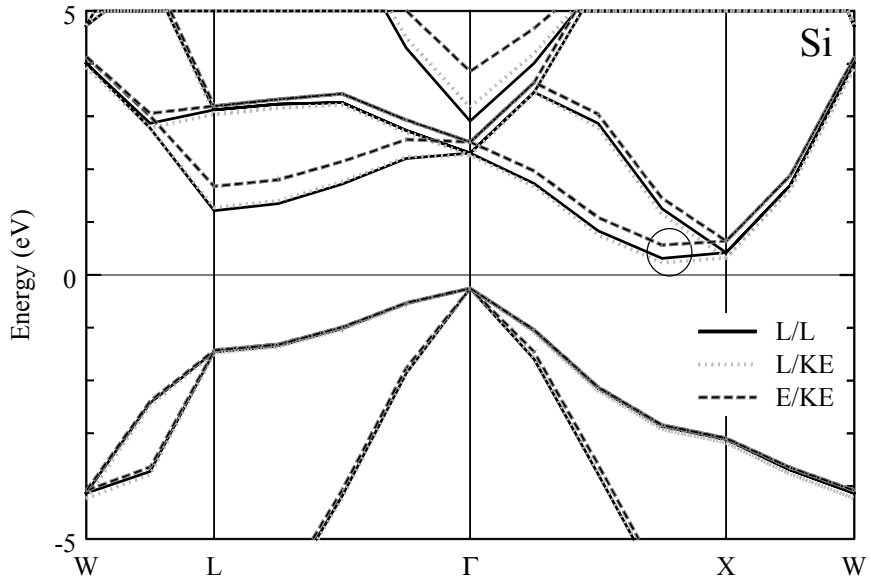

Figure 28 Pseudopotential-based band structure of Si on a reduced vertical scale to emphasize the region near the chemical potential. Exchange-only (dashed gray lines) (E/KE), L/KE and L/L results obtained in the present work.

of 8 Ry proves to be sufficient for the desired accuracy. For this parameter set we estimate the numerical errors in the KS energies to be no more than 50 *meV*.

We discuss next the physical role of the exchange potential as a function of iteration of the KS equations. As a function of iteration of the KS equations the exchange potential first closes the band gap, then overshoots the photoemission gap [163], and then approaches its asymptotic value from above. Figure 29, shows the band gap defined by the 4^{th} band at the Γ point and the point enclosed by a circle in the 5^{th} band in Figure 26 plotted as a function of the iteration of the KS equations. The line through the points is a guide to the eye. Clearly the effect exchange-only potential is highly non-trivial and is not simply a first order shift of the energies.

CONCLUSIONS

We have applied the exchange-only method to the exchange-only electronic structure of Si using *ab initio* pseudopotentials and a plane wave based approach. The resulting self-consistently obtained Kohn-Sham wave functions and charge density exhibit more localization than those of corresponding LDA based orbitals, and the fundamental band gaps move in the direction of experiment although there is no fundamental reason for this to be the case. However, the present results are in stark contrast to other recent studies. Future work will concentrate on the development of a method for obtaining the corresponding exchange-correlation kernel. This is crucial as it

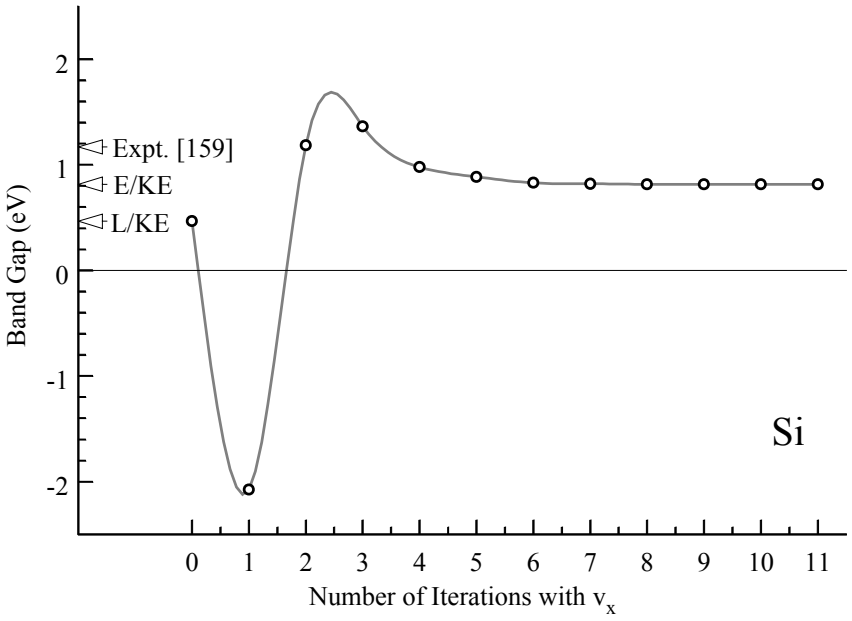

Figure 29 Band gap of Si. The gap in the present numerical work is defined by the valence band maxima at the Γ point and the wave vector for the point enclosed by a circle in Figure 26. The starting point is a self-consistent L/KE calculation and the results are plotted versus the number of iterations of the KS equations with the exchange-only potential with the line through the points as a guide to the eye.

will better address the failures of the TDLDA as we have demonstrated for Ag in Section I of Chapter One. Moreover, this highly non-trivial research goal will also serve as a benchmark for studies of correlation in the context of the optimized potential method.

References

References

1. For reviews of density-functional theory see, e.g., *Density Functional Theory of Many-Fermion Systems,* edited by S. B. Trickey (Academic, N. Y., 1990), and R. M. Dreizler and E. K. U. Gross, *Density Functional Theory: An* Approach *to the Quantum Many-Body Problem* (Springer-Verlag, Berlin, 1990). R. O. Jones and O. Gunnarsson, Rev. Mod. Phys. **61**, 689 (1989). For the rudiments of DFT see Refs. [19] and [20].

2. See for example the electronic library of Nobel Laureates: Nobel e-Museum and Refs. [3] and [4].

3. W. Kohn, Rev. Mod. Phys. **71**, 1253 (1999).

4. J. A. Pople, Rev. Mod. Phys. **71**, 1267 (1999).

5. A. vom Felde, J. Sprösser-Prou, and J. Fink, Phys. Rev. B **40**, 10181 (1989).

6. K. Widder, M. Knupfer, O. Knauff and J. Fink, Phys. Rev. B **56**, 10154 (1997).

7. M. Knupfer, K. Widder, M. Sing, O. Knauff, and J. Fink, Eur. Phys. J. B **6**, 323 (1998).

8. P. M. Platzman, E. D. Isaacs, H. Williams, P. Zschack, and G. E. Ice, Phys. Rev. B **46**, 12943 (1992), and references therein; W. Schülke, H. Schulte-Schrepping and J.

R. Schmitz, Phys. Rev B **47**, 12426 (1993); B. C. Larson, J. Z. Tischler, E. D. Isaacs, P. Zschack, A. Fleszar, and A. G. Eguiluz, Phys. Rev. Lett. **77**, 1346 (1996).

9. A. Otto and E. Petri, Solid State Communications **20**, 823 (1976).

10. T. Bornemann, J. Eickmans and A. Otto, Solid State Communications **65**, 381 (1988).

11. M. Nishijima, M. Jo, Y. Kuwahara and M. Onchi, Solid State Commun. **58**, 75 (1986).

12. D.J. Misell and A. J. Atkins, Phil. Mag. **27**, 95 (1973).

13. H. Ehrenreich and H. R. Philipp, Phys. Rev. **128**, 1622 (1962)

14. P. M. Platzman and N. Tzoar, Phys. Rev. A **139**, 410 (1965).

15. W. Plummer and W. Eberhardt in *Angle-Resolved Photoemission as a Tool for the Study of Surfaces*.

16. F. Aryasetiawan and O. Gunnarsson, Phys. Rev. B **49**, 7219 (1994); F. Aryasetiawan, O. Gunnarsson, M. Knupfer, and J. Fink, *ibid.* **50**, 7311 (1994).

17. M. A. Cazalilla, J. S. Dolado, A. Rubio, and P. M. Echenique, Phys. Rev. B **61**, 8033 (1999).

18. I. Campillo, A. Rubio and J. M. Pitarke, Phys. Rev. B **59**, 12188 (1999).

19. W. Kohn and L. J. Sham, Phys. Rev. **140**, A1133 (1965).

20. P. Hohenberg and W. Kohn, Phys. Rev. B **136**, 864 (1964).

21. A. Fleszar and W. Hanke, Phys. Rev. B **56**, 12285 (1997); H. Dröge, A. Fleszar, W. Hanke, M. Sing, M. Knupfer, J. Fink, F. Goschenhofer, C. R. Becker, R. Kargerbauer, and H. P. Steinrück, Phys. Rev. B **59**, 5544 (1999).

22. L. A. Feldkamp, M. M. Stearns and S. S. Shionozaki, Phys. Rev. B **20**, 1310 (1979).

23. Related features have been reported recently for Ag in Ref. [17] and for Pd in Ref. [24].

24. A. G. Eguiluz, A. Fleszar and J. A. Gaspar, Nucl. Inst. Meth. Phys. Res. B **96**, 550 (1995).

25. E. Runge and E.K.U. Gross, Phys. Rev. Lett. **52**, 2850 (1984).

26. R. van Leeuwen, Phys. Rev. Lett. **82**, 3863 (1999).

27. R. van Leeuwen, Phys. Rev. Lett. **76**, 3610 (1996).

28. A. Gorling, Phys. Rev. A **55**, 2630 (1997).

29. P. Hohenberg and W. Kohn, Phys. Rev. **136**, B864 (1964).

30. R. van Leeuwen, Phys. Rev. Lett. **80**, 1280 (1998).

31. E. K. U. Gross, J. F. Dobson and M. Petersilka in *Density Functional Theory of Time-Dependent Phenomena*, "Density Functional Theory", edited by R. F. Nalewajski, **181**, 81 (Springer-Verlag, Berlin 1996).

32. A. Gorling, Int. Journ. Quantum Chem. **69**, 265 (1998).

33. L. J. Sham and M. Schlüter, Phys. Rev. Lett. **51**, 1888 (1983).

34. Note however that this still does not provide the functional dependence, $v_{xc}[n](\vec{x},t)$, on the real space, real time behavior.

35. L. V. Keldysh, Sov. Phys. JETP 20, 1018 (1965). For a review of Green's function techniques for non-equilibrium situations see, for example, P. Danielewicz, Ann. Phys. **152**, 239 (1984) and/or J. Rammer, Rev. Mod. Phys. **58**, 323 (1986).

36. A. Fleszar, A. A. Quong, and A. G. Eguiluz, Phys. Rev. Lett. **74**, 590 (1995); A. Fleszar, R. Stumpf, and A. G. Eguiluz, Phys. Rev. B **55**, 2068 (1997).

37. A. A. Quong and A. G. Eguiluz, Phys. Rev. Lett. **70**, 3955 (1993).

38. N. E. Maddocks, R. W. Godby, and R. J. Needs, Europhys. Lett. **27**, 681 (1994).

39. F. Aryasetiawan and K. Karlsson, Phys. Rev. Lett. **73**, 1679 (1994).

40. A. Fleszar, A. A. Quong, and A. G. Eguiluz, Phys. Rev. Lett. **74**, 590 (1995); A. Fleszar, R. Stumpf, and A. G. Eguiluz, Phys. Rev. B **55**, 2068 (1997).

41. K.-H. Lee and K. J. Chang, Phys. Rev. B **49**, 2362 (1994); *ibid.* **54**, R8285 (1996).

42. H. Bross and M. Ehrnsperger, Z. Phys. B **97**, 17 (1995); M. Ehrnsperger and H. Bross, J. Phys.: Condens. Matter **9**, 1225 (1997).

43. A. G. Eguiluz, W. Ku, and J. M. Sullivan, Journ. Phys. Chem. Solids **61**, 383 (2000).

44. W. Ku and A. G. Eguiluz, Phys. Rev. Lett. **82**, 2350 (1999).

45. A. G. Eguiluz, J. M. Sullivan, and W. Ku, "Electronic Structure: Prediction and Applications", San Sabestian, Basque Country, Spain, October 4-6, 2000. Invited paper. Submitted to Int. J. Quantum Chem.

46. W. Ku, J. M. Sullivan and A.G. Eguiluz, to be published.

47. J. M. Sullivan and A. G. Eguiluz, to be published.

48. See for example W. Schülke in *Inelastic Scattering by Electronic Excitations*, "Handbook on Synchrotron Radiation" **3**, edited by G. Brown and D. E. Moneton.

49. For a review of norm modern pseudopotential theory see, for example, W. Pickett in *Pseudopotential Methods in Condensed Matter Applications*, Computer Physics Reports **9**, 115 (1989) and M. T. Yin and M. L. Cohen, Phys. Rev. B **25**, 7403 (1982).

50. D. J. Singh, *Planewaves, Pseudopotentials and the LAPW Method*, (Klumer, Boston 1994).

51. P. Blaha, K. Schwarz, P. Dufek, and R. Augustyn, WIEN95, Technical University of Vienna, 1995 (improved and updated UNIX version of the original copyrighted WIEN code, P. Blaha, K. Schwarz, P. Soratin, and S. B. Trickey, Comp. Phys. Commun. **59**, 399 (1990)).

52. D. J. Singh, Phys. Rev. B **43**, 6388 (1991).

53. A. Zangwill and P. Soven, Phys. Rev. A **21**, 1561 (1980).

54. S. J. A. van Gisbergen, F. Kootstra, P. R. T. Schipper, O. V. Gritsenko, J. G. Snijders, and E. J. Baerends, Phys. Rev. A **57**, 2556 (1998).

55. C. J. Umrigar and X. Gonze, Phys. Rev. A **50**, 3827 (1994); C. J. Umrigar and X. Gonze, in *High Performance Computing and Its Applications to the Physical Sciences,* edited by D. A. Browne *et al.* (World Scientific, Singapore, 1993).

56. I. Vasiliev, S. Öğüt, and J. R. Chelikowsky, Phys. Rev. Lett. **82**, 1919 (1999), and references therein; K. Yabana and G. F. Bertsch, physics/9903041. For work on clusters modelled by jellium see J. M. Pacheco and W. Ekardt, Phys. Rev. B **47**, 6667 (1993), and references therein.

57. M. Petersilka, E. K. U. Gross and K. Burke, cond-mat/0001154. K. Burke, M. Petersilka, and E. K. U. Gross, cond-mat/0001153.

58. J. C. Slater, Phys. Rev. **81**, 385 (1951).

59. E. D. Palik, *Handbook of Optical Constants of Solids* (Academic Press, New York, 1985).

60. J. P. Perdew and A. Zunger, Phys. Rev. B **23**, 5048 (1981).

61. Note that for an atomic system we may consider optimizing the value of α for each of the orbitals independently, although this is outside the formal framework of KS-DFT. This accounts for the range of α values quoted for the atom.

62. K. Sturm, Adv. Phys. **31**, 1 (1982). K. Sturm, E. Zaremba, and K. Nuroh, Phys. Rev. B **42**, 6973 (1990).

63. N. V. Smith, Phys. Rev. B **3**, 1862 (1971).

64. D. E. Eastmand and J. K. Cashion, Phys. Rev. Lett. **24**, 310 (1970). R. Courths, V Bachelier and S. Hüfner, Solid State Commun. **38** 887 (1981). R. C. Jaklevic and J. Lambe, Phys. Rev. B **12**, 4146. P. S. Williams, R. S. Williams, S. D. Kevan, D. Denley and D. A. Shirley, Phys. Rev. B **19**, 6164 (1979).

65. Note that Ref. [16] adopts the atomic sphere approximation, which is known to be less accurate in the evaluation of matrix elements (wave functions). F. Aryasetiawan, *private communication*.

66. Note that in contrast to the case of Ag, we use a real frequency sampling for the evaluation of the KS response function for Ni. The Pade' approximant method is not capable of reproducing the detailed structure of the loss function for energies so removed from the imaginary axis.

67. Of course one might ask whether the $X\alpha$ approach has any relevance for the case of Ni, as it is know that the bandwidth of the 3*d*-levels of Ni are much too broad compared to photoemission [68]. The $X\alpha$ does note help to remedy any of the deficiencies of the LDA electronic structure without the introduction of further spurious features; we concentrate solely on the LDA results since we expect that the salient features of the main loss features are independent of the exact bandwidths of the occupied levels.

68. F. J. Himpsel, J. A. Knapp and D. E. Eastman, Phys. Rev. B **19**, 2919 (1979). W. Eberhardt and E. W. Plummer, Phys. Rev. B **21**, 3245 (1980).

69. M. Nishijima, M. Jo, Y. Kuwahara and M. Onchi, Solid State Commun. **58** 75 (1986).

70. Note that in 0a we observe a similar behavior in $\mathrm{Re}\,\varepsilon$ for energies in the neighborhood of 10 eV.

71. M. Fuchs and M. Scheffler, Comput. Phys. Comm. **119**, 67 (1999).

72. N. Troullier and J. L. Martins, Phys. Rev. B **43**, 1993 (1991).

73. Of course, in the Compton regime [74], i.e. in the large energy and momentum regime, it is well known that the response properties of the all-electron and pseudopotential approaches disagree [75]. This is a direct reflection of the core-orthogonality problem, since the pseudo wave functions lack the atomic oscillations that all-electron results exhibit.

74. P. Eisenberger and P. M. Platzman, Phys. Rev. A 2, 415 (1970).

75. P. Delaney, B. Králik and S. G. Louie, Phys. Rev. B **587**, 4320 (1998). Phys. Rev. B **59**, 7907 (1999).

76. M. Bockstedte, A. Kley, J. Neugebauer, and M. Scheffler, Comp. Phys. Comm. **107**, 187 (1997).

77. In the case of Ag, the ground state calculations are based on the fcc lattice with the experimental lattice constant. The cases of Cd and Zn are treated in the bcc structure, although the true crystal structure is hcp. The reason for so doing is a technical detail related to conventions of the respective ground state programs that would digress too much in discussing it here [78]. The ambiguity revealed herein is independent of this fine; we concentrate solely on the theoretical line shapes obtained with the two methods for a given exchange-correlation functional, which we take to be the LDA in the case of Ag and Cd and the $X\alpha$ in the case of Zn. We do note that we choose the bcc lattice constants in Cd and Zn such that the average density for these crystals is the same as that of the hcp structures. By following this procedure, we ensure that the relative location of the *d* levels to the nominal plasmon energy is the same in these cubic crystals as in the true structures.

78. The WIEN [51] and fhi96md [76] programs adopt slightly different choices of unit cells for the Bravais lattice and Wigner-Seitz cells for the reciprocal lattice. Hence, it is difficult to find a wave vector common to the discrete reciprocal space meshes used in the two ground state calculations. Overcoming this technical difficult will be the subject of a future publication [47], but is irrelevant for the essential physics discussed herein.

79. S. G. Louie, S. Froyen and M. L. Cohen, Phys. Rev. B **26**, 1738 (1982).

80. Non-linear core correction papers for lattice constants

81. The pseudopotential results for Ag are obtained with a plane wave cutoff of 85 Ry. The corresponding pseudopotential was generated from the Troullier-Martins [72] procedure for angular momenta up to $l = 2$, taking the *s*-component to be local. The core radius for matching the pseudopotential wave functions to the all-electron results are 2.48, 2.60 and 2.36 a_0 for $l = 0,1,2$ respectively.

82. One may question why we choose to concentrate on the LDA results here, when we have argued in earlier in this Chapter that the $X\alpha$ approximation with $\alpha = 0.82$ yields a KS electronic structures which seems more physically plausible. We choose to focus on the LDA results here to provide definitive proof that the disagreement we find between the two theoretical methods is not a consequence of some spurious feature of the $X\alpha$ per se.

83. Clearly in an approximate KS scheme, such as the LDA, one is not guaranteed that the KS density is the same as the true density. However, one can easily demonstrate that for the diagonal elements of Eqs. (32) and (34), the right-hand side depends only on the average charge density which is identical for both the KS and many-body system whether it is obtained with the exact or an approximate exchange-correlation functional.

84. For the pseudopotential ground state calculation for Cd, we use a plane wave cutoff of 80 Ry with a Troullier-Martin's [72] pseudopotential including angular momentum up to $l = 2$ and with core radii given by 1.30a_o, 1.56 a_0, and 0.575 a_0 for $l = 0,1,2$ respectively. The *s*-component of the pseudopotential is taken to be local.

85. Note that in the pseudopotential approach, for conceptual closure, this requires a corresponding $X\alpha$ pseudopotential. Surprisingly, we find this has very little effect on the band structure; an $X\alpha$ valence electron calculation with either an $X\alpha$ or LDA pseudopotential yields nearly identical energy dispersion and loss functions. This independence of the band structure from the pseudopotential is most likely because the self-interactions act to mask the proper atomic shell structure one would find in a self-interaction-free evaluation of the potential [86].

86. J. D. Talman and F. Shadwick, Phys. Rev. A **14**, 36 (1976).

87. For the pseudopotential ground state calculations for Zn we have used a plane wave cutoff of 85 Ry and a Troullier-Martins pseudopotential [72] with angular momentum core radii of 2.16a_o, 2.32 a_o, and 2.06 a_o for $l = 0,1,2$ respectively and assuming the bcc crystal lattice as discussed earlier in this Section.

88. We do, of course, suspect that the *d* levels of Cd also suffer from the self-interaction problem and will be lower than the LDA values as used in the present work. This

will not change the conclusions regarding the pseudopotential versus all-electron results and should lead

89. R. Keyling, W. D. Schöne, and W. Ekardt, Phys. Rev. B **61**, 1670 (2000).

90. I. Campillo, V. M. Silkin, J. M. Pitarke, E. V. Chulkov, A. Rubio and P. M. Echenique, Phys. Rev. B **61**, 13484 (2000).

91. I. Campillo, J. M. Pitarke, A. Rubio, P. M. Echenique, Phys. Rev. B **62**, 1500 (2000).

92. M. Städele, J. A. Majewski, P. Vogl and A. Görling, Phys. Rev. Lett. **79**, 2089 (1997).

93. M. Städele, M. Moukara, J. A. Majewski, P. Vogl andA. Görling, Phys. Rev. B **59**, 10031 (1999).

94. D. M. Bylander and L. Kleinman, Phys. Rev. B **52**, 14566 (1995).

95. M. H. Hybertsen and S. G. Louie, Phys. Rev. B **35**, 5585 (1987).

96. E. K. U. Gross and W. Kohn, Adv. Quantum Chem. **21**, 255 (1990).

97. E. K. U. Gross, J. F. Dobson, and M. Petersilka, *Density Functional Theory*, edited by R. F. Nalewajski (Springer, New York, 1996).

98. G. Vignale and W. Kohn, Phys. Rev. Lett. **77**, 2037.

99. See, for example, *Solid State Physics*, N. W. Ashcroft and N. D. Mermin, (Harcourt Brace College Publishers, Fort Worth).

100. H. J. Monkhurst and J. D. Pack, Phys. Rev. B **13**, 5188 (1974). Another common choice of sampling is given in D. J. Chadi and M. L. Cohen, Phys. Rev. B **8**, 5747 (1973).

101. M. E. Rose, *Elementary Theory of Angular Momentum*, (John Wiley & Sons, New York, 1957).

102. N. D. Mermin, Rev. Mod. Phys. **64**, 3 (1992). D. G. Bell, Rev. Mod. Phys. **26**, 3111 (1954).

103. J. M. Sullivan, *unpublished*.

104. T. Matsubara, Prog. Thoer. Phys. **14**, 351 (1955).

105. H. J. Vidberg and J. W. Serene, J. Low Temp. Phys. **2**9, 179 (1977). K.-H. Lee and K. J. Chang, Phys. Rev. B **54**, R8285 (1996). K. S. D. Beach, R. J. Gooding and F. Marsiglio, Phys. Rev. B **61**, 5147 (2000).

106. O. K. Anderson, Phys. Rev. B **12**, 3060 (1975). O. K. Anderson and O. Jepsen, Phys. Rev. B **6**, 3584 (1972).

107. D. D. Koelling, J. Phys. Chem. Solids **33**, 1335 (1972). D. D. Koelling and G. O. Arman, J. Phys. F: Met. Phys. **5**, 2041 (1972).

108. E. Wimmer *et al.*, Phys. Rev. B **24**, 864 (1981). M. Weinert, E. Wimmer and A. J. Freeman, Phys. Rev. B **26**, 4571 (1982).

109. T. L. Loucks, The Augmented-Plane-Wave Method (Benjamin, New York, 1967).

110. J. M. Sullivan, research notes, *unpublished*.

111. The allowed (non-zero) coefficients of the KS potential or charge density, when expanded in the spherical (lattice) harmonics, can be restricted to a very few (l,m) combinations using symmetry considerations. For example, one can show that no coefficients with odd angular momentum quantum number, l, are allowed. See for example "Lattice Harmonics", J. M. Sullivan, research notes, *unpublished* and/or Ref. [50].

112. "Matrix Elements in the LAPW Basis", J. M. Sullivan, research notes, *unpublished*.

113. "Symmetries and the Kohn-Sham Response Function in the LAPW Basis", J. M. Sullivan, research notes, *unpublished*.

114. "The Little Group of $\tilde{q}$ ", J. M. Sullivan, research notes, *unpublished*.

115. Note that Ni has a 3*p* semi-core level that is treated with an $l = 1$ local orbital. In the LAPW ground state package which we make use of in this work [], we are restricted to one additional local orbital in the basis. We expect that inclusion of an $l = 1$ local orbital will not dramatically affect any of the present results.

116. For details about the Message Passing Interface library see the "Message Passing Interface Standard", available electronically at http://www-unix.mcs.anl.gov/mpi/index.html.

117. For simplicity, one can think of a processing element as a single processor, although multi-processor single processing element architectures exist.

118. See for example Richard M. Stallman in *The C Preprocessor*, for GCC version 2 with manual available electronically at http://gcc.gnu.org/onlinedocs/cpp_toc.html.

119. The syntax for preprocessor directives is that they begin with the # character in the first character position of a line. They can be carried over to additional lines with the continuation character \.

120. The flag '-D' can be used to define a macro on the command line at compile time.

121. Note that macros are case sensitive. Furthermore, to force macro substitution every where in the source file, rather than just on lines that begin with '#', one must supply the additional preprocessor flag '-F' on the Cray T3E.

122. A. Schindlmayr and R. W. Godby, Phys. Rev. B **51**, 10427 (1995).

123. Of course, in practice there is also a contribution of $-N/|\vec{x}|$ in the total field due to the N protons in the nucleus which exhibit an attractive force on all the electrons.

124. A. Gorling, Phys. Rev. A **55**, 2630 (1997).

125. D. M. Bylander and L. Kleinman, Phys. Rev. Lett. **74**, 3660 (1995).

126. D. M. Bylander and L. Kleinman., Phys. Rev. B **54**, 7891 (1996).

127. D. M. Bylander and L. Kleinman, Phys. Rev. B **55**, 9432 (1997).

128. C.-O. Ambladh and U. von Barth, Phys. Rev. B **31**, 3231 (1985).

129. A. Görling and M. Ernzerhof, Phys. Rev. A **51**, 4501 (1995).

130. E. K. U. Gross, M. Petersilka and T. Grabo, ACS Symposium Series, 629 (1996).

131. F. Herman, J. P. Van Dyke and I. B. Ortenburger, Phys. Rev. Lett. **22**, 807 (1969).

132. L. J. Sham, Phys. Rev. B **32**, 3876 (1985).

133. L. J. Sham and M. Schlüter, Phys. Rev. B **32**, 3883 (1985).

134. Z. Qian and V. Sahni, Int. Journ. Quant. Chem. **80**, 555 (2000).

135. H. Yang and M. Levy, Phys. Rev. Lett. **65**, 1036 (1990).

136. V. R. Shaginyan, Phys. Rev. A **47**, 1507 (1993).

137. R. W. Godby, M. Schlüter and L. J. Sham, Phys. Rev. B 36, 6497 (1987). *Ibid*., Phys. Rev. B **37**, 10159 (1988)

138. E. Engel and R. M. Dreizler, Journ. Comp. Chem. **20,** 31 (1999).

139. R. van Leeuwen and E. J. Baerends, Phys. Rev. A **49**, 2421 (1994).

140. M. Levy and A. Görling, Phys. Rev. B **53**, 969 (1996).

141. A. Görling, M. Levy and J. P. Perdew, Phys. Rev. B **47**, 1167 (1993).

142. J. B. Krieger, Y. Li and G. J. Iafrate, Phys. Rev. B **45**, 101 (1992).

143. M. Levy, Phys. Rev. A **26**, 1200 (1982).

144. M. Levy in *Density Functional Theory*, edited by E. K. U. Gross and R. M. Dreizler (Plenum Press, New York, 1995).

145. S. Erhard and E. K. U. Gross, Phys. Rev. A **53**, R5 (1996).

146. J. P. Perdew and M. R. Norman, Phys. Rev. B **26**, 5445 (1982).

147. J. P. Perdew, R. G. Parr, M. Levy and J. L. Balduz, Jr., Phys. Rev. Lett. **49**, 1691 (1982).

148. M. E. Casida, Phys. Rev. A 51, 2005 (1995).

149. M. M. Rieger and P. Vogl, Phys. Rev. A **52**, 282 (1995).

150. K. Burke, M. Ernzerhof and J. P. Perdew, Chem. Phys. Lett. **31**, 115 (1997).

151. K. Burke, M. Petersilka and E. K. U. Gross, cond-mat/0001153.

152. M. Ernzerhof, Chem. Phys. Lett. **13**, 499 (1996).

153. C. Filippi, C. J. Umrigar, and X. Gonze, Phys. Rev. A **54**, 4810 (1996).

154. C. Filippi, C. J. Umrigar and X. Gonze, J. Chem. Phys. **107**, 9994 (1997).

155. T. Grabo and E. K. U. Gross, Int. Journ. Quant. Chem. **64**, 95 (1997).

156. The occupation functions, $n_{j,j'}$ and $n_{S,j,j'}$ refer to the spectral weight of the appropriate Green's function projected onto the KS basis. For the quasiparticle occupation function, $n_{j,j'}$, the appropriate Green's function is that for the correlated many-body system, whereby $n_{j,j'}$ is obtained as $n_{j,j'} = \frac{1}{2\pi}\int d\omega A_{j,j'}(\omega)$. A similar equation obtains for $n_{S,j,j'}$ for which the appropriate Green's function is the KS non-interacting Green's function, which is diagonal in the KS basis and has simple poles at the KS single-particle eigenvalues.

157. The restricted Bloch basis, discussed in Appendix C is an equally valid choice of basis functions that adhere to the periodicity of the Bravais lattice and are efficient for the inversion of the KS response function.

158. The expression of Ref. [138] is that $\left\langle \vec{k},h\left|\hat{v}_{HF}^{KS}\right|\vec{k},h\right\rangle = \left\langle \vec{k},h\left|\hat{v}_{XC}\left[n\right]\right|\vec{k},h\right\rangle$ for the state, $\phi_{\vec{k},h}$, corresponding to the valence band maxima.

159. We are indebted to M. Fuchs for providing the *ab initio* KLI pseudopotentials for Si.

160. J. M. Sullivan, M. Fuchs, and A. G. Eguiluz, to be published.

161. As we have done here, and in the rest that follows, we will use the notation A/B when referring to the calculations. A and B can be one of L (LDA), E (exchange), K (KLI), HF (Hartree-Fock), or G (GGA) used to represent the various types of combinations of pseudopotential and exchange-correlation potential combinations when encounter in the present work and in the literature. An exchange-only KLI potential approximation is thus KE (KLI-E), whereas a Hartree-Fock-core calculation with an KLI treatment of exchange-only with generalized gradient correlation would be KEG/HF.

162. Schülke Phys. Rev. B , (1985?). IXS results.

163. *Numerical Data and Functional Relationships in Science and Technology*, edited by K.-H. Hellwege, Landolt-Börnstein, New Series, Group III, Vol 17, edite by O. Madelung, M Schulz, and H. Weiss (Springer, Berlin, 1982).

164. D. Straub, L. Ley, and F. J. Himpsel, Phys. Rev. Lett. B **47**, 2130 (1993).

165. J. E. Ortega and F. J. Himpsel, Phys. Rev. B **47**, 2130 (1993).

166. F. Gygi and A. Baldereschi, Phys. Rev. B **34**, 4405 (1986).

167. Typical numbers used in the calculations correspond to 512 wave vectors in the BZ, 300 bands in the KS response function and in the "screening" of the Fock potential. The matrix representation includes the 11 smallest shells of reciprocal lattice vectors for the fcc lattice. This corresponds to a plane wave cutoff, $\vec{G}_{\max}^2 / 2$, of 137 *eV*.

168. P. B. Johnson and R. W. Christy, Phys. Rev. B **9**, 5056 (1974).

169. C. Wehenkel and B. Gauthé, Phys. Stat. Sol. (b) **64**, 515 (1974).

170. E. G. Maksimov, I. I. Mazin, S. N. Rashkeev and Y. A. Uspenski, J. Phys. F: Met. Phys. **18**, 833 (1988).

171. B. Adolph, V. I. Gavrilenko, K. Tenelsen, F. Bechstedt and R. Del Sole, Phys. Rev. B **53**, 9797 (1996). V. I. Gavrilenko and F. Bechstedt, Phys. Rev. B **55**, 4343 (1997).

172. I. I. Mazin, D. J. Singh, and C. A.-Draxl, Phys. Rev. B **59**, 411 (1999).

173. S. Baroni and R. Resta, Phys. Rev. B **33**, 7017 (1986).

174. K.-H. Lee and K. J. Chang, Phys. Rev. B **49**, 2362 (1994).

Appendices

Appendix A: Brillouin Zone Integrations

The evaluation of various physical quantities requires summations over vectors of the reciprocal lattice. In the most general case, this summation consists of two separate contributions: (i) integration over the primitive unit cell of reciprocal space and (ii) a summation over the reciprocal lattice vectors. In this Appendix, we discuss several technical aspects of these wave vector summations, including the coordinate representation of wave vectors of the reciprocal lattice, the choice of an *even* or an *odd*-mesh and the use of symmetry to reduce wave vector integrations.

Brillouin Zones and Primitive Zones

There are two typical choices for the primitive cell of reciprocal space. The primitive cell can be chosen to coincide with that of the conventional definition of the *Brillouin zone* (BZ) [99], being of complex geometric shape, and not particularly convenient for numerical work. A more judicious choice is that region of wave vector space of parallelepiped shape, which is spanned by the basis vectors of the reciprocal lattice. Adopting this convention, the wave vectors lying inside this parallelepiped primitive zone (PZ), $\vec{k}$, can be expressed as

$$\vec{k} = \mathbf{B}\underset{\rightarrow}{k}, \tag{66}$$

where the wave vector $\underset{\rightarrow}{k}$ is expressed in primitive coordinates $\underset{\rightarrow}{k} = (\beta_1, \beta_2, \beta_3)$, with $0 \le \beta_i < 1$ and **B** is a matrix of rank three that transforms the wave vectors from primitive coordinates to Cartesian coordinates. Via the strict inequality on the upper bound of the β_i, this convention avoids double counting points in the PZ which are related by a vector of the reciprocal lattice.

The set of all points specified by the 3-tuples $(\beta_1, \beta_2, \beta_3)$ make up the PZ; there is a great deal of flexibility in how to choose a particular set of $(\beta_1, \beta_2, \beta_3)$. The two most common choices are the *odd-mesh* and *even-mesh* in the Monkhorst-Pack [100] sense. The distinction between the two choices comes about because one excludes the zone center in the odd-mesh, while it is include in the even mesh.

For ground state calculations, the odd-mesh is more efficient. This is because the points on the odd-mesh tend to avoid high symmetry directions, in particular the boundaries of the PZ, and thus one only needs very few linearly independent vectors (these being vectors of the irreducible wedge as defined below) to represent a large number of points in the PZ. However, in typical dynamical calculations such as those we encounter in Chapter One, one must evaluate matrix elements of functions of two spatial variables. A typical example is the Fourier coefficients of the Kohn-Sham (KS) response function, χ_S (see Appendix C), written here for zero frequency

$$\chi_{S,\vec{G},\vec{G}'}(\vec{q}) = 2\sum_{\vec{k}}\sum_{j,j'}\frac{f_{\vec{k},j} - f_{\vec{k}+\vec{q},j'}}{E_{\vec{k},j} - E_{\vec{k}+\vec{q},j'} + i0^{+}} \\ \text{x}\left\langle \vec{k},j\left|e^{-i(\vec{q}+\vec{G})\cdot\hat{\vec{x}}}\right|\vec{k}+\vec{q},j'\right\rangle\left\langle \vec{k}+\vec{q},j'\left|e^{i(\vec{q}+\vec{G}')\cdot\hat{\vec{x}}}\right|\vec{k},j\right\rangle \quad , \tag{67}$$

where the wave vector integration runs over vectors of the PZ. In systems with inversion symmetry, for every wave vector $\vec{k}$ in the PZ, there corresponds another point $-\vec{k}$, so that in practice $\vec{k}+\vec{q}=\vec{0}$ will be encountered in the summation over vectors in the PZ. Of course, one could resort to using two different meshes: an odd-mesh for the dummy variable $\vec{k}$ in Eq. (67) and choosing the external variable $\vec{q}$ as a member of an even mesh, so that $\vec{k}+\vec{q}$ is also a member of an odd-mesh. For simplicity of implementation, the present work makes use of an even-mesh for all numerical work. We next discuss the use of symmetry to further reduce the wave vector summations.

In general, from purely geometrical arguments one can reduce the number of linearly independent wave vectors in the PZ by utilizing the rotational symmetries of the full symmetry group of the Bravais lattice. The so-obtained minimum set of wave vectors are referred to as the *irreducible wedge of the primitive zone* (IWPZ); in the case in which one chooses the PZ to coincide with the BZ, we refer to these points as the *irreducible wedge of the Brillouin zone* (IWBZ). It should be noted that in the literature is the oft-used expression, IBZ, when referring to either the IWPZ or IWBZ as defined here.

The "Star of $\tilde{k}$"

Denoting by $\left\{\tilde{k}\right\}$ the set of all wave vectors belonging to the IWPZ and by $\{\mathbf{S}\}$ the set of all rotations (possibly improper) belonging to the symmetry group of the Bravais lattice, we have

$$\left\{\tilde{k}\right\} = \left\{\vec{k} \in PZ \mid \forall \vec{k}' \in PZ, \vec{k}' \neq \vec{k}, \forall \mathbf{S} \in \{\mathbf{S}\}, \mathbf{S}\vec{k} \neq \vec{k}'\right\}. \tag{68}$$

For a fixed wave vector $\tilde{k}$ of the IWPZ, the set of wave vectors of the PZ obtained by application of all the symmetry operations is referred to as the "star of $\tilde{k}$". We denote by $\{\mathbf{S}\}_{\tilde{k}}$ the minimum set of such operations required to generate the star of $\tilde{k}$. With this convention, summations over wave vectors in the PZ can be written equivalently as a summation over the IWPZ and the appropriate stars

$$\sum_{\vec{k}}^{PZ} = \sum_{\tilde{k}}^{IWPZ} \sum_{\mathbf{S}}^{\{\mathbf{S}\}_{\tilde{k}}} . \tag{69}$$

For simplicity of notation in all that follows, we adopt the shorthand notation

$$\sum_{\tilde{k}}^{IWPZ} = \sum_{\tilde{k}} .$$

We next discuss how the form of Eq. (69) can be used to reduce the wave vector summations that we encounter in the present calculations, including functions of one wave vector and two wave vectors.

Let us consider a function of one space variable. As a specific example, consider the Kohn-Sham orbital density, $n_{\vec{k},j}(\vec{x}) \equiv \left|\phi_{\vec{k},j}(\vec{x})\right|^2$, which we encounter in computing the electron charge density of density functional theory (see Appendix H). It can be shown quite readily, that $n_{\vec{k},j}(\vec{x})$ satisfies the following symmetry identity

$$n_{\mathbf{S}\tilde{k},j}(\vec{x}) = n_{\tilde{k},j}(\vec{x}). \tag{70}$$

In the present example, Eq. (69) when combined with Eq. (70) yields

$$n(\vec{x}) = \sum_{\vec{k}}^{} \sum_{j}^{occ.} n_{\vec{k},j}(\vec{x}) = \sum_{\tilde{k}}^{} \sum_{\mathbf{S}}^{\{\mathbf{S}\}_{\tilde{k}}} \sum_{j}^{occ.} n_{\tilde{k},j}(\vec{x}) = \sum_{\tilde{k}}^{} w_{\tilde{k}} \sum_{j}^{occ.} n_{\tilde{k},j}(\vec{x}), \tag{71}$$

where $w_{\tilde{k}}$, is the number of members of the star of $\tilde{k}$. It is clear from Eq. (71) that one only need to construct the orbital densities for wave vectors of the IWPZ, thereby greatly reducing the number of numerical evaluations needed in ground state calculations.

As an example of a function of two space variables, consider the KS response function $\chi_S(\vec{x},\vec{x}')$ (see Appendix C). The space-time Fourier transform of the KS response function is

$$\begin{aligned}\chi_{S,\vec{G},\vec{G}'}(\vec{q},E) = {} & \frac{1}{\Omega} \sum_{\vec{k},j,j'} \frac{f_{\vec{k},j} - f_{\vec{k}+\vec{q},j'}}{E + E_{\vec{k},j} - E_{\vec{k}+\vec{q},j'} + i0^+} \\ & \times \left\langle \vec{k},j \left| e^{-i\left(\vec{q}+\vec{G}\right)\cdot\hat{\vec{x}}} \right| \vec{k}+\vec{q},j' \right\rangle \left\langle \vec{k}+\vec{q},j' \left| e^{i\left(\vec{q}+\vec{G}'\right)\cdot\hat{\vec{x}}} \right| \vec{k},j \right\rangle .\end{aligned} \tag{72}$$

In Eq. (72), the wave vectors $\vec{k}$, $\vec{q}$ and $\vec{k}+\vec{q}$ lie in the PZ, and $\vec{G}$ is a vector of the reciprocal lattice. We first rewrite the wave vector summation of Eq. (72) as a summation over the IWPZ and the appropriate stars

$$\chi_{S,\vec{G},\vec{G}'}(\vec{q},E)=\frac{1}{\Omega}\sum_{\tilde{k},j,j'}\sum_{\mathbf{S}}^{\{\mathbf{S}\}_{\tilde{k}}}\frac{f_{\tilde{k},j}-f_{\mathbf{S}\tilde{k}+\vec{q},j'}}{E+E_{\tilde{k},j}-E_{\mathbf{S}\tilde{k}+\vec{q},j'}+i0^{+}}$$
$$\mathrm{x}\left\langle \mathbf{S}\tilde{k},j\left|e^{-i\left(\vec{q}+\vec{G}\right)\cdot\hat{\vec{x}}}\right|\mathbf{S}\tilde{k}+\vec{q},j'\right\rangle\left\langle \mathbf{S}\tilde{k}+\vec{q},j'\left|e^{i\left(\vec{q}+\vec{G}'\right)\cdot\hat{\vec{x}}}\right|\mathbf{S}\tilde{k},j\right\rangle . \tag{73}$$

We then note that the wave vector, $\mathbf{S}\tilde{k}+\vec{q}=\mathbf{S}\tilde{k}+\vec{q}-\vec{H}$, itself lying in the PZ, can be expressed equivalently in terms of a symmetry, $\mathbf{S}'$, and wave vector, $\tilde{k}'$ lying in the IWPZ

$$\mathbf{S}\tilde{k}+\vec{q}-\vec{H}=\mathbf{S}'\tilde{k}', \tag{74}$$

with $\mathbf{S}'$ belonging to the set of symmetry operations, $\{\mathbf{S}\}_{\tilde{k}'}$, that define the star of $\tilde{k}'$. To determine the matrix element $\left\langle \mathbf{S}\tilde{k},j\left|e^{-i\left(\vec{q}+\vec{G}\right)\cdot\hat{\vec{x}}}\right|\mathbf{S}'\tilde{k}',j'\right\rangle$ we make use of the symmetry properties of the KS wave functions (see Appendix B)

$$\phi_{\mathbf{S}\vec{k},j}(\vec{x})=e^{i\mathbf{S}\vec{k}\cdot\vec{\tau}}\phi_{\vec{k},j}\left(\mathbf{S}^{-1}\left(\vec{x}-\vec{\tau}\right)\right).$$

This symmetry identity, when applied to states with wave vectors $\mathbf{S}\tilde{k}$ and $\mathbf{S}'\tilde{k}'$ obtains the following real space integral needed in evaluating the matrix elements of Eq. (73)

$$e^{-i\mathbf{S}\tilde{k}\cdot\vec{\tau}}e^{i\mathbf{S}'\tilde{k}'\cdot\vec{\tau}'}\int_{\Omega}d^3x\phi^*_{\tilde{k},j}\left(\mathbf{S}^{-1}\left(\vec{x}-\vec{\tau}\right)\right)e^{-i\left(\vec{q}+\vec{G}\right)\cdot\vec{x}}\phi_{\tilde{k}',j}\left(\mathbf{S}'^{-1}\left(\vec{x}-\vec{\tau}'\right)\right). \tag{75}$$

In the case of an expansion of the KS states in plane waves

$$\phi_{\tilde{k},j}\left(\vec{x}\right)=\frac{1}{\sqrt{\Omega}}\sum_{\vec{G}}\phi_{\tilde{k},j}\left(\vec{G}\right)e^{i\left(\tilde{k}+\vec{G}\right)\cdot\vec{x}},$$

this integral can then be carried out analytically to yield

$$\left\langle \mathbf{S}\tilde{k},j\left|e^{-i\left(\vec{q}+\vec{G}\right)\cdot\hat{\vec{x}}}\right|\mathbf{S}'\tilde{k}',j'\right\rangle=\sum_{\vec{g}'}\phi^*_{\tilde{k},j}\left(\mathbf{S}^{-1}\left(\mathbf{S}'\vec{g}'-\vec{H}-\vec{G}\right)\right)\phi_{\tilde{k}',j}\left(\vec{g}'\right)$$
$$\text{x}\,e^{i\mathbf{S}'\vec{g}'\cdot\left(\vec{\tau}-\vec{\tau}'\right)}e^{-i\left(\vec{H}+\vec{G}\right)\cdot\vec{\tau}}. \tag{76}$$

Clearly from Eq. (76) we only need the Fourier coefficients, $\phi_{\tilde{k},j}\left(\vec{G}\right)$ and $\phi_{\tilde{k}',j'}\left(\vec{G}\right)$, for wave vectors $\tilde{k}$ and $\tilde{k}'$ in the IWPZ. We conclude this Appendix noting that, although the result in Eq. (76) has been derived explicitly making use of a Fourier expansion, one can apply a similar procedure to the case of the evaluation of matrix elements of all-electron wave functions. In the case of linearized augmented plane waves, the crucial ingredient in simplifying the resulting real space integration, in particular the angular integration makes use of the rotational properties of the spherical harmonics

$$Y_{lm}\left(\mathbf{S}^{-1}\hat{x}\right)=\sum_{m'=-l}^{l}S^{l}_{m',m}Y_{lm}{}'\left(\hat{x}\right).$$

In this equation, the complex coefficients $S^{l}_{m',m}$ are the rotation matrices as defined in Rose [101]. An explicit derivation of the matrix elements for the all-electron calculations of Chapter One is given in Appendix D, as well as comments on the wave vector integrations used in those calculations.

Appendix B:The Use of Symmetry in *Ab Initio* Calculations

This Appendix reviews the use of symmetry in the present numerical techniques. Although we discuss in detail applications of group theoretic concepts, we do not provide a review of the formalism of group theory and/or symmetry considerations for all types of Bravais lattices. Instead, we concentrate on subtle points of implementation that are not found in the literature and may be useful for understanding the specific details of the numerical algorithms. For a more thorough discussion of group theory, we direct the reader to Ref. [102].

We begin with a discussion of the symmetry properties of the KS wave functions, both in real space and momentum space. We then consider functions of one and two variables, such as the charge density and dynamical density response function respectively. The specific means by which these symmetry properties are utilized for the most demanding numerical kernels is covered in the relevant Appendices, including Kohn-Sham response function (see Appendix C), matrix elements of the Hartree-Fock operator (see Appendix F), matrix elements in the LAPW basis (see Appendix D), and Brillouin zone integrations via the special point technique (see Appendix A).

Symmetries of the KS States

In a crystal, the most general form of a symmetry operation consists of a rotational part (including possible improper rotations) and a translational component. We denote the total operation by the pair $\{\mathbf{S},\vec{\tau}\}$, where $\mathbf{S}$ is a 3x3 matrix that is a member of $SO(3)$ and $\vec{\tau}$ is referred to as the corresponding *partial lattice translation*. The set of all pairs $\{\mathbf{S},\vec{\tau}\}$, i.e. the set of all symmetry operations of the crystal, constitute the symmetry group of the Bravais lattice. We denote by $\hat{P}_{\{\mathbf{S},\vec{\tau}\}}$ the operation, which, when acting on functions of real space variables, transforms the arguments of these functions according to $\vec{x} \to \mathbf{S}^{-1}(\vec{x}-\vec{\tau})$. The Hamiltonian, $\hat{H}$, of the system commutes with all of these symmetry operations

$$\left[\hat{P}_{\{\mathbf{S},\vec{\tau}\}},\hat{H}\right]_{-}=0\,. \tag{77}$$

This applies to both the many-body Hamiltonian and the KS Hamiltonian. Let us consider the latter case. Application of the commutator in Eq. (77) to the KS state $\left|\vec{k},j\right\rangle$, and using the KS equation (see Appendix H)

$$\hat{H}_{KS}\left|\vec{k},j\right\rangle = E_{\vec{k},j}\left|\vec{k},j\right\rangle, \tag{78}$$

obtains

$$\hat{H}\left(\hat{P}_{\{\mathbf{S},\vec{\tau}\}}\left|\vec{k},j\right\rangle\right) = E_{\vec{k},j}\left(\hat{P}_{\{\mathbf{S},\vec{\tau}\}}\left|\vec{k},j\right\rangle\right). \tag{79}$$

For non-degenerate states $\left|\vec{k}, j\right\rangle$, this leads to the following identity

$$\hat{P}_{\{\mathbf{S},\vec{\tau}\}}\left|\vec{k}, j\right\rangle = e^{-i\mathbf{S}\vec{k}\cdot\vec{\tau}}\left|\mathbf{S}\vec{k}, j\right\rangle. \tag{80}$$

For a degenerate state belonging to a complex of m degenerate states of energy, $E_{\vec{k},j}$, the right hand side of Eq. (80) is a linear combination of the degenerates states with appropriate weights

$$\hat{P}_{\{\mathbf{S},\vec{\tau}\}}\left|\vec{k}, j\right\rangle = e^{-i\mathbf{S}\vec{k}\cdot\vec{\tau}}\sum_i U_{j,i}\left(\vec{k}\right)\left|\mathbf{S}\vec{k}, i\right\rangle. \tag{81}$$

The summation in Eq. (81) runs over the degenerate levels, and the matrix of coefficients $U_{i,j}\left(\vec{k}\right)$ is unitary

$$\sum_k U_{i,k}U^*_{k,j} = \delta_{i,j}. \tag{82}$$

Let us consider the symmetry identities expressed in Eqs. (80) and (81) in the $\vec{x}$-basis, for which they read

$$\phi_{\mathbf{S}\vec{k},j}\left(\vec{x}\right) = e^{i\mathbf{S}\vec{k}\cdot\vec{\tau}}\phi_{\vec{k},j}\left(\mathbf{S}^{-1}\left(\vec{x}-\vec{\tau}\right)\right) \tag{83}$$

and

$$\phi_{\mathbf{S}\vec{k},j}\left(\vec{x}\right) = e^{i\mathbf{S}\vec{k}\cdot\vec{\tau}}\sum_i U_{i,j}\left(\vec{k}\right)\phi_{\vec{k},i}\left(\mathbf{S}^{-1}\left(\vec{x}-\vec{\tau}\right)\right). \tag{84}$$

Also consider the above symmetry identities to the momentum representation of the KS wave functions. The Fourier coefficient, $\phi_{\vec{k},j}\left(\vec{G}\right)$, of the state $\left|\vec{k},j\right\rangle$ defined as

$$\phi_{\vec{k},j}\left(\vec{G}\right)\equiv\left\langle\vec{k}+\vec{G}\middle|\vec{k},j\right\rangle=\frac{1}{\sqrt{\Omega}}\int_{\Omega}d^3xe^{-i\left(\vec{k}+\vec{G}\right)\cdot\vec{x}}\phi_{\vec{k},j}\left(\vec{x}\right),$$

satisfies a symmetry identity similar to Eqs. (83) and (84). For simplicity, we only consider the case of non-degenerate states; generalization to the case of degenerate states is straightforward.

We wish to evaluate the coefficient $\left\langle\mathbf{S}\vec{k}+\mathbf{S}\vec{G}\middle|\mathbf{S}\vec{k},j\right\rangle$ relative to the Fourier coefficients of the state $\left|\vec{k},j\right\rangle$. Applying the definition of the $\left\langle\mathbf{S}\vec{k}+\mathbf{S}\vec{G}\middle|\mathbf{S}\vec{k},j\right\rangle$ we have

$$\left\langle\mathbf{S}\vec{k}+\mathbf{S}\vec{G}\middle|\mathbf{S}\vec{k},j\right\rangle=\frac{1}{\sqrt{\Omega}}\int_{\Omega}d^3xe^{-i\mathbf{S}\left(\vec{k}+\vec{G}\right)\cdot\vec{x}}\phi_{\mathbf{S}\vec{k},j}\left(\vec{x}\right).$$

Making use of the symmetry identity of Eq. (83) and the Fourier expansion of the state $\phi_{\vec{k},j}\left(\mathbf{S}^{-1}\left(\vec{x}-\vec{\tau}\right)\right)$ leads to

$$\left\langle\mathbf{S}\vec{k}+\mathbf{S}\vec{G}\middle|\mathbf{S}\vec{k},j\right\rangle=\frac{1}{\sqrt{\Omega}}\int_{\Omega}d^3xe^{-i\left(\mathbf{S}\vec{k}+\mathbf{S}\vec{G}\right)\cdot\vec{x}}\left[\frac{1}{\sqrt{\Omega}}\sum_{\vec{g}}\phi_{\vec{k},j}\left(\vec{g}\right)e^{i\left(\mathbf{S}\vec{k}+\mathbf{S}\vec{g}\right)\cdot\vec{x}}e^{-i\mathbf{S}\vec{g}\cdot\vec{\tau}}\right].$$

The coefficient can be further reduced to yield

$$\left\langle\mathbf{S}\vec{k}+\mathbf{S}\vec{G}\middle|\mathbf{S}\vec{k},j\right\rangle=\phi_{\mathbf{S}\vec{k},j}\left(\mathbf{S}\vec{G}\right)=e^{-i\mathbf{S}\vec{G}\cdot\vec{\tau}}\phi_{\vec{k},j}\left(\vec{G}\right).\tag{85}$$

Equation (85) is of great use in reducing the number of necessary matrix element evaluations in the construction of physical quantities.

Symmetries of Functions of One-Spatial Variable

This Section reviews symmetry identities satisfied by functions of one variable, including both the real space and momentum space representation. Examples of such functions include the external potential and electron charge density. We also stress that the functions we have in mind for this Section exhibit the full symmetry group of the crystal structure.

Consider a function of one spatial variable that has the symmetry of the Bravais lattice

$$f\left(\mathbf{S}^{-1}\left(\vec{x}-\vec{\tau}\right)\right)=f\left(\vec{x}\right), \tag{86}$$

where $\vec{\tau}$ is the partial lattice translation that corresponds to the rotation $\mathbf{S}$. The Fourier coefficient of f

$$f\left(\vec{G}\right)=\frac{1}{\sqrt{\Omega}}\int_{\Omega}d^3x e^{-i\vec{G}\cdot\vec{x}}f\left(\vec{x}\right), \tag{87}$$

satisfies the following useful identity

$$f\left(\mathbf{S}^{-1}\vec{G}\right)=e^{i\vec{G}\cdot\vec{\tau}}f\left(\vec{G}\right). \tag{88}$$

Thus, if we consider expanding the function f in the momentum basis, we may appeal to the result of Eq. (88) to significantly reduce the number of independent wave vectors, $\vec{G}$, for which we must evaluate the Fourier coefficient of f. Moreover, this is ensured to be particularly useful if one works with "shells" of reciprocal lattice vectors by including all reciprocal lattice vectors up to some reference plane wave cutoff, E_{pw},

$$f(\vec{x}) = \frac{1}{\sqrt{\Omega}} \sum_{\vec{G}}^{E_{pw} \geq \vec{G}^2/2} f(\vec{G}) e^{i\vec{G}\cdot\vec{x}} . \tag{89}$$

The above construction ensures that if the reciprocal lattice vector $\vec{G}$ is included in the representation of $f(\vec{x})$, then $\mathbf{S}\vec{G}$ is included as well; this is crucial, if $f(\vec{x})$ is to satisfy Eq. (86) when represented by a finite number of basis functions.

Symmetries of Functions of Two-Spatial Variables

Consider a function of two spatial variables, which has the full symmetry of the Bravais lattice

$$g\left(\mathbf{S}^{-1}(\vec{x}-\vec{\tau}), \mathbf{S}^{-1}(\vec{x}'-\vec{\tau})\right) = g(\vec{x}, \vec{x}') . \tag{90}$$

Examples of such a function include the KS response and many-body response function, χ, and the exchange-correlation kernel. Consider the double Fourier transform

$$g_{\vec{G},\vec{G}'}(\vec{q}) = \frac{1}{\Omega} \int_{\Omega} d^3x d^3x' e^{-i(\vec{q}+\vec{G})\cdot\vec{x}} g(\vec{x}, \vec{x}') e^{i(\vec{q}+\vec{G}')\cdot\vec{x}} . \tag{91}$$

For the dynamical response function investigated in Chapter One of this Thesis, we evaluate the Fourier coefficients of the dynamical KS response function, typically for finite momentum $\vec{q}$ and zero reciprocal lattice vectors $\vec{G}$ and $\vec{G}'$, i.e. "scalar" calculations. In Chapter Two, we require the zero momentum, but finite reciprocal lattice vector coefficients of the KS response function and its inverse for the exact exchange method. Applying the definition of the coefficient, $g_{\mathbf{S}\vec{G},\mathbf{S}\vec{G}'}(\mathbf{S}\vec{q})$, and making use of the symmetry property as in Eq. (90) obtains

$$g_{\mathbf{S}^{-1}\vec{G},\mathbf{S}^{-1}\vec{G}'}\left(\mathbf{S}^{-1}\vec{q}\right) = e^{i\left(\vec{G}-\vec{G}'\right)\cdot\vec{\tau}} g_{\vec{G},\vec{G}'}\left(\vec{q}\right). \tag{92}$$

As with Eq. (88), this is especially useful for a variety of applications. In evaluating the exchange-only potential in Chapter Two, we only need evaluate the coefficients for a subset of linearly independent reciprocal lattice vectors, which, upon application of all the symmetry operations of the crystal and appealing to the result of Eq. (92), yields the entire Hilbert space used in representing g. With shells of reciprocal lattice vectors for the representation of two point functions the full symmetry properties of $g\left(\vec{x},\vec{x}'\right)$, as in Eq. (90), are fulfilled in the finite basis.

Appendix C: The Kohn-Sham Response Function

The integral equation for the density-density response function is

$$\chi(\vec{x},\vec{x}'\,|\,E)=\chi_S(\vec{x},\vec{x}'\,|\,E) + \int_\Omega d^3y \int_\Omega d^3y' \chi_S(\vec{x},\vec{y}\,|\,E)\{v(\vec{y}-\vec{y}')+f_{xc}(\vec{y},\vec{y}'\,|\,E)\}\chi(\vec{x},\vec{x}'\,|\,E)\,, \tag{93}$$

with dynamical kernels, χ_S, the KS response function introduced in Chapter One and the exchange-correlation kernel, f_{XC}. The KS response function is a correlation function for density fluctuations, $\hat{n}(\vec{x},t)$, about the non-interacting KS ground state density,

$$\chi_S(\vec{x},t\,|\,\vec{x}',t')=-i\theta(t-t')\left\langle\left[\hat{n}(\vec{x},t),\hat{n}(\vec{x}',t')\right]_-\right\rangle_{KS}, \tag{94}$$

The time Fourier transform of the KS response function is

$$\chi_S(\vec{x},\vec{x}'\,|\,E)=2\sum_{\vec{k},j}\sum_{\vec{k}',j'}\frac{\left(f_{\vec{k},j}-f_{\vec{k}',j'}\right)\varphi_{\vec{k},j}(\vec{x})\varphi_{\vec{k}',j'}(\vec{x}')\varphi^*_{\vec{k},j}(\vec{x}')\varphi^*_{\vec{k}',j'}(\vec{x})}{E+i0^+ +E_{\vec{k},j}-E_{\vec{k}',j'}}\,. \tag{95}$$

In Eq. (95) the occupation of KS state $(\vec{k},j)$ is denoted by $f_{\vec{k},j}$ and is unity for states with energy $E_{\vec{k},j}$ less than the Fermi energy E_F and zero otherwise; the factor of 2 in Eq. (95) accounts for spin degeneracy.

In practice we make use of a numerical approximation in which $f_{\vec{k},j}$ is given as a Fermi distribution function for a state with energy $E_{\vec{k},j}-\mu$, broadened by a fictitious "temperature", T,

$$n_F\left(E\right)=\left(1+e^{(E-\mu)/kT}\right)^{-1}. \tag{96}$$

This is also self-consistently carried out in the BZ integrations in the ground state. In Eq. (96), μ is the chemical potential and k is Boltzmann's constant. Although, this introduces slight numerical errors in the KS response function, especially for energies of the order of the numerical broadening, we can safely neglect these numerical errors in the present work as explained below.

In Chapter One, we discuss the KS response function and dynamical density response function for energies typically in the range of 5 *eV* to 40 *eV*. For these energies, the impact of the numerical broadening is negligible. In Chapter Two, we discuss the KS response function for semiconductors. The numerical errors due to "thermal" broadening are negligible, because the numerical broadening is appreciably smaller than the band gap, E_{BG}, which for Si is of the order of 1 *eV*. In the present work, we typically make use of a "temperature" of 116K, corresponding to a numerical broadening of $kT\simeq 10meV$, so that

$$\frac{kT}{E_{BG}} \leq \frac{1}{100}. \tag{97}$$

Rather than solve the integral equation for the density response function, χ, in real space, we choose to work in a basis of complete functions. The two most obvious choices are the KS and momentum basis, both of which are complete

$$\sum_{\vec{q},j} \phi_{\vec{q},j}(\vec{x}) \phi^*_{\vec{q},j}(\vec{x}') = \delta(\vec{x} - \vec{x}'), \tag{98}$$

and

$$\frac{1}{\Omega} \sum_{\vec{q},\vec{G}} e^{i(\vec{q}+\vec{G})\cdot(\vec{x}-\vec{x}')} = \delta(\vec{x} - \vec{x}'). \tag{99}$$

In the present work, we note that, since the mapping of the external potential to the density is only uniquely defined on the range of non-constant potentials, we must exclude constant functions from our basis set representation of χ_S. This is easily accomplished in the restricted momentum space, $\left\{\vec{q}+\vec{G} \mid \vec{q}+\vec{G} \neq 0\right\}$ [28]. The same also holds for the restricted Bloch basis $\left\{\tilde{\phi}_{\vec{q},j}(\vec{x})\right\}$, with the restricted Bloch states, $\tilde{\phi}_{\vec{q},j}(\vec{x})$, defined as

$$\tilde{\phi}_{\vec{q},j}(\vec{x}) \equiv \phi_{\vec{q},j}(\vec{x}) - \frac{\delta_{\vec{q},0}\phi_{\vec{q},j}(\vec{0})}{\sqrt{\Omega}}, \tag{100}$$

with $\phi_{\vec{q},j}(\vec{0})$ the zero reciprocal lattice vector momentum transform of $\phi_{\vec{q},j}(\vec{x})$

If we use the restricted Bloch basis for representing induced charge densities, δn, and potential fluctuations, δv such as in

$$\delta n(\vec{x}) = \sum_{\vec{q},j} \delta n_{\vec{q},j} \tilde{\phi}_{\vec{q},j}(\vec{x}), \tag{101}$$

with the coefficient defined as

$$\delta n_{\vec{q},j} = \int d^3x \delta n(\vec{x}) \tilde{\phi}^*_{\vec{q},j}(\vec{x}), \tag{102}$$

we are then are guaranteed that $\delta n(\vec{x})$ integrates to zero

$$\int d^3x \delta n(\vec{x}) = 0. \tag{103}$$

Furthermore we also ensure that constants are excluded from the space of allowable potential fluctuations. In the Bloch basis the KS response function takes on the form

$$\chi_{S,j,j'}(\vec{q}) = 2 \sum_{\vec{k},n,n} \frac{f_{\vec{k},n} - f_{\vec{k}+\vec{q},n'}}{E_{\vec{k},n} - E_{\vec{k}+\vec{q},n'}} \\ \text{x } A\left(\vec{q}, j \middle| \vec{k}+\vec{q}, n' \middle| \vec{k}, n\right) A^*\left(\vec{q}, j' \middle| \vec{k}+\vec{q}, n' \middle| \vec{k}, n\right), \tag{104}$$

with the matrix elements A as a triple product of Bloch functions

$$A\left(\vec{q}, j \middle| \vec{k}+\vec{q}, n' \middle| \vec{k}, n\right) = \int d^3x \phi^*_{\vec{q},j}(\vec{x}) \phi_{\vec{k}+\vec{q},n'}(\vec{x}) \phi^*_{\vec{k},n}(\vec{x}). \tag{105}$$

Let us consider the $\vec{q}=0$ KS response function, as this is the only term that requires special consideration in the framework of a 1-to-1 correspondence between the external potential and the charge density. Using a Fourier expansion of the zone center KS state, $\phi_{\vec{0},j}(\vec{x})$, the right-hand side of Eq. (105) obtains

$$A\left(\vec{0},j\left|\vec{k},n'\right|\vec{k},n\right)=\frac{\delta_{n,n'}}{\sqrt{\Omega}}\phi^{*}_{\vec{0},j}\left(\vec{0}\right)+\frac{1}{\sqrt{\Omega}}\sum_{\vec{G}\neq\vec{0}}\phi^{*}_{\vec{0},j}\left(\vec{G}\right)\left\langle\vec{k},n\left|e^{-i\vec{G}\cdot\hat{\vec{x}}}\right|\vec{k},n'\right\rangle. \tag{106}$$

In the case of semiconductor, i.e. for a system without a Fermi surface, the first term contributes zero spectral weight to the KS response because there are no interband transitions. In the more general case, replacing the Bloch basis by the restricted Bloch basis in χ_S ensures that the first term in Eq. (106) is excluded. Clearly then, one may use the restricted Bloch basis as a convenient space for the numerical inversion of χ_S. In the present work, we make use of the restricted momentum basis reserving results obtained in the restricted Bloch basis for future research.

The Momentum Representation

In momentum space, and accounting for the discrete translational symmetry of the Bravais lattice, the space-time Fourier coefficients of the KS response function is

$$\begin{aligned}\chi_{S,\vec{G},\vec{G}'}\left(\vec{q},E\right)=&\frac{2}{\Omega}\sum_{\vec{k},j,j'}\frac{f_{\vec{k},j}-f_{\vec{k}+\vec{q},j'}}{E+E_{\vec{k},j}-E_{\vec{k}+\vec{q},j'}+i0^{+}}\\ &\mathrm{x}\left\langle\vec{k},j\left|e^{-i\left(\vec{q}+\vec{G}\right)\cdot\hat{\vec{x}}}\right|\vec{k}+\vec{q},j'\right\rangle\left\langle\vec{k}+\vec{q},j'\left|e^{i\left(\vec{q}+\vec{G}'\right)\cdot\hat{\vec{x}}}\right|\vec{k},j\right\rangle\end{aligned}. \tag{107}$$

Note that in Eq. (107) occurs only one dummy wave vector $\vec{k}$; the second wave vector, originally occurring in Eq. (95), is fixed to be

$$\vec{k}' = \vec{k} + \vec{q} - \vec{H}_{\vec{k},\vec{q}}, \tag{108}$$

where $\vec{H}$ is the *unique* vector of the reciprocal lattice that folds wave vector $\vec{k}+\vec{q}$ into the PZ. In Eq. (107) $\vec{k}+\vec{q}$ is then a shorthand notation for $\vec{k}+\vec{q}-\vec{H}_{\vec{k},\vec{q}}$. We have written down the form of the coefficients $\chi_{S,\vec{G},\vec{G}'}$ for real energy arguments E, but the KS response function is just as easily evaluated on the Matsubara [104] axis, in which case $E+i0^+$ in Eq. (107) is replaced by $iE_n = 2n\pi kT$ with n an integer. The KS response for real energies is then obtained via an analytic continuation to real energies ($iE_n \to E+i0^+$), using, for example, the Pade' approximant technique [105].

The Use of Symmetry

We conclude this Appendix noting some useful symmetry properties of the KS response function which reduce the effort of numerical work. First, note that, the response function has the symmetry of the Bravais lattice

$$\chi\left(\mathbf{S}^{-1}\left(\vec{x}-\vec{\tau}\right),\mathbf{S}^{-1}\left(\vec{x}'-\vec{\tau}\right)\right) = \chi\left(\vec{x},\vec{x}'\right). \tag{109}$$

This applies equally well for the many-body response and KS response function and the exchange-correlation kernel, for finite times or frequencies. As consequence the Fourier coefficients satisfy (see Appendix B)

$$\chi_{\mathbf{S}\vec{G},\mathbf{S}\vec{G}'}(\mathbf{S}\vec{q}) = e^{i(\vec{G}-\vec{G}')\cdot\vec{\tau}}\chi_{\vec{G},\vec{G}'}(\vec{q}). \tag{110}$$

The present work does not explicitly make use of this equation since we generally only need the response functions for select wave vectors (set by experiment).

One can simplify Eq. (107) to cast the response function in a practical form for numerical evaluation. Here we specialize to the case of a semiconducting material for which there is a KS energy band gap and hence well-defined valence and conduction states. With this restriction (which can also be generalized to the case of a metal), one can demonstrate that the KS response can be factored as

$$\chi^{(S)}_{\vec{G},\vec{G}'}(\vec{q},E) = \xi_{\vec{G},\vec{G}'}(q,E) + \xi^{*}_{-\vec{G},-\vec{G}'}(\vec{q},-E), \tag{111}$$

with coefficients

$$\xi_{\vec{G},\vec{G}'}(\vec{q},E) = \frac{2}{\Omega}\sum_{\vec{k},v,c}\frac{f_{\vec{k},v}}{E+E_{\vec{k},v}-E_{\vec{k}+\vec{q},c}+i0^{+}}\left\langle \vec{k},v\left|e^{-i(\vec{q}+\vec{G})\cdot\hat{\vec{x}}}\right|\vec{k}+\vec{q},c\right\rangle \\ \mathrm{x}\left\langle \vec{k}+\vec{q},c\left|e^{i(\vec{q}+\vec{G}')\cdot\hat{\vec{x}}}\right|\vec{k},v\right\rangle . \tag{112}$$

In Eq. (112) the state $\left(\vec{k},v\right)$ is to be understood as a valence state for the KS system, for which $f_{\vec{k},v}$ is unity; correspondingly, the state $\left(\vec{k},c\right)$ is to be understood as a conduction state for the KS system. Note that Eq. (112) is quite useful for we only need to evaluate the matrix elements in Eq. (107) for $\left(\vec{k},j\right)$ an occupied KS level and $\left(\vec{k}+\vec{q},j'\right)$ an unoccupied KS level.

The Kohn-Sham Response in the OPM Method

In the case of the optimized potential method, we only require the zero wave vector response function for finite reciprocal lattice vectors, $\vec{G},\vec{G}'\neq\vec{0}$ (see Chapter Two). In this case, Eq. (112) reduces to

$$\xi_{\vec{G},\vec{G}'}\left(\vec{q}=\vec{0},E\right)=\frac{2}{\Omega}\sum_{\vec{k},v,c}\frac{f_{\vec{k},v}}{E+E_{\vec{k},v}-E_{\vec{k},c}}\left\langle\vec{k},v\left|e^{-i\vec{G}\cdot\hat{\vec{x}}}\right|\vec{k},c\right\rangle \text{x}\left\langle\vec{k},c\left|e^{i\vec{G}'\cdot\hat{\vec{x}}}\right|\vec{k},v\right\rangle, \tag{113}$$

Moreover, using symmetry arguments one can further reduce this to

$$\xi_{\vec{G},\vec{G}'}\left(\vec{q}=\vec{0},E=0\right)=\frac{2}{\Omega}\sum_{\tilde{k}}^{IWBZ}\sum_{\mathbf{S}}^{\{S\}_{\tilde{k}}}\sum_{v,c}\frac{f_{\vec{k},v}}{E_{\vec{k},v}-E_{\vec{k},c}}B_{v,c}\left(\tilde{k}\,|\,\mathbf{S}^{-1}\vec{G}\right) \text{x}\,B_{v,c}^{*}\left(\tilde{k}\,|\,\mathbf{S}^{-1}\vec{G}'\right)e^{i\left(\vec{G}'-\vec{G}\right)\cdot\vec{\tau}}. \tag{114}$$

In this Eq. (114) the matrix elements are defined as

$$B_{v,c}\left(\tilde{q}\,|\,\vec{G}\right)=\left\langle \tilde{q},v\left|e^{-i\vec{G}\cdot\hat{\vec{x}}}\right|\tilde{q},c\right\rangle. \tag{115}$$

The present work on the exchange-only potential discussed in Chapter Two makes explicit use of the representation of the KS response function as in Eq. (114). In these evaluations we expand the KS response function in "shells" of reciprocal lattice vectors (see Appendix B) so that if $\vec{G}$ is included in the basis, $\mathbf{S}\vec{G}$ is included as well and thus we only need evaluate the matrix elements for wave vectors in the IWPZ (see Appendix A) for complete shells of reciprocal lattice vectors. More details of the actual implementation of the exchange-only method are provided in Appendices F and G.

Appendix D: Evaluation of All-Electron Matrix Elements

In this Appendix, we evaluate the matrix elements needed in the all-electron calculations of Chapter One. To this end, we utilize the full potential linearized augmented plane wave (FLAPW) basis [50,52,106-108] for the ground state [51]. While in the plane wave basis, the evaluation of matrix elements can be performed analytically, the all-electron case is formidable, requiring a great deal of mathematical considerations and numerical work. This is easy to visualize; the all-electron states are of a far greater complex character than "pseudized" wave functions, containing not only smooth bonding and anti-bonding regions of charge density in the interstitials but as well as a proliferation of atomic like orbitals near the atomic core. This Appendix also discusses of the use of symmetry in reducing the number of numerical evaluations. The formulas obtained are quite general and apply for all finite wave vectors, $\vec{q}$ and arbitrary $\vec{G}$, or for zero wave vector and finite $\vec{G}$. For the case of zero reciprocal lattice vectors and the limit of vanishing wave vector, which would be necessary in evaluating the optical response, we refer the reader to a separate note [110].

There is a variety of possible means by which to evaluate these matrix elements. One could expand the all-electron wave functions in the momentum basis, introducing the Fourier coefficients of the all-electron states. Clearly, this approach will require a large number of plane waves to represent the oscillatory nature of the all-electron states. We

might also try a numerical approach, with a grid of real space points in the primitive unit cell. Preliminary tests of this method suggest that a large number of such points in the primitive unit cell will be required. We instead adopt a third option, which, although tedious to implement, has reward of general ease of applicability to arbitrary systems and can be optimized quite effectively.

We evaluate the matrix elements semi-analytically, starting with the known real space expansion of KS states in the LAPW basis. We then reduce the evaluation of matrix elements with reciprocal lattice summations and angular integrations. The only remaining integrals are one-dimensional, involving radial basis functions and a spherical Bessel function. This quadrature can be carried out quite accurately and efficiently on a logarithmic mesh, which places more radial points in the region of small r where oscillations in the wave function and electron charge density are the largest.

The LAPW Basis

In the LAPW method the KS states are expanded in a set of basis functions, $\phi_{\vec{k}+\vec{G}}$,

$$\phi_{\vec{k},n}(\vec{x}) = \sum_{\vec{G}} C_n\left(\vec{k}+\vec{G}\right)\phi_{\vec{k}+\vec{G}}(\vec{x}). \tag{116}$$

The summation in Eq. (116) runs over all reciprocal lattice vectors subject to the constraint that $\left|\vec{k}+\vec{G}\right|^2 \le 2E_{cutoff}$. Typically we choose E_{cutoff} in the range of 12-16 Ry,

which results in 100-200 basis functions and proves to be sufficient for the evaluation of the electron charge density, band structure and response functions.

In the LAPW method, the primitive unit cell is partitioned into two regions: (*I*) atomic spheres and the (*II*) interstitial regions. In each of these regions, the basis functions are adapted to describe as accurately as possible the underlying charge densities while minimizing the number of basis functions needed. To this end the basis functions are decomposed as

$$\begin{aligned}\phi_{\vec{k}+\vec{g}}(\vec{x}) &= \theta_{II}(\vec{x})\, e^{i\left(\vec{k}+\vec{g}\right)\cdot\vec{x}} \\ &+ \theta_I(\vec{x})\, 4\pi S^2 \sum_{lm} Y_{lm}^*\left(\vec{k}+\vec{g}\right) Y_{lm}(\hat{x})\left\{a_l\left(\vec{k}+\vec{g}\right)u_l(r) + b_l\left(\vec{k}+\vec{g}\right)\dot{u}_l(r)\right\},\end{aligned} \qquad (117)$$

where Y_{lm} are the spherical harmonics of the angular coordinates of their arguments and the function $\theta_{II}(\vec{x})$ is unity for real space points in region *II* and zero elsewhere; the function $\theta_I(\vec{x})$ is similarly defined to be unity in region *I* (the atomic spheres) and zero elsewhere. In Eq. (117) S is the radius of the atomic sphere and a_l and b_l are coefficients fixed by the boundary conditions imposed on the wave functions at the boundary of the atomic sphere (continuous, with continuous derivatives) . The radial basis functions u_l and $\dot{u}_l$ are the radial solutions of the scalar relativistic approximation to the Dirac equation for the spherical average of the KS potential at fixed linearization energy E_l and its corresponding energy derivative respectively. Being scalar relativistic

solutions of the Dirac equation, these radial functions have a major, u_l^M, and minor component, u_l^m. The reader is also directed to numerous papers on the LAPW method [51,50,52,106,107,108] for further discussion of the method. In practice, we keep up to $l=10$ in the expansion in Eq. (117) for the purpose of diagonalizing the KS Hamiltonian, although only up to $l=6$ is utilized in constructing the charge density or potentials [111]. We should note that in writing Eq. (117) we have assumed (as we will do in all the following) that there is only one atom per primitive unit cell with its corresponding atomic sphere centered at $\vec{x}=0$; furthermore we have written the basis without reference to *local orbitals* [50,52]. All the results presented here are easily generalized to more complicated crystal structures that have multiple atoms per unit cell, for spin-polarized systems, and for systems that require the inclusion of local orbitals. For a more general discussion, the reader is directed to a separate note that discusses these fine points [112,113].

In practice, it is easier to work with states for which the reciprocal lattice summation in Eq. (116) has already been performed for the atomic sphere contribution

$$\varphi_{\vec{k},n}(\vec{x}) = \theta_{II}(\vec{x})\frac{1}{\sqrt{\Omega}}\sum_{\vec{G}} C_j\left(\vec{k}+\vec{G}\right)e^{i\left(\vec{k}+\vec{G}\right)\cdot\vec{x}} + \theta_I(\vec{x})\sum_{lm} Y_{lm}(\hat{x})\left\{A_{lm}^{\vec{k}j}u_l(r)+B_{lm}^{\vec{k}j}\dot{u}_l(r)\right\}. \quad (118)$$

The coefficients $A_{lm}^{\vec{k}j}$ and $B_{lm}^{\vec{k}j}$ of Eq. (118) are easily related to those of Eq. (117). Explicitly for $A_{lm}^{\vec{k}j}$ we have

$$A_{lm}^{\vec{k}j} = \frac{4\pi i^l S^2}{\sqrt{\Omega}} \sum_{\vec{g}} C_j\left(\vec{k}+\vec{g}\right) Y_{lm}^*\left(\vec{k}+\vec{g}\right) a_l\left(\vec{k}+\vec{g}\right). \tag{119}$$

The equation for $B_{l,m}^{\vec{k},j}$ is similar. With Eq. (118) we rewrite the required matrix elements in terms of summations over quantum numbers weighted with appropriate real space integrals. We first separate the contribution from the interstitials and atomic spheres

$$\left\langle \vec{k}, n \left| e^{-i\vec{q}\cdot\hat{\vec{x}}} \right| \vec{k}+\vec{q}, n' \right\rangle = \left\langle \; \right\rangle_I + \left\langle \; \right\rangle_{II}. \tag{120}$$

In Eq. (120) the atomic spheres contribute $\left\langle \; \right\rangle_I$ to the matrix element, whereas $\left\langle \; \right\rangle_{II}$ is solely from the interstitials.

It is necessary to utilize symmetry to relate KS states for wave-vectors in the IWPZ to those in the PZ in order to minimize the memory requirements of the numerical algorithms. By utilizing the fact that the symmetry group of the crystal commutes with the Hamiltonian, one can derive the following symmetry identity for the KS states

$$\varphi_{\mathbf{S}\vec{k},j}\left(\vec{x}\right) = \varphi_{\vec{k}j}\left(\mathbf{S}^{-1}\vec{x}\right),$$

where $\mathbf{S}$ is a matrix representing a rotational symmetry of the Bravais lattice. There is a similar expression for general crystal lattices, for which the full symmetry group includes

partial lattice translations (see Appendix B). Making the following definitions for $\vec{k}$ and $\vec{k}+\vec{q}$ in terms of the symmetries $\mathbf{S}$ and $\mathbf{S}'$ we have

$$\vec{k}=\mathbf{S}\tilde{k} \qquad \vec{k}+\vec{q}-\vec{h}=\vec{k}'=\mathbf{S}'\tilde{k}', \tag{121}$$

where $\tilde{k}$ and $\tilde{k}'$ are wave-vectors in the IWBZ and $\vec{h}$ is the unique reciprocal lattice vector that brings $\vec{k}+\vec{q}$ back into the BZ (see Appendix A), we next demonstrate how to evaluate a general matrix element for arbitrary points in the BZ utilizing the above symmetry identities.

The Interstitials

The integration over the interstitials is most easily performed by integrating over the entire unit cell and then subtracting the integral over the atomic sphere. The result is

$$\langle\ \rangle_{II}=\frac{1}{\Omega}\sum_{\vec{g}\vec{g}'}C_n^*\left(\tilde{k}+\vec{g}\right)C_{n'}\left(\tilde{k}'+\vec{g}'\right)\Gamma\left[\mathbf{S}'\left(\tilde{k}'+\vec{g}'\right)-\left(\vec{q}+\vec{G}\right)-\mathbf{S}\left(\tilde{k}+\vec{g}\right)\right], \tag{122}$$

where $\Gamma\left(\vec{G}\right)$ is

$$\Gamma\left(\vec{G}\right)=\begin{cases}-\dfrac{4\pi}{\left|\vec{G}\right|^3}\left[\sin\left(\left|\vec{G}\right|R\right)-\left|\vec{G}\right|R\cos\left(\left|\vec{G}\right|R\right)\right] & \vec{G}\neq 0\\ \Omega-\dfrac{4\pi}{3}R^3 & \vec{G}=0\end{cases}. \tag{123}$$

For systems with multiple atoms per unit cell, Eq. (123) depends on form factors for the unit cell.

The Atomic Sphere Region

The integration over the atomic sphere requires algebra that is more complex but can be evaluated explicitly in terms of radial integrals. We first define a few convenient notations. The rotational properties of the spherical harmonics are well known [101]. We make use of these properties in defining the rotation tensor, $S^l_{m'm}$, associated with rotation $\mathbf{S}$

$$Y_{lm}\left(\mathbf{S}^{-1}\hat{x}\right)=\sum_{m'} S^l_{m',m} Y_{lm}\left(\hat{x}\right). \tag{124}$$

The rotation matrices $S^l_{m',m}$ are defined with respect to the Euler angles (α,β,γ) (see Fig. 3 of Ref. [101]) as

$$S^l_{m',m}(\alpha,\beta,\gamma)=e^{-im'\alpha} d^l_{m',m}(\beta) e^{-im\gamma}. \tag{125}$$

The coefficients, $d^l_{m',m}$ are given in Rose [101]

$$\begin{aligned} d^l_{m',m}(\beta) &= \sqrt{(l+m)!(l-m)!(l+m')!(l-m')!} \\ &\text{x}\sum_{\kappa}\frac{(-1)^{\kappa}}{\kappa!(l-m'-\kappa)!(l+m-\kappa)!(\kappa+m'-m)!} \\ &\text{x}\left(\cos\frac{\beta}{2}\right)^{2l+m-m'-2\kappa}\left(-\sin\frac{\beta}{2}\right)^{m'-m+2\kappa} \end{aligned}. \tag{126}$$

We also will need the Gaunt coefficients, $K\left(lm\middle|l'm'\middle|l''m''\right)$,

$$K\left(lm\middle|l'm'\middle|l''m''\right)=\oiint d\hat{x}Y_{lm}^{*}\left(\hat{x}\right)Y_{l'm'}\left(\hat{x}\right)Y_{l''m''}\left(\hat{x}\right), \tag{127}$$

which satisfy the following identities that are especially useful for optimizing algorithms

$$K\left(lm\middle|l'm'\middle|l''m''\right)=\begin{cases} 0 & else \\ finite & m=m'+m'',\ l+l'+l''=even,\ \left|l-l''\right|\le l'\le l+l'' \end{cases}. \tag{128}$$

We will also have need to define certain radial integrals, involving the radial basis functions u_l and $\dot{u}_l$, and the spherical Bessel function, j_l

$$\begin{aligned}
\left\langle u_l\middle|j_{l'}\middle|u_{l''}\right\rangle &\equiv \int_{r_o}^{R} r^2 u_l\left(r\right) j_{l'}\left(\left|\vec{q}+\vec{G}\right|r\right)u_{l''}\left(r\right) \\
\left\langle u_l\middle|j_{l'}\middle|\dot{u}_{l''}\right\rangle &\equiv \int_{r_o}^{R} r^2 u_l\left(r\right) j_{l'}\left(\left|\vec{q}+\vec{G}\right|r\right)\dot{u}_{l''}\left(r\right) \\
\left\langle \dot{u}_l\middle|j_{l'}\middle|\dot{u}_{l''}\right\rangle &\equiv \int_{r_o}^{R} r^2 \dot{u}_l\left(r\right) j_{l'}\left(\left|\vec{q}+\vec{G}\right|r\right)\dot{u}_{l''}\left(r\right) \\
\left\langle \dot{u}_l\middle|j_{l'}\middle|u_{l''}\right\rangle &\equiv \int_{r_o}^{R} r^2 \dot{u}_l\left(r\right) j_{l'}\left(\left|\vec{q}+\vec{G}\right|r\right)u_{l''}\left(r\right)
\end{aligned}. \tag{129}$$

In Eqs. (129) r_o is the minimum point kept in the logarithmic mesh on which the radial basis functions are defined. Since the radial functions are derived from the scalar-relativistic approximation to the Dirac equation, they consist of both a major and minor

component, u_l^M and u_l^m respectively. Thus Eqs. (129) are shorthand for a scalar product involving the radial basis functions. For example, we have

$$\left\langle u_l \left| j_{l'} \right| u_{l''} \right\rangle \equiv \int_{r_o}^{R} r^2 \left\{ u_l^M(r) u_{l''}^M(r) + u_l^m(r) u_{l''}^m(r) \right\} j_{l'}\left(\left| \vec{q} + \vec{G} \right| r \right).$$

With this notation, we find the atomic contribution to be

$$\begin{aligned} \left\langle \; \right\rangle_I = 4\pi \sum_{lml'm'l''m''} & (-i)^l Y_{l'm'}^* \left(\mathbf{S}^{-1} \left(\vec{q} + \vec{G} \right) \right) \\ & \text{x} \left\{ A_{lm}^{\tilde{k}j\,*} A_{l''m''}^{\tilde{k}'j\,*} \left\langle u_l \left| j_{l'} \right| u_{l''} \right\rangle + A_{lm}^{\tilde{k}j\,*} B_{l''m''}^{\tilde{k}'j\,*} \left\langle u_l \left| j_{l'} \right| \dot{u}_{l''} \right\rangle \right. \\ & \quad \left. + B_{lm}^{\tilde{k}j\,*} A_{l''m''}^{\tilde{k}'j\,*} \left\langle \dot{u}_l \left| j_{l'} \right| u_{l''} \right\rangle + B_{lm}^{\tilde{k}j\,*} B_{l''m''}^{\tilde{k}'j\,*} \left\langle \dot{u}_l \left| j_{l'} \right| \dot{u}_{l''} \right\rangle \right\} \\ & \text{x} \quad \sum_{m'''=-l''}^{l''} K\left(lm \left| l'm' \right| l''m''' \right) \left(S_{m'''m''}^{l''l''} \right)^* \end{aligned} \quad , \qquad (130)$$

with $\mathbf{S}'' = \mathbf{S}'^{-1}\mathbf{S}$ a symmetry operation of the crystal lattice by group theoretic considerations. Equations (123) and (130) are explicitly utilized in the evaluation of the all-electron response as presented in Chapter One. We conclude this Appendix noting that although the present algorithms have been optimized, they are still quite demanding for dense PZ samplings or for a large number of reciprocal lattice vectors. As such, they have been implemented on the parallel architecture; although this particular aspect is not discussed here, it is very similar to the methodology used in Appendix G.

Appendix E: Linearization of the APW Basis

The Linearization Error

In the linearized augmented-plane-wave (LAPW) method the radial basis functions correspond to solutions of the radial equations for a *given* energy parameter; compared to the APW method, this approximation reduces the numerical work tremendously since the radial basis functions are then independent of the KS eigenvalues. However one should take care to account for the range of energies for which the linearization procedure holds. The theoretical justification of the LAPW method demonstrates that the error in the corresponding KS eigenvalues goes as $\left(E_{\vec{k}j} - E_l\right)^4$ while the error in the KS wave functions goes as $\left(E_{\vec{k}j} - E_l\right)^2$ where E_l is the linearization energy [50,106]. Normally this is of no practical concern since the linearization energy parameter can be chosen to fall in the middle of the valence band of interest. This is especially true for the charge density; however, in dynamical calculations one also has need for unoccupied KS states as well.

There are several methods for improving the linearization procedure, including (i) the APW method, (ii) super-linearized-augmented-plane-wave method (SLAPW) [52] and the (iii) paneling method. Each of these has inherent technical difficulties. The APW method is computationally intensive when required to generate KS states for many

bands and wave vectors and suffers from the so-called asymptote problem [109] that results when the radial basis function vanishes at the atomic sphere boundary.

The SLAPW method is much more demanding than the LAPW technique because three radial functions (radial function and its first two energy derivatives) are needed, and which are then combined to satisfy continuity of value, slope and curvature of the SLAPW basis functions at the atomic sphere boundary. We are not aware of any available ground state codes that use the SLAPW method.

The paneling method suffers in that in each energy window used to span the desired Hilbert space, a new set of basis functions is constructed. As a result, the KS wave functions are not guaranteed to be orthogonal if they correspond to different energy panels. This would be a rather severe problem, having direct ramifications for matrix elements, which occur in the evaluation of quantities such as the KS response function.

The LAPW+LO Method

There is a novel way to avoid all of the above-mentioned problems, using an enhancement of the LAPW method due to Singh. Singh proposed the local orbital scheme (LAPW+LO), originally motivated to treat systems with shallow semi-core levels. With these additional localized basis functions, one can treat semi-core states on the same footing as the more extended valence levels [50,52]. Singh has also shown that with judicious choices for the local orbital linearization energies, $E_{lo} \approx E_l$, the

LAPW+LO scheme becomes a very good approximation to the SLAPW method and one can span a much larger energy window with a greater degree of numerical precision than in the ordinary LAPW method. In this approximate method, the errors in the eigenvalues and wave functions going as $\left(E_{\vec{k}j} - E_l\right)^6$ and $\left(E_{\vec{k}j} - E_l\right)^4$, respectively.

As discussed next, this approach proves to be crucial for ensuring the quality of unoccupied KS levels as in the dynamical response calculations for Ni discussed in Chapter One. For the purposes of the discussion, we refer to this procedure as “sprinkling of local orbitals". We demonstrate the power of the method with a specific example.

Band Structure of Ni

One numerical parameter that has an impact on the completeness of the linearized basis is the radius of the atomic sphere, S (see Appendix D). For a given number of basis functions, a larger atomic sphere will place more demands on the expansion of all quantities into spherical harmonics. One can then perform a cursory check of the quality of the band structure with different choices for the atomic sphere radii.

In Figure 30 we have the LDA electronic structure of Ni for atomic sphere radii of 2.0 and 2.35 with the same number of LAPW basis functions in both calculations. The valence bands and unoccupied bands up to roughly 10 eV above the Fermi level are nearly identical in the two results. Clearly for states above this, there are significant

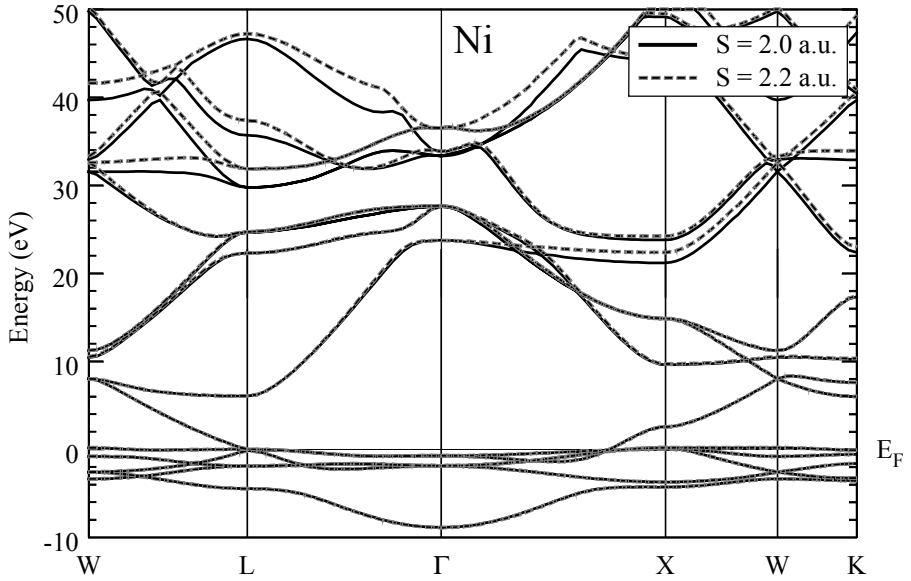

Figure 30 All-electron electronic structure of Ni obtained in the LDA for two choices of the atomic sphere radii. Results for a calculation with an atomic sphere radius of $S = 2.0a_o$ is shown as solid black lines, while the results for $S = 2.35a_o$ are shown as dashed gray lines.

differences. As an example, note that at the W point, at around 40 *eV* above the Fermi level, the latter calculations are nearly 2 *eV* higher than the former. Inclusion of additional LAPW basis functions, i.e. using a larger plane wave cutoff, does not remove these discrepancies, nor does increasing $l_{\max}$ parameter.

In Figure 31 we show the LDA band structure of Ni obtained by performing additional self-consistent ground state calculations with the sprinkling of local orbitals technique. The additional local orbitals included correspond to $l=0$ and $l=2$ [115] with linearization energies chosen as $E_{lo}(l=0)-E_l(l=0)=0.2Ry$ and $E_{lo}(l=2)-E_l(l=2)=0.35Ry$. In practice, we find it almost impossible to choose $E_{lo}\cong E_l$ as this will make the set of basis functions over-complete and the local orbitals will no longer be linearly independent of the standard LAPW basis. It is clear that the two calculations agree over a much larger energy range. While there is essentially no impact of the additional local orbitals for energies up to ~10 *eV* above the Fermi level, the fairly non-dispersive band from Γ to X around 20 *eV* above the Fermi level is shifted down relative to its position in Figure 30. This is consistent with our opening remarks concerning the quality of the basis. It is also instructive to note that this shift results mainly from the inclusion of the $l=2$ local orbital. We are confident that these results constitute the best (numerically) possible LDA band structure one can obtain with

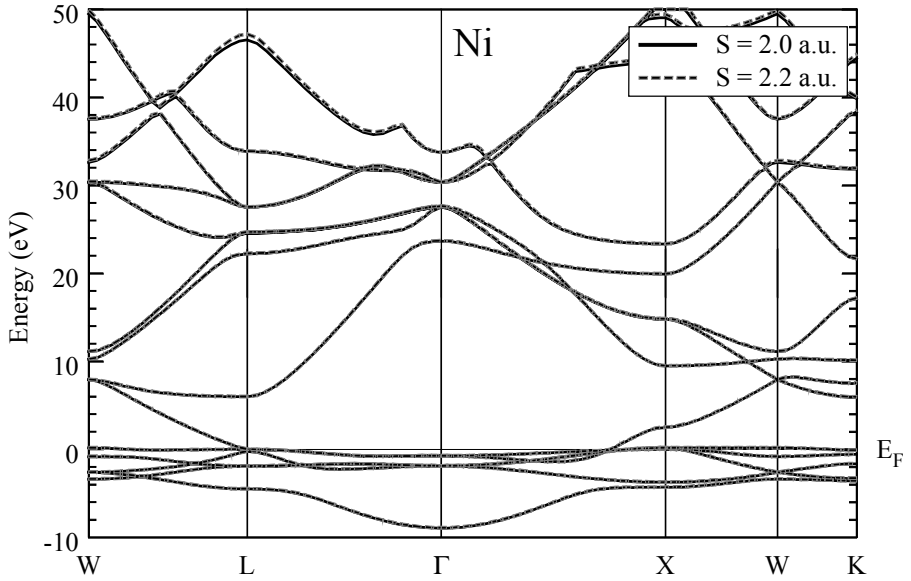

Figure 31 All-electron band structure of Ni obtained in the LDA after inclusion of additional local orbitals chosen to enhance the completeness of the basis. Results for $S = 2.0a_o$ are shown as solid black lines, while the results for $S = 2.35a_o$ are shown as dashed gray lines. The additional local orbitals correspond to $l = 0$ and $l = 2$ with energy parameters $E_{lo}(l = 0) - E_l(l = 0) = 0.2Ry$ and $E_{lo}(l = 2) - E_l(l = 2) = 0.35Ry$ (see text).

the LAPW basis. The calculation of the dynamical density response function of Ni presented in Chapter One is based on this technique.

The trends shown here for the case of Ni are fairly system independent. We have observed the same in systems such as Al (a simple metal) and Si (a semi-conductor). Thus, the quality of the basis is governed mainly by numerical issues, rather than detailed physics of the systems in question. We conclude, by noting that calculations that utilize atomic sphere radii that are 20-25 % smaller than the largest allowed values (set by geometrical arguments) generally yield more accurate unoccupied KS energies. To ensure the numerical artifacts are minimized for general physical quantities, one should examine the impact of using different atomic radii. This may then suggest the inclusion of appropriate local orbitals.

Appendix F: Matrix Elements of the Fock Operator

The Exchange Energy

Matrix elements of the Fock operator (FO) for the N-particle non-interacting KS system are necessary in the evaluation of the exchange-only potential. The FO for the KS system corresponds to the density functional definition of the exchange energy (see Chapter Two and Appendix H) defined as the difference in energy between the expectation value of the Coulomb interaction in the KS ground state and the Hartree energy

$$E_x[n] \equiv \langle \hat{v} \rangle_{KS} - U[n] = \frac{1}{2} \left\langle \hat{v}_F^{KS} \right\rangle_{KS} . \tag{131}$$

In Eq. (131) $U[n]$ is the classical electrostatic (Hartree) energy

$$U[n] = \frac{1}{2} \iint d^3x d^3x' n(\vec{x}) v(\vec{x} - \vec{x}') n(\vec{x}'),$$

$\langle \hat{v} \rangle$ the energy due to pairwise Coulomb interactions

$$\hat{v} = \iint d^3x d^3x' \hat{\psi}^\dagger(\vec{x}) \hat{\psi}^\dagger(\vec{x}') v(\vec{x} - \vec{x}') \hat{\psi}(\vec{x}') \hat{\psi}(\vec{x}), \tag{132}$$

and $\hat{v}_F^{KS}$ the Fock operator for the KS system

$$\hat{v}_F^{KS} = -\iint d^3x d^3x' v(\vec{x} - \vec{x}') \left\langle \hat{\psi}^\dagger(\vec{x}') \hat{\psi}(\vec{x}) \right\rangle_{KS} \hat{\psi}^\dagger(\vec{x}) \hat{\psi}(\vec{x}'), \tag{133}$$

with the expectation value, $\langle\ \rangle_{KS}$, taken in the KS ground state. Given the single-particle nature of the KS system and the known *anti*-commutation rules for the field operators, $\hat{\psi}$ and $\hat{\psi}^{\dagger}$, one can easily show that the definition of E_X in Eq. (131) yields

$$E_x[n] = -\frac{1}{2}\sum_{\vec{q},v}\sum_{\vec{q}',v'} f_{\vec{q},j} f_{\vec{q}',j'} \iint_{\Omega} d^3x d^3x' v(\vec{x}-\vec{x}') \phi_{\vec{q},v}(\vec{x}) \phi^*_{\vec{q},v}(\vec{x}') \\ \text{x}\, \phi_{\vec{q}',v'}(\vec{x}') \phi^*_{\vec{q}',v'}(\vec{x}) \quad , \tag{134}$$

or equivalently

$$E_x[n] = \frac{1}{2}\sum_{\vec{q},v} f_{\vec{q},v} \left\langle \vec{q},v \middle| \hat{v}_F^{KS} \middle| \vec{q},v \right\rangle . \tag{135}$$

In Eqs. (133) and (134) the summation is over wave vectors of the BZ and occupied KS states which contribute to the electron charge density

$$n(\vec{x}) = 2\sum_{\vec{q},v} f_{\vec{q},v} \left| \phi_{\vec{q},v}(\vec{x}) \right|^2 .$$

The real space integration in Eq. (134) runs over the macro crystal, of volume Ω, to which the Born von Karman [99] boundary conditions have been applied. The Fock potential, which is FO in the $\vec{x}$ basis, is

$$\left\langle \vec{x} \middle| \hat{v}_F^{KS} \middle| \vec{x}' \right\rangle = -\sum_{\vec{k},v} f_{\vec{k},v} \phi_{\vec{k},v}(\vec{x}) v(\vec{x}-\vec{x}') \phi^*_{\vec{k},v}(\vec{x}') . \tag{136}$$

The Momentum Basis

The evaluation of matrix elements such as $\left\langle \vec{k}, j \middle| \hat{v}_F^{KS} \middle| \vec{k}, j' \right\rangle$ is greatly simplified making use of an intermediate matrix element evaluation in the momentum basis

$$\left\langle \vec{k}, j \middle| \hat{v}_F^{KS} \middle| \vec{k}, j' \right\rangle = \sum_{\vec{G},\vec{G}'} \phi^*_{\vec{k},j}\left(\vec{G}\right) \left\langle \vec{k}+\vec{G} \middle| \hat{v}_F^{KS} \middle| \vec{k}+\vec{G}' \right\rangle \phi_{\vec{k},j}\left(\vec{G}'\right), \tag{137}$$

with the Fourier coefficients of the KS states

$$\phi_{\vec{k},j}\left(\vec{G}\right) \equiv \frac{1}{\sqrt{\Omega}} \int_{\Omega} d^3x e^{-i\left(\vec{k}+\vec{G}\right)\cdot\vec{x}} \phi_{\vec{k},j}\left(\vec{x}\right).$$

With this approach, the basic computational kernel then, involves the evaluation of matrix elements of the FO between momentum states.

Note that the completeness of the momentum basis

$$\sum_{\vec{q},\vec{G}} \left| \vec{q}+\vec{G} \right\rangle \left\langle \vec{q}+\vec{G} \right| = \hat{1}, \tag{138}$$

guarantees that this procedure is applicable with respect to pseudopotential-based or all-electron wave functions; however, due to the core-orthogonalization effects which arise naturally in the latter, and are eliminated by construction in the former, it is to be expected that many more momentum basis functions will be necessary when carrying out calculations using all-electron wave functions. In pseudopotential-based methods, the Fourier coefficients of the KS states arise naturally in the diagonalization of the

Hamiltonian, and are, therefore, available in any standard ground state program which uses plane wave basis functions.

The Exchange Singularity

For the evaluation of $\left\langle \vec{k}+\vec{G}\left|\hat{v}_F^{KS}\right|\vec{k}+\vec{G}'\right\rangle$ we refer the reader to a similar derivation given by Gygi and Baldereschi, hereafter referred to as GB. GB discussed the evaluation of matrix elements of the FO in their seminal work on the electronic structure of Si [166]. Insertion of FO into the matrix element of Eq. (137) obtains

$$-\frac{1}{\Omega}\sum_{\vec{q},j} f_{\vec{q},j}\iint_{\Omega} d^3x d^3x' e^{-i\left(\vec{k}+\vec{G}\right)\cdot\vec{x}}\phi_{\vec{q},j}\left(\vec{x}\right)v\left(\vec{x}-\vec{x}'\right)\phi^*_{\vec{q},j}\left(\vec{x}'\right)e^{i\left(\vec{k}+\vec{G}'\right)\cdot\vec{x}'}. \tag{139}$$

The two real space integrations in Eq. (139) can be separated by expanding the Coulomb potential in a set of basis functions. The two most natural choices for these basis functions are KS states, $\phi_{\vec{q},j}\left(\vec{x}\right)$, or momentum states $e^{i\left(\vec{k}+\vec{G}\right)\cdot\vec{x}}/\sqrt{\Omega}$. Insertion of the former obtains

$$\begin{aligned}\left\langle \vec{k}+\vec{G}\left|\hat{v}_{HF}^{KS}\right|k+\vec{G}'\right\rangle = -\frac{1}{\Omega}\sum_{\vec{k}',j,n,n'} f_{\vec{q},j}v_{nn'}\left(\vec{k}+\vec{k}'\right)\left\langle \vec{k}+\vec{k}',n\left|e^{i\left(\vec{k}'+\vec{G}\right)}\right|\vec{k},j\right\rangle \\ \text{x}\left\langle \vec{k},j\left|e^{-i\left(\vec{k}'+\vec{G}\right)}\right|\vec{k}+\vec{k}',n'\right\rangle\end{aligned} \tag{140}$$

with $v_{nn'}\left(\vec{q}\right)$ a matrix element of the Coulomb potential

$$v_{n,n}\left(\vec{q}\right)=\iint_{\Omega} d^3x d^3x' \phi^*_{\vec{q},n}\left(\vec{x}\right) v\left(\vec{x}-\vec{x}'\right) \phi_{\vec{q},n}\left(\vec{x}'\right).$$

The latter representation yields

$$\left\langle \vec{k}+\vec{G}\left|\hat{v}_F^{KS}\right|\vec{k}+\vec{G}'\right\rangle = -\frac{1}{\Omega}\sum_{\vec{q},n',\vec{g}} v_{\vec{q}-\vec{k}+\vec{g}} \phi_{\vec{q},n'}\left(\vec{g}+\vec{G}\right)\phi^*_{\vec{q},n'}\left(\vec{g}+\vec{G}'\right) f_{\vec{q},n'} \tag{141}$$

with $v_{\vec{q}+\vec{G}} = 4\pi / \left|\vec{q}+\vec{G}\right|^2$. Due to technical difficulties with the approach embodied in Eq. (140), the present work makes use of the representation given in equation (141); these technical problems are discussed elsewhere [114].

For a fixed wave vector $\vec{k}$, the integration over wave vectors in Eq. (141) contains an integrable singularity at dummy wave vector variables, $\vec{q}_o+\vec{g}_o$, such that $\vec{q}_o-\vec{k}+\vec{g}_o=\vec{0}$. Since both $\vec{k}$ and $\vec{q}$ are in the BZ, this specifies the *unique* point $\left\{\vec{q}_o\left(\vec{k}\right)=\vec{k}, \vec{g}_o=\vec{0}\right\}$, for which the integrand takes the form

$$-\frac{1}{\Omega}\sum_{n'} f_{\vec{k},n'} \phi_{\vec{k},n'}\left(\vec{G}\right)\phi^*_{\vec{k},n'}\left(\vec{G}'\right) v_{\vec{q}_o-\vec{k}}\,. \tag{142}$$

Though the integrand is singular at this point, the integral itself is finite, due to the volume dependence of the BZ summation on the magnitude squared of the dummy wave vector of integration. This can be most easily seen by first changing the dummy variable of integration in Eq. (140) from wave vector $\vec{q}$ to the deviation from $\vec{k}$, $\vec{q}'=\vec{q}-\vec{k}$.

$$\left\langle \vec{k}+\vec{G}\left|\hat{v}_F^{KS}\right|\vec{k}+\vec{G}'\right\rangle = -\frac{1}{\Omega}\sum_{\vec{q}',n',\vec{g}} f_{\vec{q}'+\vec{k},n'} v_{\vec{q}'+\vec{g}}$$

$$\text{x} \quad \phi_{\vec{q}'+\vec{k},n'}\left(\vec{g}+\vec{G}\right)\phi^*_{\vec{q}'+\vec{k},n'}\left(\vec{g}+\vec{G}'\right) \tag{143}$$

The singularity then occurs for $\vec{q}' \to \vec{0}$. In the limit $\vec{q}' \to \vec{0}$ we neglect the $\vec{q}'$-dependence of the Fourier coefficients, $\phi_{\vec{q}'+\vec{k},\nu}\left(\vec{G}\right) \approx \phi_{\vec{k},\nu}\left(\vec{G}\right)$ and occupation function, $f_{\vec{k}+\vec{q}',\nu} \approx f_{\vec{k},\nu}$. Denote by $\Omega_{\vec{k}}$, the region in wave vector space (viewed as the volume parameterized by the independent deviation variable, $\vec{q}' \approx \vec{0}$) for which this approximation is valid; typically we *assume* this volume to be that of the parallelepiped obtained by dividing each basis vector, $\vec{\beta}_i$ of the BZ into N_i equal segments for a total of $N_1 N_2 N_3$ points in the three-dimensional BZ (see Appendix A). The singularity in the evaluation of Eq. (143) is then contained in the following term, written for an occupied state of band index j

$$\frac{1}{\Omega}\sum_{\vec{q}'}^{\Omega_{\vec{k}}} v_{\vec{q}'}\phi_{\vec{q}'+\vec{k},j}\left(\vec{g}+\vec{G}\right)\phi^*_{\vec{q}'+\vec{k},j}\left(\vec{g}+\vec{G}'\right) f_{\vec{q}'+\vec{k},j} \approx$$

$$f_{\vec{k},j}\phi_{\vec{k},j}\left(\vec{g}+\vec{G}\right)\phi^*_{\vec{k},j}\left(\vec{g}+\vec{G}'\right)\left\{\frac{1}{\Omega}\sum_{\vec{q}'}^{\Omega_{\vec{k}}} v_{\vec{q}'}\right\} \quad . \tag{144}$$

Furthermore, only for the purposes of motivating the actual numerical algorithm, we approximate the complex geometrical quadrature implied by the integration over $\Omega_{\vec{k}}$, by that of integration over a sphere of the same volume. In this approximation the integration over $\vec{q}'$ in curly brackets in Eq. (144) is then easily carried out by hand

$$\frac{1}{\Omega_{\vec{k}}}\sum_{\vec{q}'}^{\Omega_{\vec{k}}} v_{\vec{q}'} \approx \frac{1}{2\pi^2} k^* , \tag{145}$$

In Eq. (145) k^* is the radius of the sphere that approximates the volume $\Omega_{\vec{k}}$

$$k^* = \left(\frac{3\Omega_{\vec{k}}}{4\pi} \right)^{\frac{1}{3}} . \tag{146}$$

Clearly the result in Eq. (145) is regular; furthermore, its spectral weight in the numerical evaluation of the integral in Eq. (143) vanishes as $1/\overline{N}$, $\overline{N}$ being a typical number of wave vectors used to sample the BZ in one direction. Thus, in our approximate numerical evaluation described in detail in what follows, we may expect a finite result for the value of the integral in Eq. (143).

Returning to Eq. (142), and motivated by the above arguments, we may integrate over the singular point with a discrete mesh of wave vectors by adding and subtracting a model function that has the same behavior as that of the true integrand for $\vec{q} \to \vec{q}_o\left(\vec{k}\right)$. In terms of the deviation variable, $\vec{q}'$, this model function must go as $4\pi/\left|\vec{q}'\right|^2$ as $\vec{q}' \to \vec{0}$. As noted by GB, the specific form of the model function is not critical; the only conditions are that it satisfy two basic criteria: (i) the model function should be periodic in momentum space, and (ii) sufficiently smooth that it can be accurately integrated via the special points technique. The requirement of periodicity in momentum space is consistent with the periodicity of the function

$$F_{\vec{G}\vec{G}'}(\vec{q}) = \frac{-1}{\Omega}\sum_{n',\vec{g}'} v_{\vec{q}-\vec{k}+\vec{g}'}\phi_{\vec{q},n'}\left(\vec{g}'+\vec{G}\right)\phi^*_{\vec{q},n'}\left(\vec{g}'+\vec{G}'\right) f_{\vec{q},n'}\,, \tag{147}$$

which can be shown to satisfy

$$F_{\vec{G}+\vec{g},\vec{G}'+\vec{g}}(\vec{q}+\vec{g}) = F_{\vec{G}\vec{G}'}(\vec{q})\,. \tag{148}$$

An appropriate model function which satisfies these two properties, combined with the results of Eq. (141) yields

$$\begin{aligned}\left\langle \vec{k}+\vec{G}\left|\hat{v}^{KS}_{HF}\right|k+\vec{G}'\right\rangle = -\frac{1}{\Omega}\sum_{\vec{q},n'} f_{\vec{q},n'}\Big\{ \sum_{\vec{g}} v_{\vec{q}-\vec{k}+\vec{g}}\phi_{\vec{q},n'}\left(\vec{g}+\vec{G}\right)\phi^*_{\vec{q},n'}\left(\vec{g}+\vec{G}'\right) \\ -F\left(\vec{q}-\vec{k}\right)\phi_{\vec{k},n'}\left(\vec{G}\right)\phi^*_{\vec{k},n'}\left(\vec{G}'\right)\Big\} - \frac{1}{\Omega}\sum_{n'}\phi_{\vec{k},n'}\left(\vec{G}\right)\phi^*_{\vec{k},n'}\left(\vec{G}'\right)\sum_{\vec{q}} f_{\vec{q},n}{}'F\left(\vec{q}-\vec{k}\right).\end{aligned} \tag{149}$$

The term in curly brackets is regular provided $F(\vec{q})$ goes like $v_{\vec{q}}$ for $\vec{q}\to\vec{0}$. We note that for a valence band of index n, the corresponding occupation function is independent of wave vector; combining this result with the periodic nature of the model function , the integration over wave vectors in the BZ can be performed independently of the external variable $\vec{k}$ in the last term of Eq. (149). With the specific choice of function that GB propose,

$$\begin{aligned}F(\vec{p}) = 4\pi\left(\frac{a}{2}\right)^2\Big[3-\cos\left(ap_x/2\right)\cos\left(ap_y/2\right) \\ -\cos\left(ap_x/2\right)\cos\left(ap_z/2\right)-\cos\left(ap_y/2\right)\cos\left(ap_z/2\right)\Big]^{-1}\end{aligned} \tag{150}$$

which is consistent with both (i) and (ii) above, we have the following result for the value of the integral of $F(\vec{q})$ over the BZ of the fcc lattice

$$\frac{1}{\Omega}\sum_{\vec{q}} F(\vec{q}) = \frac{1}{(2\pi)^3}\int_{BZ} d^3qF(\vec{q}) = \frac{4\text{x}4.423758}{a\pi} \equiv \frac{2\pi}{a} N_{GB}. \tag{151}$$

In Eq. (151) a is the lattice constant of the crystal and the last equality serves as a convenient algorithmic definition of N_{GB}. For a semiconductor, the occupation function, $f_{\vec{q},n}$, is independent of wave vector for all the bands, so that we may use the result of Eq. (151) for all the valence states in evaluating the last term of Eq. (149). In the case of a metal, we may use the result of Eq. (151) for all the valence bands; for conduction states, we must then evaluate a complicated geometrical integral implied by the last term of Eq. (149). For the present work, we focus strictly on semiconducting materials, leaving a more general evaluation of last term of Eq. (149) for a future publication [103]. This completes the evaluation of the matrix elements in Eq. (141). In practice, we use symmetry arguments to further simplify the BZ integration of Eq. (149). (see Appendices A and B for general BZ and symmetry considerations).

The Use of Symmetry

Recall the symmetry properties of the KS wave functions (see Appendix B)

$$\phi_{\mathbf{S}\vec{k},j}(\vec{x}) = e^{i\mathbf{S}\vec{k}\cdot\vec{\tau}}\phi_{\vec{k},j}\left(\mathbf{S}^{-1}(\vec{x}-\vec{\tau})\right).$$

In this equation, $\mathbf{S}$ is an operation of the point group of the crystal and $\vec{\tau}$ is the corresponding partial lattice translation, which, when combined with $\mathbf{S}$ to form the pair, $\{\mathbf{S},\vec{\tau}\}$, is an element of the space group of the Bravais lattice. Having this result in mind, we partition the summation over wave vectors, $\vec{q}$, in the BZ of Eq. (149) into a summation over the IWBZ and the "stars of $\vec{q}$", $\{\mathbf{S}\}_{\tilde{q}}$ (see Appendices A and B). We also adopt the following notation for the rest of this Appendix; the "external" wave vector of the Fock matrix element, $\vec{k}$, is restricted to the IWBZ and we will denote this explicitly as $\tilde{k}$. The reason for adopting this convention becomes clear when one considers the symmetry properties of the Fock matrix elements

$$\left\langle \mathbf{S}\tilde{k}, j \left| \hat{v}_F^{KS} \right| \mathbf{S}\tilde{k}, j' \right\rangle = \left\langle \tilde{k}, j \left| \hat{v}_F^{KS} \right| \tilde{k}, j' \right\rangle . \tag{152}$$

Thus, we only need to evaluate the above matrix elements for wave vectors in the IWBZ. Dropping the wave vector dependence of the occupation function, $f_n \equiv f_{\tilde{q},n}$, as is appropriate for semiconductors, and using the symmetry properties of the KS states we have

$$\begin{aligned}\left\langle \tilde{k}+\vec{G} \left| v_{HF}^{KS} \right| \tilde{k}+\vec{G}' \right\rangle = -\frac{1}{\Omega}\sum_{\tilde{q},j}\sum_{\mathbf{S}}^{\{\mathbf{S}\}_{\tilde{q}}} f_j \int_{\Omega}\int_{\Omega} d^3x d^3x' e^{-i\left(\tilde{k}+\vec{G}\right)\cdot\vec{x}} e^{i\left(\tilde{k}+\vec{G}'\right)\cdot\vec{x}'} \\ \text{x}\ \ \phi_{\tilde{q},j}\left(\mathbf{S}^{-1}\left(\vec{x}-\vec{\tau}\right)\right) v\left(\vec{x}-\vec{x}'\right) \phi^*_{\tilde{q},j}\left(\mathbf{S}^{-1}\left(\vec{x}'-\vec{\tau}\right)\right) \quad .\end{aligned} \tag{153}$$

The spatial integrations can now be carried out analytically making explicit use of the plane wave representation of the Bloch states

$$\phi_{\tilde{q},j}\left(\vec{x}\right)=\frac{1}{\sqrt{\Omega}}\sum_{\vec{G}}\phi_{\tilde{q},j}\left(\vec{G}\right)e^{i\left(\tilde{q}+\vec{G}\right)\cdot\vec{x}}\ .$$

Inserting this form into Eq. (153) and making use of the fact that the Coulomb potential is diagonal in momentum space, obtains

$$\begin{aligned}\left\langle\tilde{k}+\vec{G}\left|\hat{v}_{HF}^{KS}\right|\tilde{k}+\vec{G}'\right\rangle=&-\frac{2\pi}{a}\gamma_{\vec{G}\vec{G}'}\left(\tilde{k}\right)N_{GB}-\frac{1}{\Omega}\beta_{\vec{G}\vec{G}'}\left(\tilde{k}\right)\\&+\frac{1}{\Omega}\sum_{\substack{\tilde{q},\mathbf{S}\\ \mathbf{S}\tilde{q}\neq\tilde{k}}}\Big[\gamma_{\vec{G}\vec{G}'}\left(\tilde{k}\right)F\left(\mathbf{S}\tilde{q}-\tilde{k}\right)\\&-\sum_{n,\vec{g}}f_n v_{\mathbf{S}\tilde{q}-\tilde{k}+\vec{g}}\phi_{\tilde{q},n}\left(\mathbf{S}^{-1}\left(\vec{G}+\vec{g}\right)\right)\phi_{\tilde{q},n}^{*}\left(\mathbf{S}^{-1}\left(\vec{G}'+\vec{g}\right)\right)e^{-i\left(\vec{G}-\vec{G}'\right)\cdot\vec{\tau}}\Big],\end{aligned}\tag{154}$$

with γ and β being convenient definitions for numerical work

$$\beta_{\vec{G}\vec{G}'}\left(\tilde{k}\right)\equiv\sum_{\vec{g}\neq\vec{0}}v_{\vec{g}}\sum_{n}f_n\phi_{\tilde{k},n}\left(\vec{G}+\vec{g}\right)\phi_{\tilde{k},n}^{*}\left(\vec{G}'+\vec{g}\right),\tag{155}$$

and

$$\gamma_{\vec{G}\vec{G}'}\left(\tilde{k}\right)=\sum_{n}f_n\phi_{\tilde{k},n}\left(\vec{G}\right)\phi_{\tilde{k},n}^{*}\left(\vec{G}'\right).\tag{156}$$

Note that the summation over wave vectors in the BZ in Eq. (154) excludes the point $\mathbf{S}\tilde{q}=\tilde{k}$.

Before concluding this Appendix, we note one further feature of the matrix elements of the FO. Appealing the Hermitian nature of the FO, one can demonstrate the momentum matrix elements of Eq. (153) satisfy

$$\left\langle \vec{k}+\vec{G}\left|\hat{v}_F^{KS}\right|\vec{k}+\vec{G}'\right\rangle = \left\langle \vec{k}+\vec{G}'\left|\hat{v}_F^{KS}\right|\vec{k}+\vec{G}\right\rangle^* . \tag{157}$$

A similar expression may also be obtained for the KS matrix elements

$$\left\langle \vec{k},j\left|\hat{v}_F^{KS}\right|\vec{k},j'\right\rangle = \left\langle \vec{k},j'\left|\hat{v}_F^{KS}\right|\vec{k},j\right\rangle^* . \tag{158}$$

Equations (157) and (158) are especially useful for reducing the number of floating point operations needed in the evaluation of the exchange-only potential. For explicit details, the reader is directed to Appendix G.

We conclude this Appendix noting that the algorithms used in the present work of Chapter Two are based on the results displayed in Eqs. (154), (155), (156). Evaluation of all the necessary matrix elements needed for Eq. (137) becomes prohibitive on a serial computer. Hence, these algorithms have been constructed to make use of the massively parallel architectures, distributing the computational workload equally among all the processors. Details of this parallelization and the other programmatic aspects of this calculation can be found in Appendix G.

Appendix G: Computational Approach to the Exchange-Only Method

In this Appendix, we review some computational details of the present numerical work on the EXCHANGE-ONLY method. This will include a discussion of the algorithms used to implement the calculations on the massively parallel architecture, with reference to point-to-point and collective communication calls from the Message Passing Interface (MPI) standard [115]. We also describe an efficient method by which single source code distributions can be ported to a variety of operating systems. This Appendix is concluded with a discussion of the integration of the EXCHANGE-ONLY algorithm with the Fritz-Haber ground state program [76].

Exchange Matrix Elements

In the present work on the exact exchange method, the most demanding computational kernels are matrix elements of the Fock operator in the momentum basis (see Appendix F)

$$\left\langle \vec{k}+\vec{G}\left|\hat{v}_F^{KS}\right|\vec{k}+\vec{G}'\right\rangle = -\frac{1}{\Omega}\sum_{\vec{q},n',\vec{g}} v_{\vec{q}-\vec{k}+\vec{g}}\phi_{\vec{q},n'}\left(\vec{g}+\vec{G}\right)\phi^*_{\vec{q},n'}\left(\vec{g}+\vec{G}'\right) f_{\vec{q},n'} . \qquad (159)$$

Clearly, the evaluation of the matrix element of Eq. (159) scales as $N_v N_{\vec{g}} N_{\vec{q}}$ with N_v the number of valence states, $N_{\vec{q}}$ the number of wave vectors in the BZ, and $N_{\vec{g}}$ the number

of reciprocal lattice vectors kept in the summation over $\vec{g}$ on the left-hand side of Eq. (159). The other most demanding kernels are matrix elements of density fluctuation operator $e^{-i\vec{q}\cdot\hat{\vec{x}}}$ taken between KS states $\left|\vec{k}+\vec{q}, j'\right\rangle$ and $\left\langle\vec{k}, j\right|$. These matrix elements scale only as $N_{\vec{g}}$. Moreover, we need a reasonably large number (~100-200) of momentum matrix elements $\left\langle\vec{k}+\vec{G}\left|\hat{v}_{HF}^{KS}\right|\vec{k}+\vec{G}'\right\rangle$ to well represent the desired matrix element

$$\left\langle\vec{k}, j\left|\hat{v}_{HF}^{KS}\right|\vec{k}, j'\right\rangle=\sum_{\vec{G},\vec{G}'}\phi_{\vec{k},j}^{*}\left(\vec{G}\right)\left\langle\vec{k}+\vec{G}\left|\hat{v}_{HF}^{KS}\right|\vec{k}+\vec{G}'\right\rangle\phi_{\vec{k},j}\left(\vec{G}'\right). \tag{160}$$

Having in mind this large number of terms to evaluate, each of which is computationally intensive, we construct an algorithm to parallelize the evaluation of exchange-only potential of Chapter Two.

Denote by $N_{\vec{G}}^{F}$ the number of terms needed in each of the reciprocal lattice summations on the right-hand side of Eq. (160) to accurately represent the left-hand side. This obtains only $N_{\vec{G}}^{F}\left(N_{\vec{G}}^{F}+1\right)/2$ independent number of elements on the right-hand side; the remaining elements can be obtained from considering the Hermitian nature of the FO (see Appendix F). Let us consider performing the evaluation of the right-hand side of Eq. (160) on a collection of N_{PE} processing elements (PE) [117] operating in parallel and numbered from 0 to $N_{PE}-1$. Use ξ to denote a super index, which runs from 1 to $N_{Total}^{F}\equiv N_{\vec{G}}^{F}\left(N_{\vec{G}}^{F}+1\right)/2$ serving as the index of the independent matrix

elements on the right-hand side of Eq. (160). As a final bit of notational convenience for the rest of this Appendix, we simplify the notation of the HF matrix element to be

$$v_{F,\xi} \equiv \begin{cases} \left\langle \vec{k}+\vec{G}(\xi) \middle| \hat{v}_F^{KS} \middle| \vec{k}+\vec{G}'(\xi) \right\rangle & \vec{G} \neq \vec{G}' \\ \dfrac{\left\langle \vec{k}+\vec{G}(\xi) \middle| \hat{v}_F^{KS} \middle| \vec{k}+\vec{G}(\xi) \right\rangle}{2} & \vec{G} = \vec{G} \end{cases}. \tag{161}$$

With this notation, the right-hand side of Eq. (160) can be transformed into

$$\sum_{\xi} \phi^*_{\vec{k},j}\left(\vec{G}(\xi)\right)\phi_{\vec{k},j}\left(\vec{G}'(\xi)\right)v_{F,\xi} + \phi^*_{\vec{k},j}\left(\vec{G}'(\xi)\right)\phi_{\vec{k},j}\left(\vec{G}(\xi)\right)v^*_{F,\xi}\,. \tag{162}$$

Note that the factor of $1/2$ in Eq. (161) ensures that the diagonal elements of the FO are not double counted when represented as in Eq. (162).

Hermiticity and Parallelization

To parallelize the structure of this equation, we divide the total number of terms on the right-hand side of Eq. (162) equally between all the PE's. In the case that N^F_{Total} is not exactly divisible by, N_{PE} we distribute the terms in a "round-robin" fashion, assigning the remainder left upon modular division one at a time starting with PE number 0. As a specific example, suppose $N^F_{\vec{G}} = 6$ which yields $N^F_{Total} = 21$ independent terms. We choose $N_{PE} = 4$, and, upon dividing the data among these 4 PE's, we assign 6 matrix elements to PE 0 and 5 matrix elements to the remaining PE's; this is depicted

schematically in Figure 32. Furthermore, denote by ξ_i a super index referring to the terms the i^{th} PE is assigned to evaluate. For the specific example quoted above, we have

$$1 \le \xi_0 \le 6, \quad 7 \le \xi_1 \le 11, \quad 12 \le \xi_2 \le 16, \quad 17 \le \xi_3 \le 21 .$$

With this parallel division, the right-hand side of Eq. (162) then reads

$$\sum_{i=0}^{N_{PE}-1} \sum_{\xi_i} \Big[\phi^*_{\vec{k},j}\left(\vec{G}(\xi_i)\right) \phi_{\vec{k},j}\left(\vec{G}'(\xi_i)\right) v_{F,\xi_i} + \phi^*_{\vec{k},j}\left(\vec{G}'(\xi_i)\right) \phi_{\vec{k},j}\left(\vec{G}(\xi_i)\right) v^*_{F,\xi_i} \Big] \quad , \tag{163}$$

where the sum over ξ_i is over the terms the i^{th} PE is to evaluate. If we use $v^i_{F,j,j'}$ to denote the matrix element which the i^{th} PE evaluates

$$v^i_{F,j,j'} = \sum_{\xi_i} [\phi^*_{\vec{k},j}\left(\vec{G}(\xi_i)\right) \phi_{\vec{k},j}\left(\vec{G}'(\xi_i)\right) v_{F,\xi_i} + \phi^*_{\vec{k},j}\left(\vec{G}'(\xi_i)\right) \phi_{\vec{k},j}\left(\vec{G}(\xi_i)\right) v^*_{F,\xi_i}] \quad , \tag{164}$$

then the matrix element of the right-hand side of Eq. (163) consists of independent contributions from all the PE's

$$\left\langle \vec{k}, j \left| \hat{v}^{KS}_F \right| \vec{k}, j' \right\rangle = \sum_{i=0}^{N_{PE}-1} v^i_{F,j,j'} . \tag{165}$$

In terms of the actual algorithm, the summation on the right-hand side of Eq. (165) is evaluated via a call to MPI_ALLREDUCE(), with the global operation MPI_SUM. This

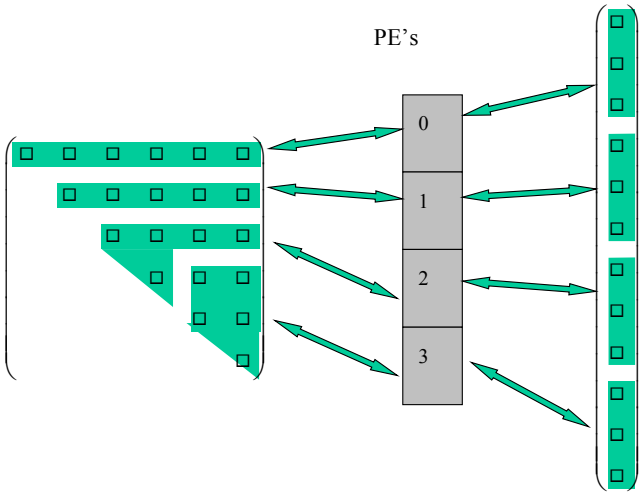

Figure 32 Parallelization of matrix elements of the FO motivated by its Hermitian nature. The PE's are numbered 0-3 and the elements they are responsible for evaluating are denoted with arrows. Also shown is a schematic representation of the parallelization of vector quantities in the OPM algorithm.

routine will perform the summation over the PE's, with the result passed to all the PE's [116].

A similar procedure is applied to vector quantities. As a specific example, we have the Fourier coefficients of the exchange-correlation potential

$$v_{xc}\left(\vec{G}\right) \equiv \frac{1}{\sqrt{\Omega}} \int_{\Omega} d^3x e^{-i\vec{G}\cdot\vec{x}} v_{xc}\left(\vec{x}\right). \tag{166}$$

Denote by $N_{\vec{G}}^{xc}$ the number of Fourier coefficients kept in representing the real space form of the exchange-correlation potential; we may divide the evaluation of these coefficients among the various PE's in a fashion similar to that applied to matrix element of the FO. Each PE is then responsible for computing only a subset of the desired coefficients, which will then be collected in the memory of every PE via MPI communication calls (see Figure 32). Before discussing the integration of the EXCHANGE-ONLY algorithm with the ground state program, we first briefly review a few general procedures by which source trees can be developed to be as portable as possible.

Source Code Preprocessing

We note that in porting codes among various machines one always faces the problem of dealing with interface calls to external libraries and the precision appropriate for the calculation and the architecture. As an example of the former problem, note that

single and double precision NAG routines are named differently, ending in 'E' for single precision routines and 'F' for double precision. This technical problem occurs in porting code between RISC and Cray machines, which by default have a different representation for single and double precision. The latter problem can normally be solved by forcing the compiler to default all floating and integer types to a specific precision. On the Cray T3E for example, this accomplished with the '-dp' switch supplied to the FORTRAN90 compiler. The compiler then converts all double precision objects to single precision; note that single precision on the T3E is equivalent to what is normally referred to as double precision on RISC machines. The later problem can be more troublesome, especially if one uses different numerical libraries on different machines. An efficient method to overcome this technical difficulty makes use of the concept of source-code *preprocessing* [118].

With a few additional lines of code, one can construct source trees that compile transparently on nearly any machine with the correct external library calls and/or precision. Only a very small subset of the all the available preprocessor directives are actually used in the present work, the two essential being **#ifdef** and **#define** [118,119]. The form of the #ifdef construct is

```
#ifdef MACRO1
.
.
#endif
```

’

where MACRO1 is a preprocessor variable referred to as a *macro* that can either be defined or undefined (analogous to the logical true and false statements) or defined with a specific value, such as "10" or "F04ADF". When used in the true/false context, the #ifdef construct is useful for compiling objects with different data types according to user needs or machine precision. For example, suppose we need code to support both the IBM SP3 and Cray T3E architectures, i.e. it must be available in both double and single precision form. Furthermore, suppose that on the IBM SP we also require support for complex arithmetic. In this case, a sample code snippet may read as follows.

```
#ifdef IBMSP
c Compile with double precision data
#ifdef COMPLEX
c Double precision complex data
      complex*16 sampledata2(10)
#else
c Double precision real data
      real*8 sampledata(10)
#endif
#elifdef CRAYT3E
c Single precision real data
      real*4 sampledata(10)
#else
#endif
```

In the above, the lines beginning with 'c' are FORTRAN comments and have no bearing on the data types or precision. It is a simple matter to define the macros IBMSP, COMPLEX and/or CRAYT3E on the command line, or in a Makefile [120].

As an example of when it is convenient to define a macro with a specific value, consider the following code snippet.

```
#ifdef IBMSP
#define DETER F04AAF
#elifdef CRAYT3E
#define DETER F04AAE
#else
#define DETER MYOWNDETER
#endif
```

With the above construct, the macro DETER will be defined to 'F04ADF' on the IBM SP and 'F04ADE' on the Cray T3E and to 'MYOWNDETER' on some other class of machines. Note that the names 'F04AAF' and 'F04AAE' are the names of NAG routines for computing the determinant of a complex matrix of double and single precision respectively. Then upon preprocessing the code snippet

```
c Compute the determinant of a matrix
      call DETER(A,N,M,determinant, wkspce,ifail),
```

the preprocessor will substitute the value [121] of the macro DETER according to its definition above. Thus, the code is nearly transparent to the user and will compile as

expected on a variety of machines. We move next to discuss the integration of the EXCHANGE-ONLY algorithm, with the Fritz-Haber ground state program [76].

Integration of the EXCHANGE-ONLY and Ground State Programs

In principle, one must solve the KS equations self-consistently with the corresponding exchange-correlation potential (see Chapter Two and Appendix H). The self-consistency loop has the structure of that in Figure 33. The electron charge density is obtained from the occupied KS states and determines the new KS effective potential. This is the structure in traditional approaches with approximate functionals that only depend on the charge density, as in the LDA or GGA's. However, the exchange functional depends only implicitly on the charge density, being instead, an explicit functional of the density matrix. Therefore, one needs the KS wave functions in constructing the corresponding exchange potential. This is the only major conceptual difference between the structure of density-dependent potentials and the exchange-only approach adopted here.

Integration of the algorithm for computing the exchange-only potential with the ground state program is crucial, if the technique is to be easily applicable to a general system. In the present numerical work, we utilize the ground state information provided by the Fritz-Haber code [76]. Our discussion is thus specific for this particular program although the procedure should be similar for other plane wave based codes. In order to

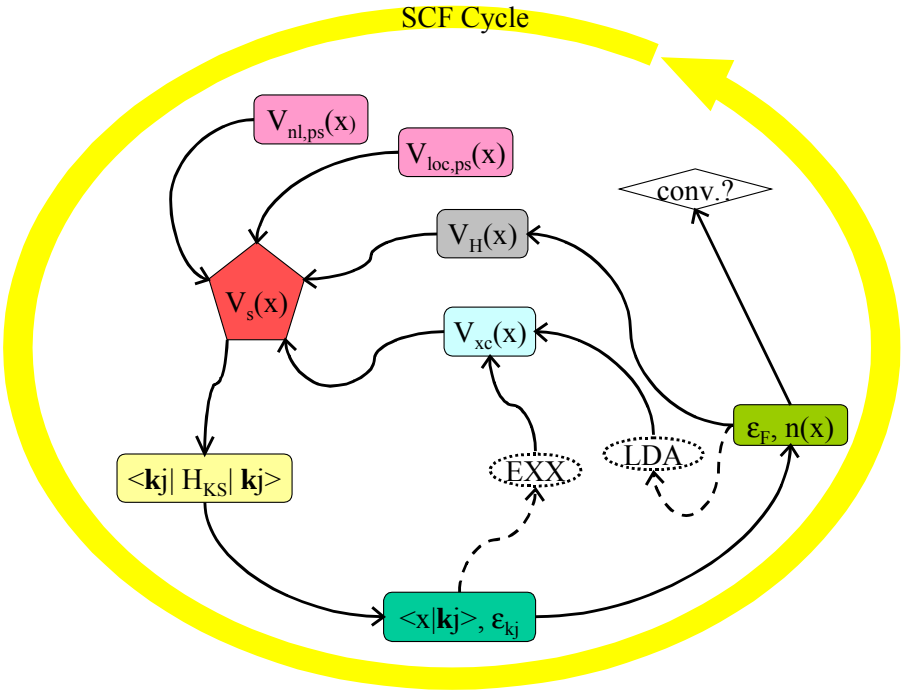

Figure 33 Self-consistency loop for solving the KS equations with the exchange-correlation potential and the charge density. Explicitly this is shown for pseudopotential-based calculations, although the structure is very similar for all-electron calculations.

minimize the number of source code changes to the ground state program, only three subroutines of the *fhi96md* program are modified: (i) we generate a driver program for setting up the process groups and which synchronizes the master and worker PE's, (ii) we modify the main program of the fhi96md source tree to be a subroutine, adding a dynamic switch which turns on the exchange-only potential after a specified number of iterations of the KS equations with the LDA functional, and (iii) we create a buffer program that transforms the ground state information into a useful form for carrying out the evaluation of the exchange-only potential. The structure of such an algorithm is depicted schematically in Figure 34, where the original source for the Fritz-Haber program is that region in the upper right, bounded by the bordered box. To this end, we only add a few basic signal-handling procedures to the original source code and two additional pieces of I/O to/from disk. The I/O to and from disk provides for interface with the algorithm for the exchange-only potential.

The exchange-only algorithm developed for the present work is independent of the ground state program, being flexible enough to execute in stand-alone fashion with a given set of ground state data, or as an additional library of exchange-correlation functionals in lieu of those provided by the Fritz-Haber code. In the next few paragraphs we discuss specific details of modifications the source code of the ground state program.

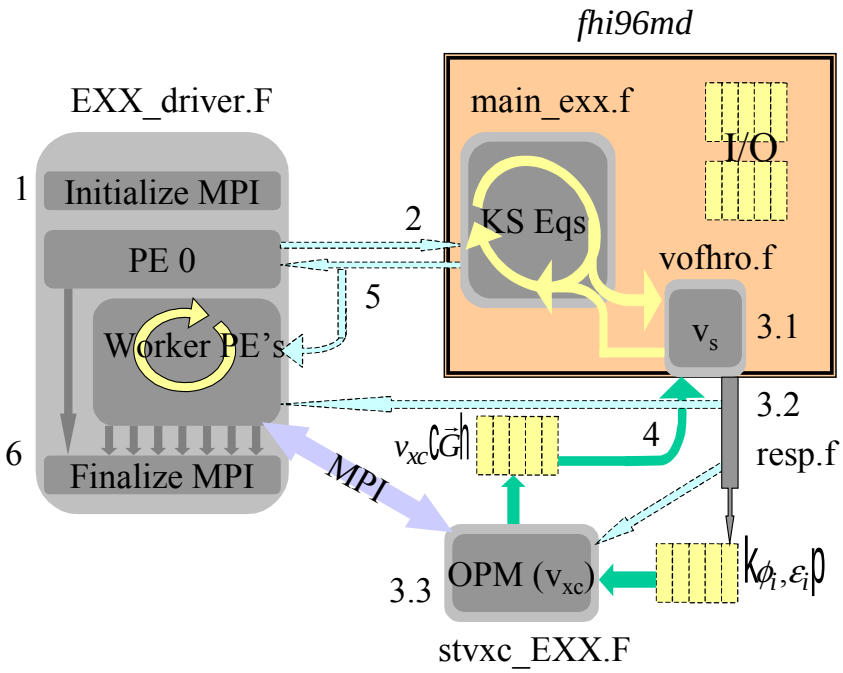

Figure 34 Integration of the algorithm for computing the exchange-only potential with the Fritz-Haber ground state program. Schematically, the ground state program is confined to the bordered box at the upper right, while all objects outside this box are additions developed in the current work. File I/O is handled in the dashed blocked areas whereas signal handling is denoted by the dashed arrows.

In principle, one could simply parallelize the entire ground state calculation, whereby every PE self-consistently solves the KS equations, only making real use of the parallel architecture when constructing the exchange potential. However, this leads to difficulties, for each PE will perform I/O, thereby corrupting the data on disk. An alternative approach, being nearly as easy to implement and requiring fewer modifications to the ground state code, requires only the master PE (typically PE number 0) to solve the KS equations with the exchange-only potential, which, itself, is computed making full use of the parallel architecture. The only subtle point in constructing such an algorithm is the synchronization of the master and worker nodes for evaluating the exchange potential. This particular task is taken care of in the driver program *EXCHANGE-ONLY_driver.F* (see Figure 34). In this driver program, the master PE makes a call to the fhi96md ground state program, which then proceeds to self-consistently solve the KS equations in the normal fashion. For the worker nodes, they sit in a ready state waiting for a signal from the master PE to begin evaluating their contributions to the exchange potential, returning to this ready state after this evaluation is completed. After a number of iterations with the LDA functional are completed, the algorithm then switches on the exchange-only potential. The master node signals the worker nodes (labeled step 3.2 in Figure 34) to begin accepting ground state data. Simultaneous with this, the routine *resp.f* generates a file on disk containing all the necessary KS wave functions and energies need to evaluate the exchange-only potential. By keeping the transfer of information from the ground state

program to the exchange-only algorithm entirely through disk space, we avoid corrupting any of the ground state data and, moreover, we maintain the independence of the algorithm from the specific details of the ground state program. The exchange-only algorithm then proceeds, utilizing MPI for communication calls and parallelizing the data according to the procedure outlined at the beginning of this Appendix. The Fourier coefficients of the exchange potential are written to file, to be read in by the master node in the Fritz-Haber program. The worker nodes return to a state of readiness, awaiting the next start signal from the mater PE. Upon reaching self-consistency the mater node signals the worker nodes (step 5 in Figure 34); the calculation ends with a call to MPI_FINALIZE() [116]. A typical evaluation of the exchange potential requires 50-60 PE's and 4 hours wall clock time.

Appendix H: Density Functional Theory

In this Appendix we review some of the most salient features of density functional theory. This will include a discussion of the basic underlying theorems put forth in the classic papers of Hohenberg and Kohn [29] and Kohn and Sham [19]. We conclude this Appendix with a discussion of static linear response and its relevance for the exchange-only calculations in Chapter Two.

Density Functional Theory

We consider a perfectly spin-compensated system of N electrons interacting via the bare Coulomb interaction, $v(\vec{x}-\vec{x}') = 1/|\vec{x}-\vec{x}'|$, and with a *local* external potential, v_{ext}. The appropriate Hamiltonian for this system, written in second quantized notation in terms of the field operators $\hat{\psi}(\vec{x})$ and $\hat{\psi}^{\dagger}(\vec{x})$ is

$$\hat{H} = -\frac{1}{2}\int d^3x\,\hat{\psi}^{\dagger}(\vec{x})\vec{\nabla}^2\hat{\psi}(\vec{x}) + \int d^3x\,\hat{\psi}^{\dagger}(\vec{x})\hat{\psi}(\vec{x})\,\mathrm{v}_{ext}(\vec{x}) + \frac{1}{2}\int d^3x d^3x'\,\hat{\psi}^{\dagger}(\vec{x})\hat{\psi}^{\dagger}(\vec{x}')v(\vec{x}-\vec{x}')\hat{\psi}(\vec{x}')\hat{\psi}(\vec{x}) \quad . \tag{167}$$

The field operators $\hat{\psi}$ and $\hat{\psi}^{\dagger}$ annihilate and create electrons, respectively, satisfy the canonical anti-commutation rules

$$\begin{aligned} \left[\hat{\psi}^{\dagger}(\vec{x}),\hat{\psi}^{\dagger}(\vec{x}')\right]_+ &= \left[\hat{\psi}(\vec{x}),\hat{\psi}(\vec{x}')\right]_+ = 0 \\ \left[\hat{\psi}^{\dagger}(\vec{x}),\hat{\psi}(\vec{x}')\right]_+ &= \delta(\vec{x}-\vec{x}') \end{aligned} \quad , \tag{168}$$

and serve as the generalized conjugate variables in the Hamilton approach to the quantum-mechanical many-body problem. The total energy of the N particle system consists of the kinetic energy, T, potential energy due to the pair-wise Coulomb interaction, V, and potential energy due to the external field, V_{ext},

$$E = \left\langle H \right\rangle_{GS} = T + V + V_{ext}. \tag{169}$$

In Eq. (169), the expectation values are taken in the ground state of the many-body system, $\left|\Psi_{GS}\right\rangle$. In their seminal work on the "Inhomogeneous Electron Gas", Hohenberg and Kohn [29], hereafter referred to as HK, argue that, for a given external potential, the energy is a unique functional of the charge density

$$E = E\left[n\right]. \tag{170}$$

Equation (170), though it appears rather innocent, has wide sweeping ramifications for the rest of the theoretical analysis that follows. HK established this powerful result by demonstrating the external potential and electron charge density are in one-to-one correspondence.

Denote the mapping from the external potential to the charge density by A. This map, $A: \mathrm{v}_{ext} \to n$, is constructed from the charge density,

$$n\left(\vec{x}\right) = \left\langle \hat{\psi}^{\dagger}\left(\vec{x}\right)\hat{\psi}\left(\vec{x}\right)\right\rangle_{GS}, \tag{171}$$

corresponding to the ground state solution of the Schrödinger equation (see Figure 35),

$$\hat{H}\left|\Psi_{GS}\right\rangle = E\left|\Psi_{GS}\right\rangle. \tag{172}$$

HK argue for the uniqueness of (and hence, the invertibility of) A by appealing to the Rayleigh-Ritz variational principle.

We remind the reader here of a subtle point that has received renewed attention as of late, for practical *ab initio* approaches such as those undertaken in Chapter Two. The mapping, and hence the inverse mapping, of the potential to the density is only unique (invertible) on the domain of non-constant functions; the corresponding range of this map only includes the space of non-constant functions also. This construction excludes the possibility of constant changes in either the external potential or the charge density. The former restriction is quite clear, since a constant change in the external potential will not change the ground state wave function (other than an arbitrarily chosen phase, which has no physical consequences for most observables) or charge density. The latter restriction retains charge neutrality since we demand that the external potential not create or annihilate real electrons.

HK separated the total energy into a universal functional, F, which depends only implicitly on the external potential and a term, V_{ext}, that depends explicitly on the external potential

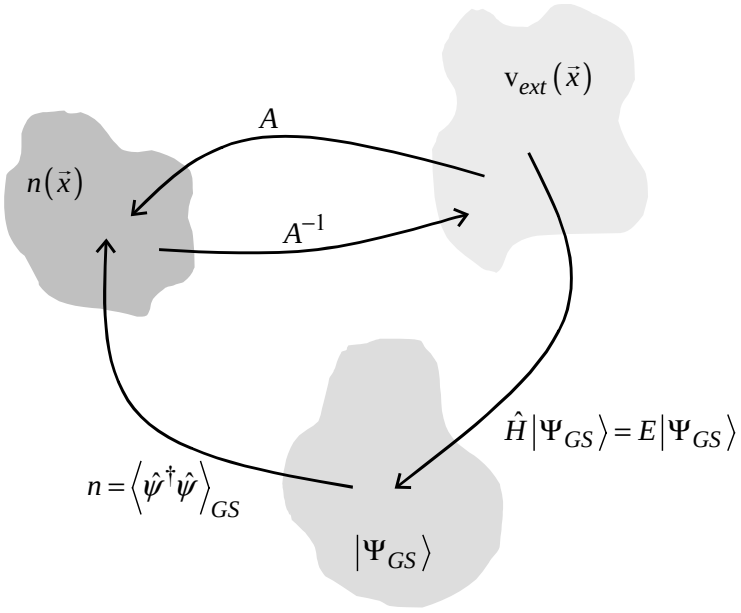

Figure 35 Mapping and inverse mapping of the external potential to the charge density.

$$E_{\mathrm{v}}[n_{\mathrm{v}}] = F[n_{\mathrm{v}}] + \mathrm{V}_{ext}[n_{\mathrm{v}}], \tag{173}$$

with

$$V_{ext} = \int d^3x\, n(\vec{x})\, \mathrm{v}_{ext}(\vec{x}). \tag{174}$$

In Eqs. (173) and (174) we have adopted the shorthand notation, n_{v}, to stand for the charge density in correspondence with the external potential, v_{ext}. The implicit dependence is controlled through mean values with reference to the ground state wave function, as, for example, in the charge density

$$n_{\mathrm{v}}(\vec{x}) = \left\langle \Psi^{\mathrm{v}}_{GS} \left| \hat{\psi}^{\dagger}(\vec{x}) \hat{\psi}(\vec{x}) \right| \Psi^{\mathrm{v}}_{GS} \right\rangle.$$

The universal functional of Eq. (173) is the internal energy of the isolated electronic system

$$F[n_{\mathrm{v}}] = E_0[n_{\mathrm{v}}] = \left\langle \Psi^{\mathrm{v}}_{GS} \left| \hat{H} \right| \Psi^{\mathrm{v}}_{GS} \right\rangle = T[n_{\mathrm{v}}] + V[n_{\mathrm{v}}], \tag{175}$$

evaluated at the electron charge density corresponding to v_{ext}.

HK established the variational nature of the total energy functional of Eq. (170)

$$\delta\left(E_{\mathrm{v}}[n_{\mathrm{v}}] - \mu N[n_{\mathrm{v}}]\right) = 0. \tag{176}$$

In this equation μ is a Langrage multiplier, identified as the chemical potential, necessary to maintain a fixed number of particles

$$N[n_{\mathrm{v}}] = \int d^3x n_{\mathrm{v}}(\vec{x}) = N\,. \tag{177}$$

The variation in Eq. (176) is to be affected about the ground state density for the N particle system with fixed external potential. For notational convenience for the remainder of this Appendix, unless otherwise specifically noted, we adopt the shorthand notation in which n stands for n_{v}. We will also make use of the shorthand notation, $E[n]$, to stand for the internal energy of the electronic system evaluated at the density n_{v}., explicitly using $E[n] + \int d^3x \mathrm{v}_{ext}(\vec{x}) n(\vec{x})$ to mean the total energy of the system. With the separation of the total energy as in Eq. (173) we have

$$\frac{\delta F[n]}{\delta \mathrm{n}(\vec{x})} = \mu - \mathrm{v}_{ext}(\vec{x})\,. \tag{178}$$

Following the approach of HK, we separate from the functional F a mean-field (electrostatic) contribution

$$F[n] = \frac{1}{2}\iint d^3x d^3x' n(\vec{x}) v(\vec{x} - \vec{x}') n(\vec{x}') + G[n]\,. \tag{179}$$

The functional G is the remainder of the internal energy of the electron system, consisting of the kinetic energy of the many-body system and the difference between the expectation value of the Coulomb potential, $\hat{v}$,

$$\hat{v} = \frac{1}{2}\iint d^3x d^3x' \hat{\psi}^\dagger(\vec{x})\hat{\psi}^\dagger(\vec{x}')v(\vec{x}-\vec{x}')\hat{\psi}(\vec{x}')\hat{\psi}(\vec{x}), \tag{180}$$

and the Hartree energy

$$U[n] = \frac{1}{2}\iint d^3x d^3x' n(\vec{x})v(\vec{x}-\vec{x}')n(\vec{x}'),$$

yielding

$$G[n] = T[n] + \left\langle \hat{V} \right\rangle_{GS} - U[n]. \tag{181}$$

HK then go on to discuss further properties of the functional G including its relation to the electronic polarizability and providing an approximate expression for the total energy of an electron gas of slowly varying density. We instead proceed to the classic paper of Kohn and Sham [19] who developed a practical formalism based on the groundwork laid by HK.

Following KS, we further separate the functional G with reference to a non-interacting system,

$$G[n] = T_S[n] + \left\langle \hat{V} \right\rangle_S - U[n] + \left\langle \hat{T} + \hat{V} \right\rangle_{GS} - \left\langle \hat{T} + \hat{V} \right\rangle_S . \tag{182}$$

In Eq. (182) the expectation value $\langle \, \rangle_S$ is take in the ground state, $|\Psi_{GS}\rangle_S$, of the reference non-interacting system.

The non-interacting reference system in question has totally anti-symmetric wave function formed as a Slater determinant of the N lowest single particle states obtained as solutions of a Schrödinger equation with a local effective potential, v_{eff}

$$\left\{ -\frac{1}{2}\vec{\nabla}^2 + v_S(\vec{x}) \right\} \phi_i(\vec{x}) = E_i \phi_i(\vec{x}) . \tag{183}$$

It is a rather nontrivial matter to suppose the existence of some single-particle-like system with local effective potential, which yields the same density as the exact ground state density of the many-body system. This is the so-called non-interacting v-representability problem, has been a point of some controversy among theorists in the field [122], and having only been truly resolved for the time dependent density functional theory due to van Leeuwen [26]. For the time independent case, there is no known proof for the existence of an effective potential that yields the correct electron charge density. In all of this work we assume this to be a non-issue, i.e. that the electron charge density is non-interacting v-representable.

Motivated by one of the central results of HK, that the so-called exchange correlation energy,

$$E_{XC}[n] \equiv E[n] - T_s[n] - U[n], \tag{184}$$

can be written as

$$E_{XC}[n] \simeq \int d^3x n(\vec{x}) \varepsilon_{XC}(n(\vec{x})) \tag{185}$$

for the electron gas of slowly varying density, KS determined uniquely the local effective potential of Eq. (183). In Eq. (185) $\varepsilon_{xc}(n)$ is the exchange-correlation energy per particle of a homogeneous electron gas of density n. Then by HK, one has the following restriction on variations away from the exact ground state density

$$\int d^3x \left\{ \frac{\delta T_S[n]}{\delta n(\vec{x})} + \mathrm{v}_{ext}(\vec{x}) + v_H[n](\vec{x}) + \frac{\delta E_{XC}[n]}{\delta n(\vec{x})} - \mu \right\} \delta n(\vec{x}) = 0, \tag{186}$$

where the variations are affected about the ground state density. KS noted that Eq. (186) is the same as one obtains for a system of non-interacting particles moving in an effective field

$$v_S[n](\vec{x}) = v_{XC}[n](\vec{x}) + v_H[n](\vec{x}) + \mathrm{v}_{ext}(\vec{x}), \tag{187}$$

corresponding to a Hamiltonian given by

$$\hat{H}_{eff} = -\frac{1}{2}\int d^3x \hat{\psi}^\dagger(\vec{x})\vec{\nabla}^2\hat{\psi}(\vec{x}) + \int d^3x \hat{\psi}^\dagger(\vec{x})\hat{\psi}(\vec{x})v_S(\vec{x}). \tag{188}$$

In Eq. (187) $v_{XC}[n](\vec{x})$ is the so-called exchange-correlation potential

$$v_{XC}[n](\vec{x}) = \frac{\delta E_{XC}[n]}{\delta n(\vec{x})}, \tag{189}$$

whose physical content is such as to yield the same charge density as the correlated many-body ground state. It consists of an exchange contribution, $v_x = \delta E_x / \delta n$ and a correlation contribution $v_c = \delta E_c / \delta n$. In Chapter Two, we provide an exact evaluation of v_x.

The total energy of such a system is

$$E_S[n] = T_S[n] + U_S[n], \tag{190}$$

with the effective potential energy

$$U_S[n] = \int d^3x\, n(\vec{x})v_S(\vec{x}), \tag{191}$$

and charge density

$$n(\vec{x}) = \sum_{i=1}^{N} \left|\phi_i(\vec{x})\right|^2. \tag{192}$$

In this equation, the KS orbitals are to satisfy Eq. (183) with the KS effective potential. With Eq. (184) we may obtain the total energy of the system as

$$E[n]+\int d^3x n(\vec{x})\,\mathrm{v}_{eff}(\vec{x})=\sum_{i=1}^{N}\varepsilon_i-U[n]-U_{XC}[n]+E_{XC}[n]. \tag{193}$$

The exchange-correlation potential energy, $U_{xc}[n]$, is defined by

$$U_{xc}[n]=\int d^3x n(\vec{x})v_{xc}[n](\vec{x}). \tag{194}$$

Equations (187),0, and (193) constitute the Kohn-Sham method and must be solved self-consistently to yield the correct charge density and corresponding effective potential.

Though the KS equations constitute an exact solution to the many-body problem, in the sense that they generate the correct charge density, we have no explicit expressions for general physical quantities of interest. More importantly, there is no known way to evaluate even the exchange-correlation potential, and hence the charge density, in an exact fashion except for few-electron systems, where the exact electron charge density is already known from configuration interaction calculations. In Chapter Two we present a general procedure for the evaluation of an approximate DFT scheme in which exchange is treated exactly.

Static Linear Response

Let us next note that the form of the total energy functional of Eq. (193) lends itself naturally to an introduction of the integral equation for the density response function for the many-body system. We also discuss the integral equation for the finite frequency (time dependent) case in Chapter One. Recall that the total energy of the system, $E[n]+\int d^3x \mathrm{v}_{ext}(\vec{x})n(\vec{x})$, has associated second variational coefficient of the electronic energy

$$\chi^{-1}(\vec{x},\vec{x}') = -\frac{\delta^2 E}{\delta n(\vec{x})\delta n(\vec{x}')} = \frac{\delta \mathrm{v}_{ext}(\vec{x})}{\delta n(\vec{x}')}. \tag{195}$$

The dynamical density response function, is a two-particle correlation, measuring density fluctuations about the ground state charge distribution

$$\chi(\vec{x},\vec{x}'\,|\,t-t') = -i\Theta(t-t')\left\langle\left[\hat{n}(\vec{x},t),\hat{n}(\vec{x}',t')\right]_-\right\rangle_{GS}, \tag{196}$$

for which $\chi(\vec{x},\vec{x}')$ is the static limit and $\chi_S^{-1}(\vec{x},\vec{x}')$ is its associated inverse. Considering the energy as in Eq. (193) one can establish the following integral equation

$$\chi(\vec{x},\vec{x}') = \chi_S(\vec{x},\vec{x}') + \iint d^3y d^3y' \chi(\vec{x},\vec{y})\left[v(\vec{y}-\vec{y}') + f_{XC}(\vec{y},\vec{y}')\right]\chi(\vec{y}',\vec{x}'). \tag{197}$$

In Eq. (197), the response function for the KS system is given by the canonical form

$$\chi_S(\vec{x},\vec{x}') = 2\sum_{i,j}\frac{f_i - f_j}{E_i - E_j}\phi_i(\vec{x})\phi_j(\vec{x}')\phi_i^*(\vec{x}')\phi_j^*(\vec{x}), \tag{198}$$

whereas its inverse is the negative of the second variational coefficient of the electronic energy of the KS system

$$\chi_S^{-1}(\vec{x},\vec{x}') = -\frac{\delta^2 E_S[n]}{\delta n(\vec{x})\delta n(\vec{x}')} = -\frac{\delta^2 T_S[n]}{\delta n(\vec{x})\delta n(\vec{x}')} = \frac{\delta v_S(\vec{x})}{\delta n(\vec{x}')}. \tag{199}$$

In Eq. (197), the exchange-correlation kernel f_{XC} is the second variational coefficient of the exchange-correlation energy

$$f_{xc}(\vec{x},\vec{x}') = \frac{\delta^2 E_{xc}[n]}{\delta n(\vec{x})\delta n(\vec{x}')}. \tag{200}$$

Being density response functions for the many-body and KS systems, χ and χ_S satisfy Kubo identities relating changes in the external and effective potentials, $\delta \mathrm{v}_{ext}$ and δv_S, to changes in the charge density, δn,

$$\delta n(\vec{x}) = \int d^3x' \chi(\vec{x},\vec{x}')\delta \mathrm{v}_{ext}(\vec{x}') \tag{201}$$

and

$$\delta n(\vec{x}) = \int d^3x' \chi_S(\vec{x},\vec{x}')\delta n(\vec{x}'). \tag{202}$$

Of course, by definition of the uniqueness of the mapping of the external potential to the density, demands that the formulas are only applicable for variations $\delta \mathrm{v}_{ext}$ and δv_S in their respective domains, and for variations in the charge density that are v-representable. Furthermore, it is interesting to note that the *exact* exchange-correlation potential can be obtained from an equation such as Eq. (202) for a specific charge density variation, δn_{xc},

$$v_{xc}(\vec{x}) = \int d^3x' \chi_S^{-1}(\vec{x}, \vec{x}') \delta n_{xc}(\vec{x}'). \tag{203}$$

In Eq. (203) $\delta n_{XC}(\vec{x})$ is obtained as a specific choice of density fluctuation about the ground state density. This is discussed in more detail in Chapter Two.

Appendix I: A Digression on the Exchange-Correlation Kernel

In this Appendix, we briefly review a recently noted [30] problem with the definition of the exchange-correlation potential as defined in a manner analogous to the time-independent case.

The Quantum Mechanical Action

Let us consider separating the quantum mechanical action of Eq. (5), as in the time-independent case (see Appendix H), into a universal functional, $B[n]$, and the potential energy due to the external potential

$$A[n] = B[n] + \int dt \int d^3x \, \mathrm{v}_{ext}(\vec{x},t)\, n(\vec{x},t). \tag{204}$$

The functional $B[n]$ is just the quantum mechanical action for the isolated electronic system

$$B[n] = \int dt \left\langle \Psi(t) \left| i\frac{\partial}{\partial t} - \hat{H}_o \right| \Psi(t) \right\rangle, \tag{205}$$

evaluated for the time dependent charge density in one-to-one correspondence (via RG) with $\mathrm{v}_{ext}(\vec{x},t)$ and $\hat{H}_o$ is the intrinsic electron Hamiltonian

$$\hat{H}_o = -\frac{1}{2}\int d^3x\,\hat{\psi}^\dagger(\vec{x})\vec{\nabla}^2\hat{\psi}(\vec{x}) + \frac{1}{2}\int d^3x\,d^3x'\,\hat{\psi}^\dagger(\vec{x})\hat{\psi}^\dagger(\vec{x}')v(\vec{x}-\vec{x}')\hat{\psi}(\vec{x}')\hat{\psi}(\vec{x}). \tag{206}$$

Furthermore, we may consider separating from $B[n]$ an exchange-correlation contribution defined in analogy to the time-independent case (see Appendix H)

$$A_{xc}[n] = \int dt\left\langle \Psi(t)\left| i\frac{\partial}{\partial t} - \hat{T} - \hat{V}\right|\Psi(t)\right\rangle - \int dt\left\langle \Psi_S(t)\left| i\frac{\partial}{\partial t} - \hat{T} - \hat{V}\right|\Psi_S(t)\right\rangle, \tag{207}$$

where $\left|\Psi_S(t)\right\rangle$ is the time dependent non-interacting state for the KS system.

The Exchange-Correlation Kernel

With the definition of $A_{xc}[n]$ as in Eq. (207) and in analogy with the time independent case, one might consider defining the exchange-correlation potential as the first variational coefficient of the exchange-correlation action,

$$\frac{\delta A_{xc}}{\delta n(\vec{x},t)}.$$

However, this is improper, for it leads to a time-dependent exchange-correlation kernel, f_{xc},

$$f_{xc}\left(\vec{x},t\,|\,\vec{x}',t'\right)=\frac{\delta v_{xc}\left(\vec{x},t\right)}{\delta n\left(\vec{x}',t'\right)}, \tag{208}$$

which is symmetric in the time-domain, rather than of the proper causal behavior. Two approaches to avoid this and other problems with the quantum mechanical action formulation of TDDFT have been discussed recently in the literature. Görling [28] has put forth a time-dependent version of DFT that does not appeal to the action formulation at all. Using perturbative methods, he derived a method for generating the exact exchange-correlation potential. van Leeuwen has also commented recently on TDDFT in a series of three important papers. This author first obtained a time-dependent version of the Sham-Shluter equation [33], thereby providing a means by which to evaluate the exact time-dependent exchange-correlation potential [27] from the exact many-body Green's function [34], although still lacking is the explicit functional dependence $v_{XC}\left[n\right]\left(\vec{x},t\right)$. In the second of these papers [30], he noted that the major problem with the quantum mechanical action formulation of TDDFT, namely the non-casual response of the exchange-correlation kernel, can be avoided by working with Keldysh [35] techniques. In this formalism, all quantities are symmetric functions of a pseudotime variable and have the proper causal behavior when carried over to real times. In the last of these [26], he established the validity of v-representability for arbitrary time-dependent densities. For our purposes it suffices that the exchange-correlation kernel defined in Eq. (208) is the

first functional derivative of the exchange-correlation potential, which itself is defined operationally to yield the correct time-dependent density.

Vita

James Moye Sullivan was born in Washington, North Carolina on July 1, 1972. He graduated from Washington High School in May of 1990. After a year of study at the University of North Carolina at Charlotte, he transferred to North Carolina State University where he received he received a B.S. in Physics and a B.S. in Mathematics in May of 1995.

In 1995 he began graduate studies in the Department of Physics at the University of Tennessee at Knoxville. Before joining the research group of Adolfo G. Eguiluz, Professor of Physics, in January of 1997, he concentrated entirely on class work. From January 1997 to December 2000 his research efforts focused attention on theoretical condensed matter physics, establishing collaborations with members of Oak Ridge National Laboratory, and serving as a Graduate Student Liason in the Department of Physics. Mr. Sullivan received the degree of Doctor of Philosophy with a major in Physics in May of 2001. After graduation, he will join the staff of Naval Research Laboratory in Washington, D.C. as a postdoctoral fellow in the Research Associateship Program of the National Research Council.